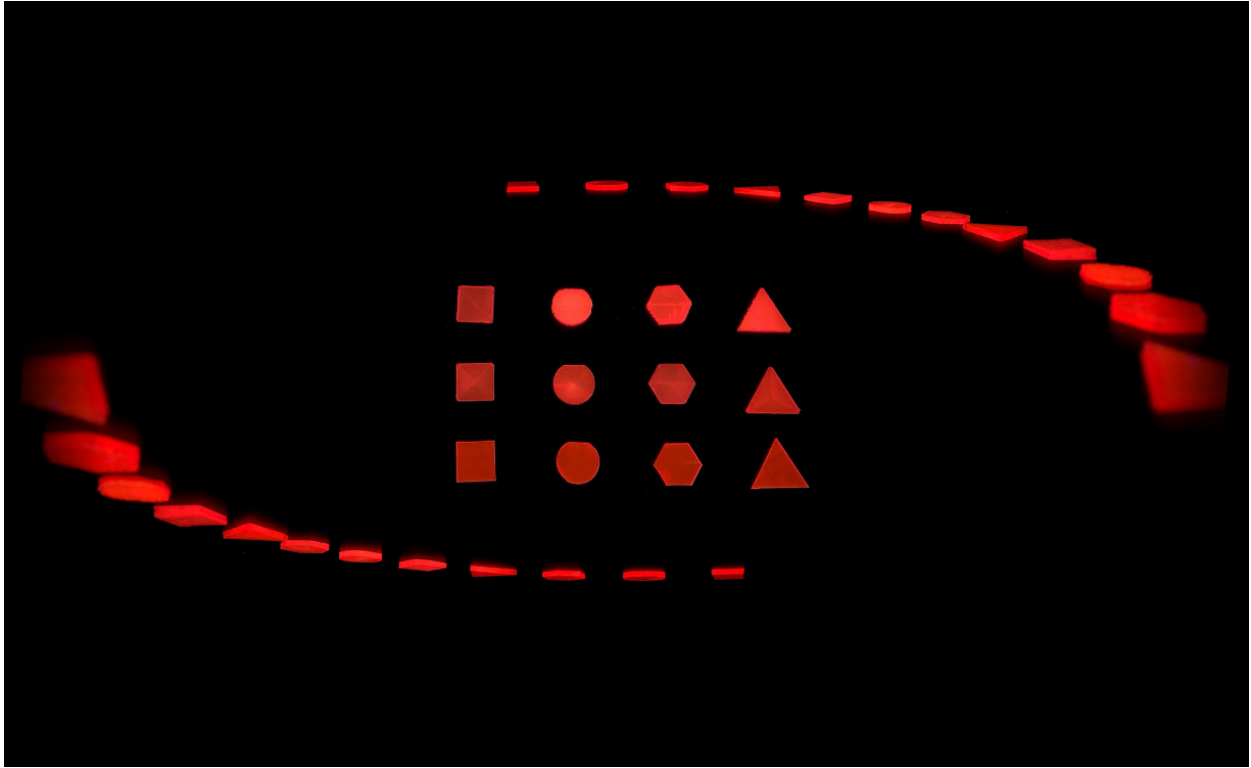


End-to-end performance analysis of 3D printed luminescent solar concentrators



Shomik Verma
St. John's College

Supervisor: Dr. Rachel Evans
Photoactive Materials Group
Department of Materials Science and Metallurgy
University of Cambridge

This thesis is submitted for the degree of Master of Philosophy.

Originally Submitted: September 2020
Corrections Submitted: November 2020

I. Declaration

This thesis is the result of my own work and includes nothing which is the outcome of work done in collaboration except where explicitly stated in the text. It is not substantially the same as any work that has already been submitted before for any degree or other qualification. It does not exceed the word limit prescribed by the Degree Committee for the Faculty of Physics and Chemistry (15,000 words excluding tables, footnotes, bibliography, and appendices).

II. Acknowledgements

The work reported in this thesis was conducted in the Functional Photoactive Materials Group in the Department of Materials Science and Metallurgy at the University of Cambridge with funding from the European Research Council (ERC) and the Marshall Scholarship. I would like to thank Dr. Rachel Evans for her vision, insights, and invaluable guidance throughout this project. I am also grateful for the rest of my lab group who helped me quickly get up to speed and provided a wonderful community.

III. Abstract

In recent years, there has been increasing urgency to develop cheap, efficient solar devices. However, most solar modules are large, bulky, and rectangular, making integration into the built environment non-trivial. A promising technological solution that may help solve this problem is the luminescent solar concentrator (LSC). A typical LSC is a plastic slab that absorbs sunlight and re-emits light of a tailored wavelength towards its edges, where solar cells can be installed. Because LSCs are colorful, semi-transparent, and modular, they hold great potential in reducing the cost and barrier to entry of solar technologies. However, they suffer from significant optical losses limiting their efficiency. Many novel device shapes have been proposed to improve light transport pathways in LSCs, but these often rely on expensive or wasteful fabrication techniques.

A potential solution to this is 3D printing, which has gained immense traction as an alternative manufacturing technology. 3D printing has many benefits including accessibility, rapid prototyping, and fabrication of completely new designs. This study presents an end-to-end performance analysis methodology to evaluate new LSC designs that can take advantage of this novel manufacturing technology. This methodology is applied to preliminary 3D printed parts as a proof of concept that can be applied to a wider variety of designs.

This study consists of 3 distinct steps: simulating the optical efficiency of the printed part, 3D printing the part with luminescent filament, and characterizing its optical efficiency experimentally.

Simulation of LSCs using ray tracing has been extensively investigated in the past; however, this has been limited to conventional, rectangular LSCs. Analyzing the performance of alternative LSC geometries requires developing a novel methodology for

evaluating device efficiency, as well as implementing parallelization techniques to reduce computation time for complex geometries.

Among the 3D printing technologies, fused deposition modeling (FDM) is the most accessible and widely used, but it is not known for producing transparent parts usable for optical applications. This thesis aims to solve some of the complications of FDM to develop a cheap, rapid, and accessible methodology for printing efficient LSCs.

Similar to modeling, device characterization has been limited to rectangular LSCs, so a standardized methodology for evaluating device efficiency has been developed, allowing for comparison between different device shapes.

The simulated results of this study indicate 3D printed devices have the potential to offer a twofold increase in efficiency over conventionally manufactured bulk devices. Actual 3D printed devices were measured to have similar efficiency to bulk devices (within 1%), but extrapolating the results to parts made with higher quality material also suggests some parts would have twice the efficiency of their bulk counterparts. 3D printed parts may have additional benefits in improving directionality of edge-emitted light, but this will have to be confirmed in future work.

Overall, 3D printing provides major benefits over conventional manufacturing techniques, as it introduces rapid prototyping by allowing experimental iteration and model validation, allows custom-built designs for easier integration into the built environment, and increases the optical efficiency of devices by improving light transport pathways. With further development, this technology can help make widespread solar adoption a reality.

IV. List of Abbreviations

A – absorbance	MMA – methyl methacrylate
ABS – acrylonitrile butadiene styrene	MW – molecular weight
AM1.5G – air mass 1.5 global	n – refractive index
α – absorption coefficient	NREL – National Renewable Energy Laboratory
B – spectral radiance	η_{ext} – external photon efficiency
c – concentration	η_{int} – internal photon efficiency
c – speed of light	η_{trap} – trapping efficiency
CAD – computer aided design	PCE – power conversion efficiency
CSD3 – Cambridge Service for Data-Driven Discovery	PDMS – poly(dimethylsiloxane)
DIW – direct ink writing	PETG – poly(ethylene terephthalate glycol)
DLP – digital light processing	PLA – poly(lactic acid)
DPA – diphenylanthracene	PLQY – photoluminescence quantum yield
ϵ – attenuation coefficient	PMMA – poly(methyl methacrylate)
FDM – fused deposition modeling	ppm – parts per million
GUI – graphical user interface	PV – photovoltaic(s)
h – Planck constant	Φ_{PL} – photoluminescence quantum yield
I – light intensity	QD – quantum dot
k_B – Boltzmann constant	SLA – stereolithography
L – path length	STL – stereolithography
LC – liquid crystal	T – temperature
LED – light emitting diode	θ_c – critical angle
LR305 – Lumogen F Red 305	UV – ultraviolet
LSC – luminescent solar concentrator	wt – weight
λ – wavelength	

Table of Contents

1. Introduction	3
2. Literature Review	6
2.1. Overview of LSCs	6
2.1.1. LSC Operation	6
2.1.2. Optical Loss Mechanisms	7
2.1.3. Novel LSC Designs	9
2.2. Overview of 3D Printing	15
2.2.1. Common 3D Printing Technologies	15
2.2.2. 3D Printing of Photoluminescent Objects	18
2.3. Printed LSCs	20
2.3.1. 2D printed LSCs	20
2.3.2. Printed Negative Masters/Molds	22
3. Thesis Aims	24
4. Methodology	27
4.1. CAD Model Generation	28
4.2. Ray-Tracing Simulation	33
4.2.1. pvTrace background	34
4.2.2. Inputs to pvTrace	34
4.2.3. Changes to pvTrace	37
4.2.4. Experimental Verification of pvTrace Modifications	39
4.2.5. pvTrace Graphical User Interface (GUI)	40
4.2.6. pvTrace parallelization	41
4.2.7. Ray tracing of 3D printed parts	43
4.3. Luminescent Filament Preparation	43
4.3.1. Lumophore Incorporation	44
4.3.2. Filament Extrusion	45
4.4. 3D Printing Parts	46
4.5. Optical Characterization	47
4.5.1. Basic Optical Characterization	48

4.5.2.	<i>Optical Efficiency Measurement</i>	48
5.	Results and Discussion	51
5.1.	STL Generation	51
5.2.	Ray Trace Analysis.....	53
5.2.1.	<i>Bulk vs. 3D Printed LSCs</i>	53
5.3.	Luminescent Filament Generation	58
5.4.	3D Printing.....	61
5.4.1.	<i>Plain PMMA Parts</i>	61
5.4.2.	<i>Luminescent Parts</i>	65
5.4.3.	<i>Bulk parts</i>	68
5.5.	Optical Characterization.....	69
6.	Future Work	76
7.	Conclusions	78
8.	References	80
9.	Appendix	85
9.1.	Literature Review	85
9.1.1.	<i>3D Printing Photoluminescent Parts</i>	85
9.2.	Experimental.....	87
9.2.1.	<i>Software</i>	87
9.2.2.	<i>Materials</i>	103
9.2.3.	<i>Instrumentation</i>	109
9.3.	Additional Data	116
9.3.1.	<i>LSC edge emission</i>	116
9.3.2.	<i>Optical Efficiency Data</i>	118
9.3.3.	<i>Scattering Data</i>	119

1. Introduction

In recent years, there has been increasing urgency to develop inexpensive, efficient solar devices, with an abundance of research being conducted in this area.¹⁻⁶ The field of photovoltaics (PV), featuring the direct generation of electricity from sunlight, has seen exceptional growth,⁷⁻¹⁰ with a variety of interesting technologies emerging beyond conventional silicon cells, including perovskites,^{11,12} thin film PV,¹³ and organic PV.¹⁴ However, additional solar technologies beyond PV must be developed in order to achieve a truly carbon-zero future. One particular issue with PV devices is their form; since modules are typically bulky, dark, and rectangular, integration into the built environment is non-trivial.¹⁵ A promising technological solution that may help solve this problem is the luminescent solar concentrator (LSC).¹⁶

A typical LSC is composed of a flat plate doped or coated with a luminescent dye. The dye absorbs sunlight and re-emits light at a longer wavelength towards the edges of the plate, where solar cells can be installed. The plate also acts as a waveguide to help the re-emitted light from the dye reach the edges through total internal reflection. A schematic of an LSC is shown in Figure 1(a). LSCs are colorful and semi-transparent, as seen in Figure 1(b), and can come in a variety of different shapes. Additionally, as a concentrator technology, they reduce the area of expensive solar cells. They are also able to utilize diffuse light, setting them apart from other concentrator technologies. Due to all of these characteristics, LSCs are favorable over conventional PV modules for built environment integration.

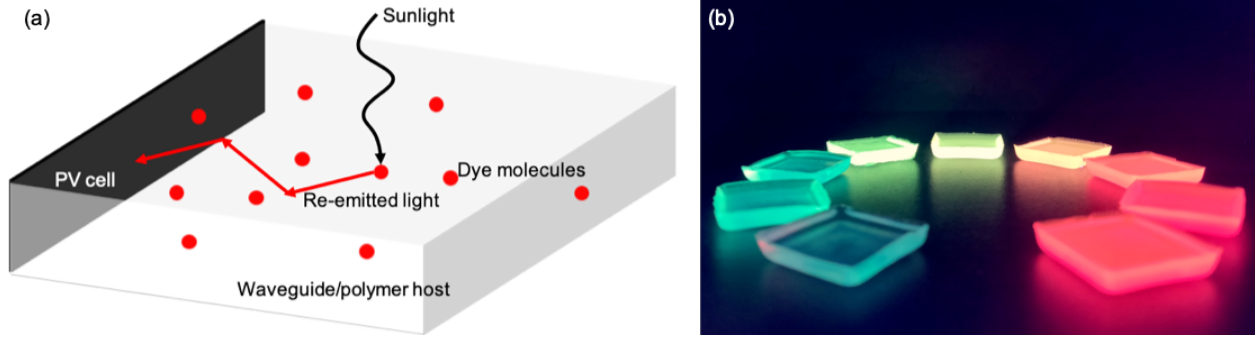


Figure 1: (a) Schematic of an LSC showing incident sunlight hitting a dye molecule, being absorbed, and being re-emitted through the waveguide/polymer host material to the edge, where a PV cell is installed. (b) Image of LSCs of various colors, demonstrating their favorable characteristics: semi-transparency, ability to concentrate light towards their edges, and utilization of diffuse light. Image courtesy of Guanpeng Lyu.

While LSCs are a useful complementary technology to PV, they unfortunately suffer from several optical losses that limit the amount of incident sunlight that eventually reaches the PV cells.^{17,18} Several different device shapes such as cylinders, wedges, polygons, and curved LSCs have been proposed to reduce these optical losses, but there has been limited success due to the restrictions of conventional manufacturing techniques.¹⁵ The development of novel manufacturing techniques such as 3D printing may help increase the optical efficiency of these devices.

3D printing, also known as additive manufacturing, is the process of building a part layer by layer, as opposed to subtractive manufacturing which starts with a bulk object and gradually removes material until the desired part is created.¹⁹ 3D printing is a rapidly advancing technology, primarily due to its ability to create objects that would be impossible to fabricate using traditional subtractive manufacturing techniques.²⁰ Other manufacturing techniques such as injection molding may be able to create similarly complex designs, but 3D printing allows for flexibility in design as it does not require a pre-made mold, thus allowing multiple design iterations to take place rapidly.²¹ One downside of 3D printing is it is relatively slow to manufacture individual parts, so once an ideal design has been achieved, techniques such as injection molding can be used to mass-produce parts. Regardless, 3D printing holds great promise.

While 3D printing of a variety of materials has been achieved,²²⁻²⁵ polymer 3D printing has achieved especially great commercial success, with many polymer 3D printers available on the mass market.²⁶ Printed objects are typically inert, but additives can be included in the polymer precursors to give prints functionality, allowing 3D printed objects to be applied to various fields.²⁷

The specific field of interest for this thesis is 3D printing of polymer materials for solar devices. 3D printing of polymer solar cells has been investigated previously and is an area for future growth.²⁸⁻³⁰ However, the focus of this thesis will be 3D printing of LSCs. Most bulk LSCs are simply photoluminescent polymer composite materials, with the waveguide being the polymer host and the dye molecules being the dopant. Since 3D printing of polymer composites has significant precedent in literature, printing of LSCs is a possibility.

3D printing of LSCs would allow them to take on a variety of novel shapes, both increasing their efficiency and allowing them to be incorporated into buildings in new, unique ways. 3D printing would also allow rapid prototyping, providing the ability to improve designs until optimal optical efficiency is achieved while also allowing valuable real-world validation of optical modeling. The following section provides an overview of the literature on the applications of 3D printing to LSCs.

2. Literature Review

2.1. Overview of LSCs

2.1.1. LSC Operation

A typical LSC is composed of a large, flat, usually square or rectangular slab doped or coated with a luminescent dye. The dye absorbs incident sunlight and re-emits light at a longer wavelength tailored for solar cells. It is the responsibility of the waveguide to ensure the greatest amount of light is captured and guided to the edges of the plate. This is accomplished by using a material with a high refractive index, allowing most of the emitted light to be totally internally reflected towards the edges of the plate. For example, a material with refractive index 1.5 will trap around 75% of emitted light, based on the trapping efficiency:

$$\eta_{trap} = \sqrt{1 - \frac{1}{n^2}}, \quad (1)$$

where n is the refractive index of the material.³¹ The light-trapping properties of the waveguide cause light to be concentrated from the large top surface of the flat plate to the narrow edges. PV cells can be installed on these edges, generating clean electricity (see Figure 1). Bulk LSCs, in which the entire polymer slab is doped with a luminescent dye, are the most common device type.³² Poly(methyl methacrylate) (PMMA), shown in Figure 2(a), is a commonly used polymer host³³⁻³⁵ due to its stability, transparency, and refractive index of ~ 1.5 . Lumogen F Red 305 (LR305), shown in Figure 2(b), is a commonly used dye^{31,36} due to its high photoluminescence quantum yield (PLQY), strong visible absorption, and suitable emission wavelength maximum of ~ 610 nm.³⁷

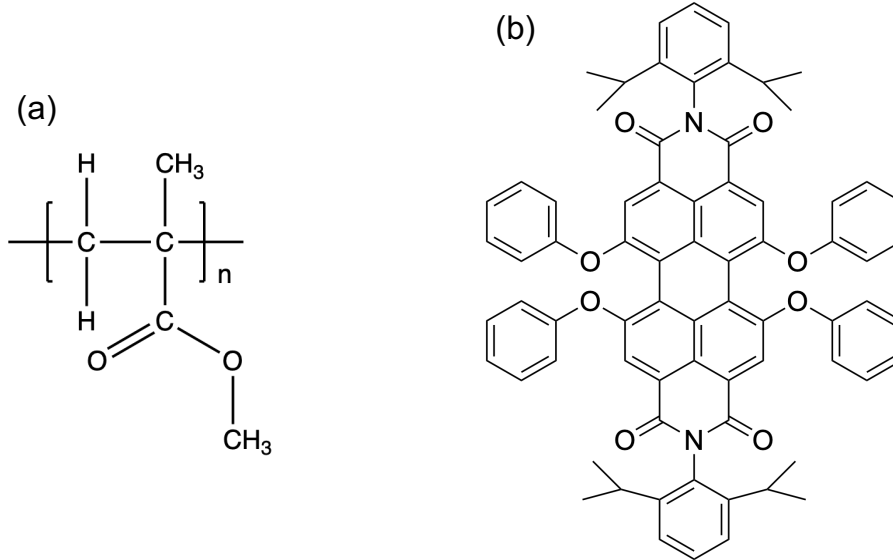


Figure 2: Chemical structures of (a) PMMA and (b) LR305. PMMA is commonly used as the polymer host for LSCs, while LR305 is commonly used as the lumophore.

2.1.2. Optical Loss Mechanisms

Ideally, all incident light would be absorbed by the dye, re-emitted, and guided to the edges of the LSC. In practice, this is not realistic. In many cases, the dye is not able to absorb all incident light, so light may be transmitted through the LSC. Further, losses exist within the dye, as many dyes have less than 100% PLQY (Φ_{PL}), defined as:

$$\Phi_{PL} = \frac{\# \text{ photons emitted}}{\# \text{ photons absorbed}}, \quad (2)$$

meaning not all of the light that is absorbed gets re-emitted.¹⁸ However, issues with the waveguide contribute most to optical loss.³⁸ There are several mechanisms for waveguide optical losses, depicted in Figure 3(a).

First are escape cone losses. The purpose of the high refractive index waveguide material is to trap light emitted from the dye. As shown in Figure 3(b), the high refractive index creates a critical angle, θ_c , such that any light emitted at a greater angle is totally internally reflected. However, if the dye emits light at a smaller angle than the critical

angle, the photon may leave the LSC instead of being waveguided to the edges through total internal reflection.¹⁵ As discussed earlier, at least 25% of photons will leave the LSC in this way,³¹ but these losses can be amplified depending on the dye alignment and have been shown to be up to 50%.³⁹ Second, the re-emitted light may be re-absorbed by another dye molecule if the wavelength of the re-emitted light is within the absorption spectrum of the dye (for example, Figure 3(c) shows the spectra for LR305 – if a photon is emitted in the 525-600 nm region, there is a possibility of re-absorption by another LR305 molecule).^{40,41} Third, the waveguide itself may absorb some light, and even trace amounts of absorption in the visible region can harm LSC performance.¹⁵ Finally, the waveguide may scatter light due to imperfections in the bulk material or the surface.³⁹ All of these factors contribute to lowering the overall efficiency of the LSC.

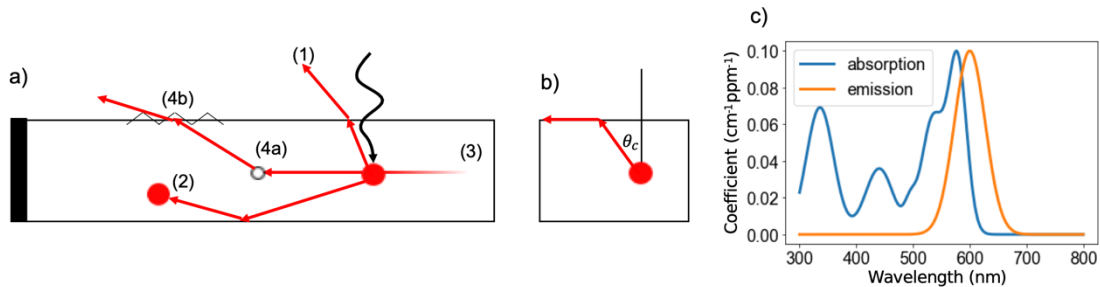


Figure 3: (a) Schematic depicting the various waveguide optical losses of an LSC. (1) escape cone losses, (2) reabsorption, (3) waveguide absorption, (4a) waveguide scattering, and (4b) surface scattering. (b) Schematic demonstrating the critical angle of a waveguide (c) absorption and emission spectrum for LR305 showing overlap leading to dye reabsorption.

There are three primary measures of efficiency for LSCs. First is the internal photon efficiency (η_{int}), which divides the amount of light exiting the LSC’s edges by the light absorbed by the LSC. Second is external photon efficiency (η_{ext}), which measures the amount of light exiting the LSC’s edges versus the incident light on the LSC’s frontal surface, thus also taking into account transmission losses. Last is power conversion efficiency (PCE), defined as the fraction of incident power that is converted to electricity, which additionally takes into account the efficiency of the PV cell used. While these three

methods of reporting efficiency are most common, there is lack of standardization of measurement procedures, especially when considering the variety of sizes and shapes of LSCs. Regardless, many devices exhibit low efficiency when compared to the maximum theoretical PCE of an LSC at 20%, calculated by taking into account the various losses discussed above.⁴² For example, Desmet *et al.* fabricated a stacked red/blue LSC with a PCE of 4.2% using GaAs cells placed on the 2 edges of the LSC, mirrors on the other 2 edges, and a diffuse reflector on the back.⁴³ Clearly, there is significant room for improvement for LSCs. Several research groups have proposed alternative LSC designs, some of which will be detailed in the following section.

2.1.3. Novel LSC Designs

Several previous works have aimed to reduce optical losses with novel LSC designs. It was initially believed that collector geometry had little effect on device efficiency;⁴⁴ however, modern techniques and new technologies have made significant advances in increasing device performance. These advances can be separated into 2 main categories: novel dye patterning and novel device shapes.

2.1.3.1. Dye Patterning

Dye patterning helps reduce reabsorption losses and improve light transport pathways for emitted light. One of the most basic strategies is to separate the waveguide and polymer host/luminescent material by depositing the polymer host as a thin film above (or below) the bulk waveguide, as shown in Figure 4(a).⁴⁵ This ensures that the absorption of light and guiding to the edges are physically separated phenomena, decreasing the number of dye molecules encountered by the transported light and thus reducing the probability of reabsorption.

While thin film LSCs are effective to limit reabsorption to some extent, patterned thin film LSCs, shown in Figure 4(b), would reduce reabsorption even further. Tsoi *et al.* investigated this dye patterning strategy by spin-coating a substrate with the luminescent precursors but using a shadow mask to only polymerize certain areas of the LSC, using ethanol to etch away the unreacted material.⁴⁵ They found a 70% increase in η_{int} for a 30% covered LSC versus a 100% covered control sample, corroborating their claim of reduced reabsorption loss.⁴⁵ However, the big issue with this design is the reduced overall power produced, since less light is absorbed due to greater transmission losses caused by lower coverage.

Another similar strategy developed by Albers *et al.* involves stacking 2 single-side patterned LSCs with an air gap in between to retain waveguide functionality, shown in Figure 4(c). This device exhibited increased η_{ext} compared to a 100% covered thin film LSC (17.4% vs. 16.3%).

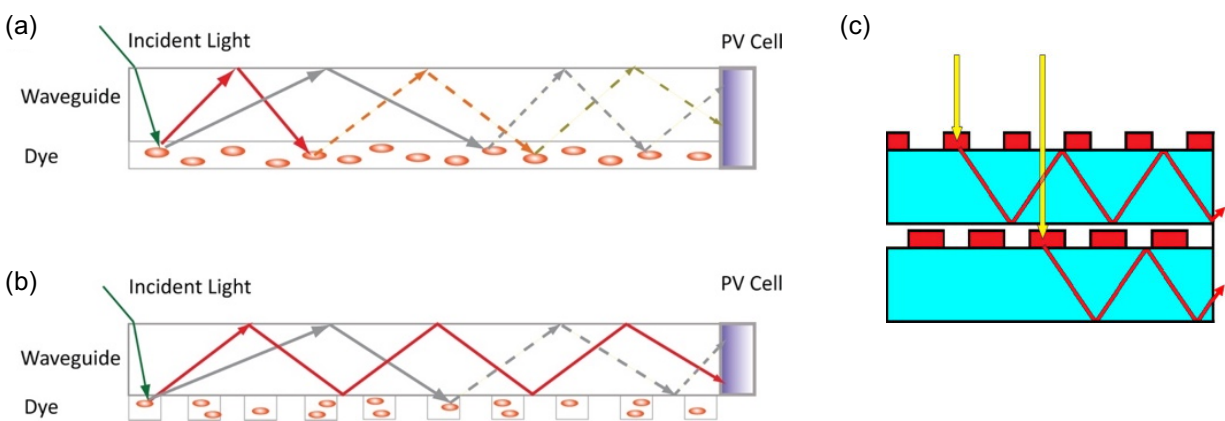


Figure 4: Dye patterning strategies in thin film LSCs to limit reabsorption losses. (a) Thin film LSC with dye/polymer host only located on a thin film at the bottom. (b) Dye line patterning featuring limited coverage of the bottom of the LSC, decreasing reabsorption by reducing probability of re-emitted light hitting another dye molecule. (d) 2 thin film patterned LSCs (summing to 100% coverage) stacked with an air gap in between to retain waveguide properties. (a,b) Reprinted from Tsoi *et al.* with permission from Optical Society of America.⁴⁵ (c) Reprinted from Albers *et al.* with permission from Elsevier.⁴⁶

As mentioned before, it is difficult to extrapolate the results from these studies due to the lack of standardization in efficiency measurement. While the general techniques are consistent, variables within each LSC such as waveguide thickness, dye concentration, etc. may influence the results. Thus, the general trend should still remain valid, but the specific numbers should not be directly compared.

Beyond patterning the bulk dye material, it is possible to align the individual dye molecules to deliberately direct light towards a certain direction. Verbunt *et al.* used dichroic organic dye molecules embedded in a liquid crystal (LC) host as the thin film covering for the LSC, creating a self-assembly procedure by spin-coating the LC composite onto a pre-treated alignment layer on a PMMA substrate.⁴⁷ The alignment layer (composed of poly(vinylalcohol) (PVA)) was spun onto the substrate, cured, then rubbed in a planar (x - or y - direction, as shown in Figure 5(a)) fashion which forced the dyes in the LC host to follow that orientation.⁴⁷ They were able to achieve 60% greater emission from the preferred edge than the non-favored edge, showing that the dye alignment was successful in directing light transport.⁴⁷

Bruijnaers *et al.* extended this idea, using the same procedure to align the dichroic dye molecules in a “theater” or “quarter-circle” configuration, as shown in Figure 5(b,c).⁴⁸ A PV cell was placed at the predicted focal point of the configuration, and the short circuit current of the cell was measured as an indication of amount of emitted light incident at that point.⁴⁸ The aligned LSCs featured a 33% greater short circuit current compared to LSCs with an isotropic dye pattern.⁴⁸ These two studies are promising and indicate dye alignment in a variety of shapes is possible – thus, the mean length of the light transport pathway could be minimized, reducing the chances of encounter with another dye molecule and increasing η_{int} .

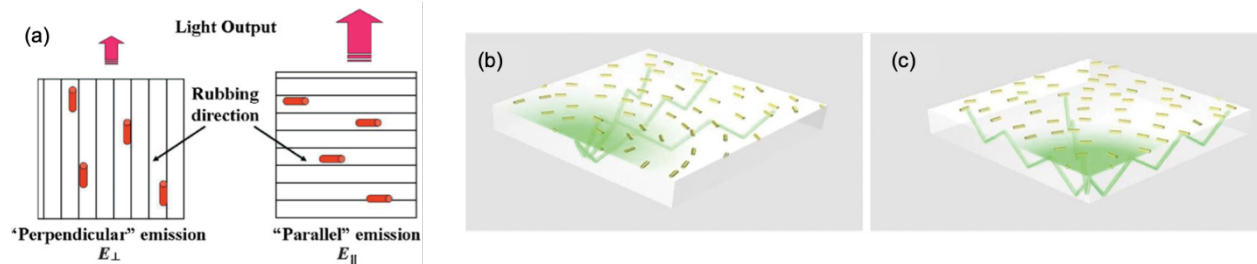


Figure 5: (a) Schematic showing examples of dye alignment for thin film LSCs. Dye molecules within an LC host were aligned through self-assembly to follow either the x - or y - axis. The size of the arrow corresponds to the magnitude of light output at the top edge for each alignment direction. (b,c) Schematics of different types of dye alignment of dichroic dye molecules within an LC host. Showing the (b) theater configuration and (c) quarter circle configuration for dye alignment, as well as the expected light transport pathways. A PV cell placed at the focus was used to measure light intensity. (a) Reproduced from Verbunt *et al.* with permission from Wiley-VCH Verlag GmbH & Co. KGaA.⁴⁷ (b,c) Reproduced from Bruijnaers *et al.* with permission from Wiley-VCH Verlag GmbH & Co. KGaA.⁴⁸

2.1.3.2. Device Shapes

The next major category of innovations in LSC design has been in device shape. The traditional LSC is shaped as a large, flat rectangular block. However, a variety of additional shapes have been investigated since LSCs were originally proposed.

The first common alternative LSC shape is a cylinder. Inman *et al.* made cylindrical LSCs (both filled and hollow, shown in Figure 6(a)) with quantum dots (QDs) in PMMA as an alternative to flat LSCs, noting a 12% increase in η_{int} from flat to filled and a further 10% increase from filled to hollow, giving a final η_{int} of 53% and η_{ext} of 6.7% for hollow LSCs.⁴⁹ Correia *et al.* created red-emitting cylindrical LSCs with PMMA-based optical fibers coated with a ureasil layer (shown in Figure 6(b)), achieving a η_{ext} of 26.5% and PCE of 2.5%.⁵⁰ Related work in modeling cylindrical LSCs confirms their benefits.^{51,52}

Another potential LSC shape is curved LSCs, as shown in Figure 6(c), investigated by Vishwanathan *et al.*⁵³ They found a 3% increase (18% to 21%) in η_{ext} from a flat LSC to the curved LSC.⁵³ Carbone *et al.* developed flexible, circular, front-facing LSCs using polydimethylsiloxane (PDMS) instead of the conventional PMMA, focusing on increasing light gain, and demonstrated a PCE of 1.31%, comparable to conventional devices.⁵⁴

To further investigate the impact of shape on LSC efficiency and cost, Kennedy *et al.* used Monte Carlo ray tracing to model triangular, hexagonal, and circular LSCs (shown in Figure 6(d)).⁵⁵ They calculated the predicted concentration ratio for fixed collector area, finding hexagonal LSCs to be superior, but also finding all geometries to have similar relative cost of power.⁵⁵ Evidently, further research is required to determine the impact of shape on overall collector efficiency.

Beyond these conventional device shapes, more radical LSC designs have also been considered. Hughes *et al.* used Monte Carlo ray tracing methods to model wedge-shaped LSCs, shown in Figure 6(e), and determined an almost fourfold increase in η_{ext} (from 7.6% to 32.8%) compared to flat LSCs for conditions when the sun remains low in the sky.⁵⁶ Reinders *et al.* developed a leaf-shaped, front-facing LSC, shown in Figure 6(f), with a relatively high PCE of 5.8%, demonstrating the versatility of designs possible.⁵⁷

While the previous studies focus on changing just the shape of the LSC, it is also possible to design the overall device in different ways to improve efficiency. Debije *et al.* investigated in detail the effects of a white scattering layer placed below the LSC with an air gap (shown in Figure 6(g)), finding a 37-50% increase in power output from the emission edge of the LSC compared to a similar device with a black background.⁵⁸

Furthermore, Mateen *et al.* installed both an array of cylindrical optical fibers and a white diffuse scattering layer underneath a bulk LSC, as shown in Figure 6(h); they found a 65% increase in PCE (0.55% to 0.91%) compared to a bulk LSC.⁵⁹ Finally, Desmet *et al.* created a stacked LSC with a blue LSC sandwiched between a red LSC and a microcellular poly(ethylene terephthalate) (MCPET) back-reflector, as shown in Figure 6(i) – they were able to achieve an increase in PCE from 2.3% for just the red LSC to 4.2% for the entire setup.⁴³

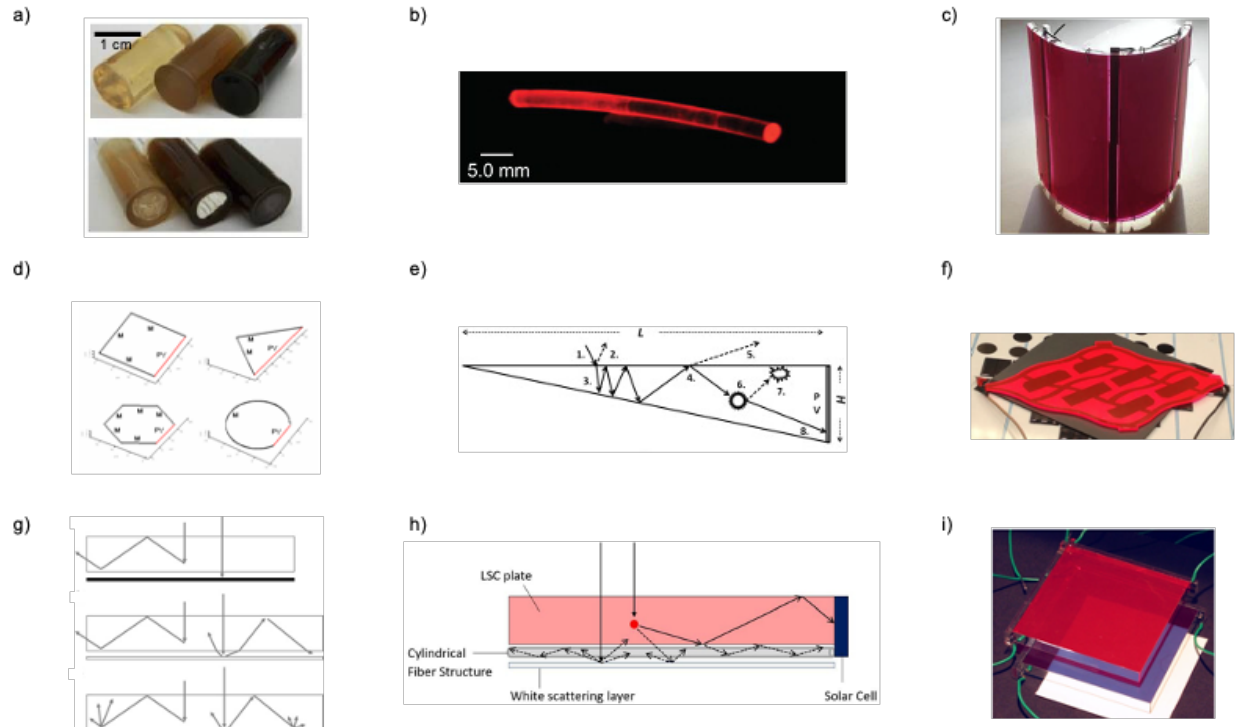


Figure 6: Various novel LSC device shapes. (a) Filled and hollow cylindrical LSCs with NIR QDs, reproduced from Inman et al. with permission from the Optical Society of America,⁴⁹ (b) red-emitting LSC with PMMA core coated with rare earth ion-doped ureasil layer, reproduced from Correia et al. with permission from Elsevier,⁵⁰ (c) curved LSC, reproduced from Vishwanathan et al. with permission from Elsevier,⁵³ (d) LSCs of various polygon shapes, reproduced from Kennedy et al. with permission from Springer Nature,⁵⁵ (e) wedge-shaped LSC, reproduced from Hughes et al. with permission from Elsevier,⁵⁶ (f) leaf LSC, reproduced from Reinders et al. with permission from IEEE,⁵⁷ (g) LSCs with no back reflector, separate diffuse reflector, and attached diffuse reflector, reproduced from Debije et al. with permission from Elsevier,⁵⁸ (h) LSC with cylindrical back absorber with white scattering layer, reproduced from Mateen et al. with permission from Elsevier,⁵⁹ (i) stacked LSC, reproduced from Desmet et al. with permission from the Optical Society of America.⁴³

Many of the above device designs were successful in reducing optical losses faced by conventional LSCs, either by unique dye patterns or new device shapes, despite being created specifically to facilitate incorporation into the built environment. By creating new designs for LSCs, we further develop this potential of creating aesthetic, efficient devices. All of the works above used conventional manufacturing techniques; spin-coating, photopolymerization, *etc.*, resulting in designs being largely confined to two dimensions. This severely limits the possible LSC shapes that can be created. Luckily, 3D printing can solve this issue.

2.2. Overview of 3D Printing

Before discussing the application of 3D printing to LSCs, it is first necessary to detail the 3D printing process itself. The first step is to create a computer-aided design (CAD) model of the part to be printed.⁶⁰ The model is then converted to a stereolithography (STL) file which tessellates the various contours of the CAD model into small triangles.⁶⁰ The STL file can then be sliced with software to generate layers and a support structure, and the subsequent instructions are saved as G-code, a type of machine code that tells the 3D printer how to print the part.⁶⁰ The most common 3D printers use fused deposition modeling (FDM), inkjet printing, or stereolithography (SLA), which are described in more detail in the section below.²¹

2.2.1. Common 3D Printing Technologies

FDM, also known as fused filament fabrication, is arguably the most common 3D printing technology, especially for commercial and hobbyist use.⁶¹ FDM consists of a filament pushed through an extruder nozzle onto a build plate, as shown in Figure 7(a).⁶¹ The polymer filament used is heated above its glass transition temperature to flow smoothly through the nozzle. The nozzle moves in the x - and y -directions to deposit each layer in a specified pattern, while the print bed moves in the z -direction to allow the nozzle to build the object layer by layer. Once deposited, the polymer cools to form a solid 3D object. Acrylonitrile butadiene styrene (ABS) and polylactic acid (PLA) are the most common polymers used in FDM 3D printers, but a variety of other polymers (and materials in general) can also be turned into filament and printed.²⁰ FDM is popular due to its low cost, high speed, and relatively simple filament manufacturing process. However,

the main drawbacks include discernable layers (low resolution due to relatively large nozzle sizes of ~ 0.4 mm), weak mechanical properties, and uneven surface finish.²⁰

Inkjet printing is the next main type of 3D printing technology.⁶² The most common form of inkjet printing is drop-on-demand, in which individual droplets of ink are ejected from a nozzle onto a print bed through a piezo-electric pulse, as shown in Figure 7(b).⁶³ The ink is usually made up of a fast-drying solvent with some type of structural material that forms the printed part after the ink dries. To achieve proper deposition, the ink must have a variety of specific fluid properties such as relatively high surface tension and low viscosity.⁶⁴ A major benefit of inkjet printing is its solution-based processing. Additional benefits include fine control over deposition (~ 100 μm). On the other hand, high resolution comes at the cost of long processing times. Additionally, one of the main problems with inkjet printing is ring formation, where most of the structural material is deposited on the outer rim of the droplet after the solvent evaporates; to solve this, a mixture of solvents is often used.⁶²

Stereolithography (SLA) is another commonly used 3D printing technique, shown in Figure 7(c).⁶⁵ In SLA, a resin reservoir is scanned with a focused UV laser that solidifies the surface to a certain depth, securing it to a build platform. Then, the platform is moved such that the solid resin is exposed to more liquid resin, and the process is repeated. SLA has various benefits: it enables high-resolution parts over a wide variety of scales (~ 100 μm to ~ 1 cm), and SLA parts typically have a better surface finish than FDM parts. However, SLA is messy, requires post-processing, is limited in terms of resin-compatible materials and involves UV photopolymerization, which may threaten the stability of some components.⁶⁶ Similar technologies to SLA are digital light processing (DLP), in which a light image is projected onto the resin bed, and two-photon polymerization, which offers higher resolution (~ 100 nm) but requires much longer time and higher cost.⁶⁷

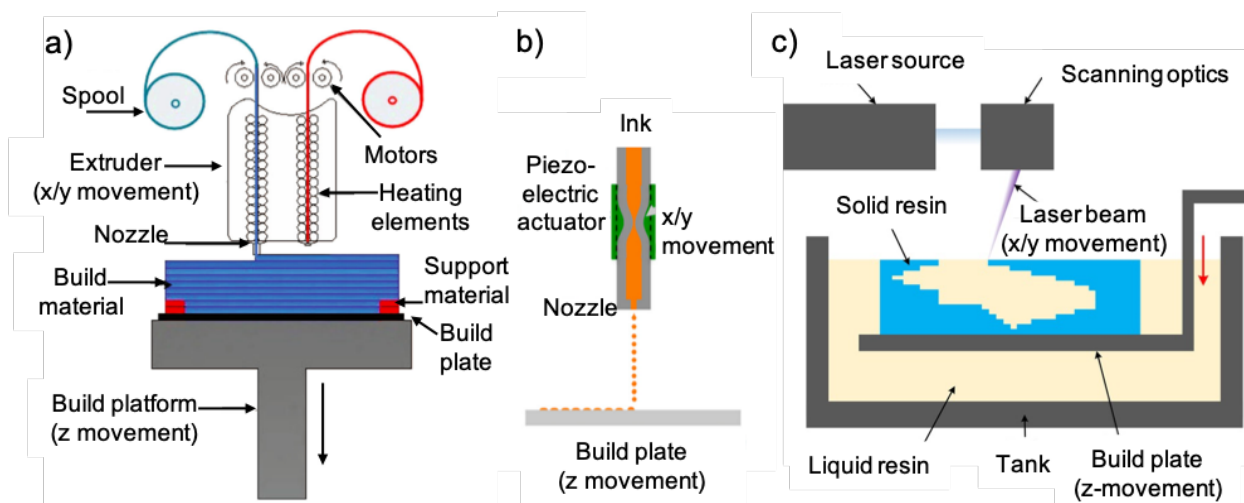


Figure 7: Schematics of the most common types of 3D printing techniques: (a) fused deposition modeling (FDM), in which a plastic filament is extruded through a nozzle and deposited onto a print bed. Reproduced from Mohamed et al. with permission from Springer Nature.⁶¹ (b) inkjet printing, in which individual droplets are deposited onto a print bed. Reproduced from Alamán et al. with permission from MDPI.⁶⁴ (c) stereolithography (SLA), in which a rastering laser solidifies layers of liquid resin. Reproduced from He et al. with permission from Wiley-VCH Verlag GmbH & Co.⁶⁵

The development of multiple 3D printing types reflects its significance. 3D printing enables rapid prototyping, allowing users to go from a computer model to a physical part in the matter of hours. On the other hand, it can provide immense detail, with resolutions on the scale of micrometers for some printing technologies. However, 3D printing is most commonly used to print inert parts, which are not useful for applications in chemistry.

There are two main ways to add chemical functionality to 3D printed parts. The first is grafting (covalently bonding) functional groups to the polymer chain. This is most commonly done with nanoparticles⁶⁸ or organic substituents.⁶⁹ The other option is doping the polymer with materials that are not bonded to the chain but are still active agents. Such additives can be nanoparticles,^{70,71} porosity-inducing materials,⁷² photoluminescent additives,⁷³ or 2D materials.⁶⁷

The current study is interested in using these methods of adding chemical functionality to 3D print photoluminescent parts, discussed in the following section.

2.2.2. 3D Printing of Photoluminescent Objects

The fundamental process of photoluminescence can be explained in two steps. First, a molecule absorbs high-energy photons, causing the excitation of its electrons to a higher energy state. Then, the electrons relax down to their ground state and emit lower energy photons – this emission of light is known as photoluminescence. Figure 8 shows the basic principles of molecular absorption and photoluminescence.

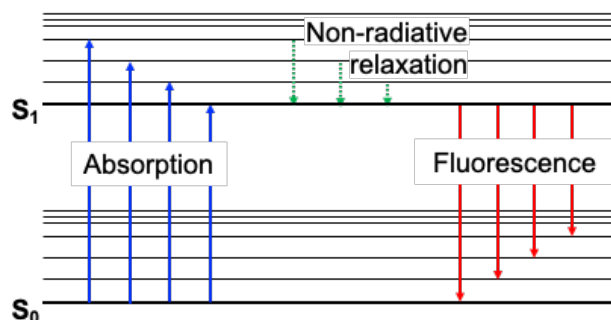


Figure 8: Schematic showing the principles of molecular fluorescence. Light absorption causes electrons to be excited to various vibrational energy levels of a higher energy singlet state (S_1). Non-radiative relaxation then occurs to bring the electron down to the lowest energy level of the high energy singlet state. The subsequent radiative relaxation to the ground singlet state (S_0) is known as fluorescence.

Unfortunately, most commonly used polymers in 3D printing are not inherently photoluminescent. In order to make the resulting print glow, luminescent materials must be added to the polymers in one of the two methods mentioned above, covalent-grafting or doping. The most common luminescent materials used are quantum dots (QDs), rare earth ions, or organic dyes. Several past studies have successfully 3D printed photoluminescent parts using various printing techniques, as summarized in Table 1. More detail about these studies is provided in Appendix Section 9.1.1.

Many of the studies created test parts as proof of concepts (PoC) for the proposed luminescent additive manufacturing technique proposed. A few mentioned applications in light emitting diodes (LEDs)^{74,75} or optics and waveguides.^{76,77} However, the current study is particularly interested in the application of photoluminescent 3D printing to LSCs, discussed in detail in the following section.

Table 1: Summary of works involving photoluminescent 3D printing. Includes all major types of lumophores (quantum dots, rare earth ions, and organic dyes) doped in a variety of polymer hosts to achieve various types of 3D printing (inkjet, SLA, FDM).

Lumophore	Polymer Host	Printing Method	Key Results	Application / PoC	Ref.
QD (CdSe/ZnS)	PS	Inkjet	Green, orange, red emitting inks.	Pixelated display	78
QD (CdTe)	PVA	Inkjet	Green and red emitting inks, prevented ring formation.	Array of dots	79
QD (carbon)	Sodium polyacrylate	SLA	Orange emitting solid-state parts.	Fluorescent Statue of Liberty	80
QD (CdSe/ZnS)	ORMOCER	SLA	Multicolored cubic voxels (blue, green, red, yellow).	Multicolor block display	76
QD (CdSe/CdZnS)	ORMOCER	Two-photon	Used functionalized silica shell to bond to polymer host. Multicolored luminescence (blue, green, red).	Patterned photonic materials	81
QD (CdSSe)	PLA	FDM	Graded alloy of S/Se. Solvent casting, shredding, extrusion to produce orange/red filament.	Logo using fluorescent filament	82
QD (FAPbBr ₃)	PCL	FDM	Perovskite nanocrystals encapsulated in polymer matrix.	White LED	75
Rare earth (SrAl ₂ O ₄ :Eu ²⁺ , Dy ³⁺)	PLA	FDM	Green fluorescent filament using melt blending.	Fluorescent furniture	83
Rare earth (MgAl ₂ O ₄ :Sm ³⁺)	PLA	FDM	Powders modified with 3-aminopropyl triethoxysilane to produce purple filament.	Samples for mechanical testing	84
Rare earth (Ru ²⁺ , Ir ³⁺)	PPL+PMMA, PS	Inkjet	Copolymers created orange and yellow inks.	Array of dots	74
Organic dye (Rhodamine B, Solvent Yellow 98, BBOT)	DEGMA	SLA	Also included small stabilizing acrylate monomer. Created red/green/blue resins.	Brightly fluorescent vases	85
Organic dye (NBD-MA)	BEDA	SLA	Printed yellow fluorescent parts.	Optical waveguides	77

2.3. Printed LSCs

By using 3D printing technology, it would be possible to increase the dimensionality of parts, vastly expanding the potential designs that can be created. It would also make manufacturing all of the above parts much easier. For dye patterning, instead of having to create a specific mask for each pattern required, each design could be coded into the same generic 3D printer, saving time, effort, and materials. For device shape, since all of the above designs are all essentially extrusions of two-dimensional shapes, a 3D printer could easily manufacture them. Additionally, the printer would allow rapid prototyping and characterization, letting the user quickly verify stimulated results and iterate more effectively to find the most efficient design.

2.3.1. 2D printed LSCs

There are already some works that feature printed LSCs, though in a limited sense. The first category of such devices is 2D printed LSCs. Renny *et al.* developed cheap, easy-to-use multicolor paints that can be manually applied on top of bulk, clear PMMA waveguides to create simple LSCs for art or education purposes.⁸⁶ They use coumarin 153, rhodamine 6G, hexamethylindotricarbocyanine perchlorate, rhodamine 640 perchlorate, and SCHEMBL16842984, all dissolved in acetone, as the primary organic dyes, varying the ratio of each to obtain a specific color.⁸⁶ They then added poly(butyl methacrylate-*co*-methyl methacrylate) as the polymer host material in a 2:1 ratio of polymer to dye solution, which created a fairly viscous paint that could be applied easily to the PMMA waveguide.⁸⁶ The participants were able to create a variety of creative designs, one of which is shown in Figure 9(a).⁸⁶ Although the luminescent thin film was applied by manual painting, it is not difficult to conceive a nozzle-based 3D printer using a similar version

of this paint. After each layer of applied paint dries, another layer could be applied, allowing thicker and more innovative shapes to be created.

Another work featuring 2D printed LSCs was conducted by Schiphorst *et al.*, featuring multicolor inkjet printing of LSCs.⁸⁷ While the specifics of the ink used was not included in the paper due to intended commercialization, the dyes used were LR305 and a blue perylene perinone derivative, presumably with a photopolymerizable host, deposited on a PMMA waveguide.⁸⁷ They were able to print a variety of designs using a Dimatix DMP-2850 inkjet printer with a 10 picolitre drop volume, obtaining fairly high resolution of 15 dots per inch, and were able to vary shading by changing the voltage of the nozzle or by increasing the concentration of the dye.⁸⁷ An LED lamp was used during printing to secure the ink onto the PMMA plate, and further polymerization occurred after the print was finished to complete solidification.⁸⁷ Two of the designs generated are shown in Figure 9(b) and (c). Here we see a clear pathway to 3D printing of designs. While inkjet 3D printing would be time-consuming due to the required photopolymerization step between layers, it is theoretically possible to build a 3D object using this technology.

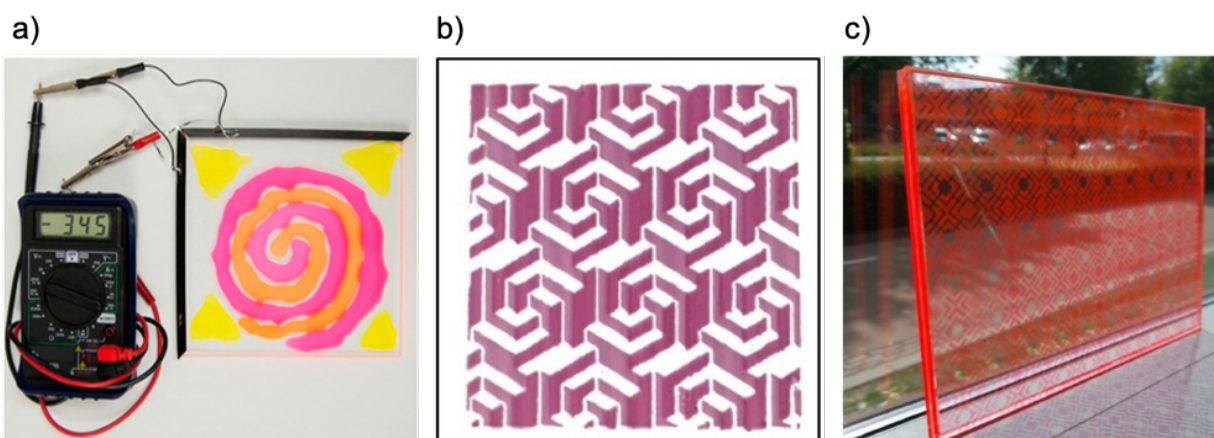


Figure 9: Examples of 2D printed LSCs. (a) Painted LSCs involving luminescent dye dissolved in a viscous solvent manually painted on a PMMA waveguide. Solar cells are attached on 2 edges and the voltage output is displayed on the multimeter. Reproduced from Renny *et al.* with permission from the American Chemical Society.⁸⁶ (b) and (c) inkjet-printed LSCs using Lumogen Red F 305 dispersed in photopolymerizable host (shading produced by changing concentration of dye), reproduced from Schiphorst *et al.* with permission from Elsevier.⁸⁷

2.3.2. Printed Negative Masters/Molds

The other category of current literature in printed LSCs is the development of negative masters. Zhao *et al.* used an FDM printer with high-impact polystyrene filament to create negative molds of an LSC photomicroreactor (two molds were created, one each for the top and bottom of the part).⁸⁸ The actual LSC was made with PDMS, so a PDMS precursor (silicone elastomer with curing agent) mixed with LR305 was poured into both molds and cured. Then, the two halves were bonded together following plasma functionalization.⁸⁸ This process results in a 3D structure in which the traditional bulk rectangular LSC contains flow channels for photocatalyzed reactions to occur, as shown in Figure 10(a).⁸⁸ In this case, the LSC is not directly 3D printed; however, 3D printing is a crucial part of its manufacturing process. Further, it is not infeasible that the actual device be 3D printed with some changes to the methods. The researchers used thermal polymerization to create the PDMS in a vacuum oven, but if the curing agent were to be replaced with a photopolymerization initiator, the same setup could be used in an SLA printer. This would also allow more unique geometries, as the flow channels could additionally be split in the z -direction.

Another example of a 3D printed master used for LSC production is a work by Credi *et al.* involving 3D printed textures to create hydrophobic LSCs.⁸⁹ The textured positive master is comprised of a matrix of cylinders with diameters 80 μm , height 400 μm , and spacing 300-400 μm , created using SLA printing of a DL260 resin.⁸⁹ A PDMS negative mold was then created by pouring a resin with 10:1 ratio of prepolymer to curing agent over the textured master and thermally polymerizing the solution.⁸⁹ Finally, a mixture of monomer precursor and LR305 was poured over the PDMS mold and photopolymerized to create the final microtextured LSC.⁸⁹ SEM images of the resulting LSC surface are shown in Figure 10(b), demonstrating the success of the fabrication

methodology. Because of the high resolution required for this particular application, direct 3D printing of the LSC would take an immensely long time. This is one of the reasons why the study opted to create a polymer master and then use replica molding to create the final LSC. However, for simpler designs, it remains possible that the LSC could be directly printed, for similarly interesting applications.

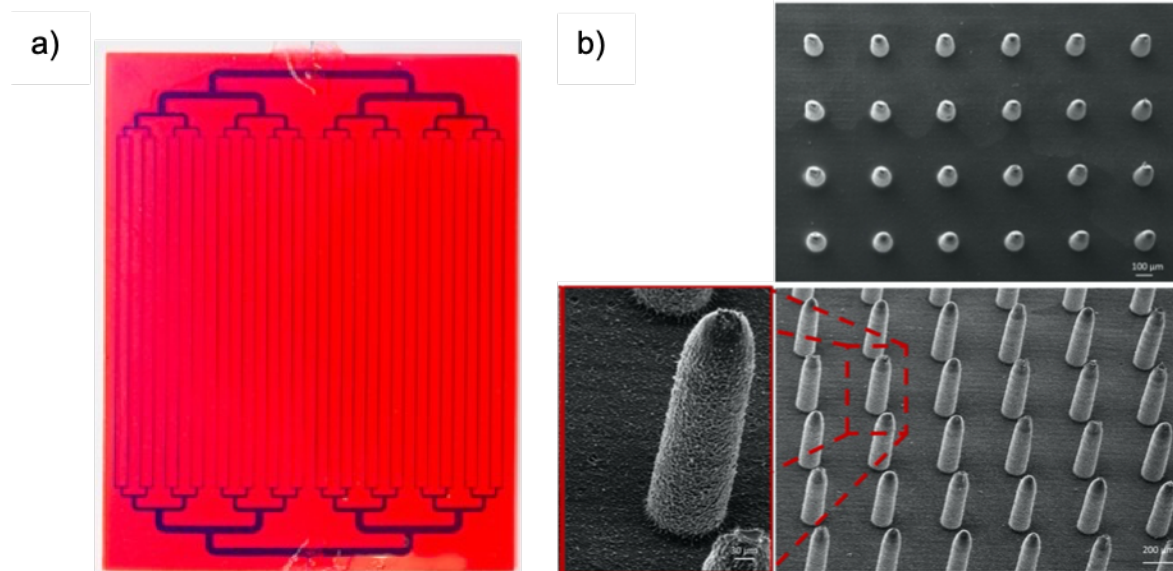


Figure 10: (a) LSC-PM fabricated using a 3D printing negative mold. ABS mold was printed and PDMS monomer precursor was deposited on top. Then surface was functionalized for each half and they were joined. Reproduced from Zhao et al. with permission from the American Chemical Society.⁸⁸ (b) Top, side, and zoomed view of microstructured LSC. First, a master is created using SLA printing of a polymer resin. A PDMS monomer precursor solution is poured over the master and polymerized to form a negative mold. Lastly, the LSC monomer solution is poured into the negative mold and polymerized to form the final product. Reproduced from Credi et al. with permission from Elsevier.⁸⁹

From the examples above, it is clear the fundamentals have been established to allow 3D printing of LSCs. While the previous studies in the field have either focused on 2D printing or used 3D printed molds, slight changes to the synthesis methodology could enable direct 3D printing of LSCs. Thus, this thesis aims to develop 3D printing of LSCs. The goals of this study and an overview of obstacles that must be overcome for success are detailed in the following section.

3. Thesis Aims

There are three main steps to 3D printing LSCs. First, a CAD model of the LSC must be generated. The model's performance can be predicted using ray tracing,⁹⁰⁻⁹² and some preliminary optimization can occur. Second, the LSC must be printed. The specific 3D printing technology must be selected, the required precursors synthesized, and the printing parameters optimized. Third, the printed LSC must be characterized. While researchers understand how to measure optical *vs.* overall efficiency,⁹³ how to separate different types of losses,¹⁸ *etc.*, comparing the efficiency of different devices is difficult, so a standardized characterization technique will need to be developed. Of the three steps, the physical 3D printing of the LSC will likely be the hardest part of this process, since there is little to no precedent. The three most common types of 3D printing introduced in Section 2.2.1 – inkjet, SLA, and FDM – are considered below.

Inkjet printing of LSCs has been demonstrated already, albeit only for 2D printing of thin film LSCs. Inkjet 3D printing could be possible if each dye layer is allowed to dry before depositing the next. However, this would be considerably time consuming. An alternative, more viscous ink could be used, similar to direct ink writing (DIW) printing where a continuous stream of ink is deposited rather than individual droplets. A suitable polymer precursor with desirable viscosity and structural properties must be identified.

SLA printing has great promise in 3D printing of LSCs. UV photopolymerization of luminescent LSC layers is already common practice. For SLA, instead of polymerizing the entire LSC precursor, a focused laser would only harden certain portions. Resin precursors and photoinitiators for LSCs have already been explored in depth, as discussed in Section 2.2.2. In principle, SLA printing should be a natural progression from known techniques towards 3D printing of LSCs.

FDM requires the most extensive development out of the three. While studies have completed FDM printing of luminescent parts,^{75,82} they have primarily relied on quantum dots for luminescence rather than organic dye molecules. However, organic dyes are preferred, as QDs are almost always more toxic⁹⁴ and more expensive.⁹⁵ To the author's knowledge, there is only one paper that generates polymer filament using an organic dye for use in an LSC,⁹⁶ but instead of 3D printing this filament, they use it directly as an optical fiber LSC.

The first step to FDM is generating luminescent filament, which many studies have proven to be possible. First, the luminophore is incorporated in the polymer host material, either through physical mixing,^{83,84} solvent casting,^{75,82} or grafting.⁶⁹ Once a bulk luminescent polymer is generated, it is chopped into fine pellets and fed through a screw extruder to generate filament. The extrusion process must be fine-tuned to determine the correct temperature and extrusion rate to optimize filament quality.

After generating filament, it can be used to 3D print an LSC. Since the filament is cylindrical, post-printing there may still be internal gaps between layers or between adjacently deposited filament. These gaps would alter the light transport pathways of the LSC and could reduce the transparency of the printed LSC. Optimizing the printing parameters would be necessary to print high-efficiency parts.

Despite these challenges, FDM is the cheapest of the common 3D printing methods, so developing a methodology to successfully print LSCs using FDM would be revolutionary. This thesis aims solve many of the complications discussed above to develop a cheap, rapid, and accessible methodology for FDM 3D printing of efficient LSCs. To the author's knowledge, this is the first work to successfully FDM print LSCs doped with organic dye molecules.

The thesis begins with detailing the experimental methodology used. This is split into five distinct steps. First, constructing a computerized 3D model of the LSC. Second, conducting ray-tracing simulation of the model to predict performance. Third, preparing luminescent filament to print the model. Fourth, actual 3D printing of the design. Lastly, characterizing the optical efficiency of the printed part. The cycle can then continue, using the results from optical characterization to drive design improvements.

The results of each of the five steps above are then presented, along with an analysis of the data collected and a discussion of its significance. This is followed by some thoughts on future work to help make 3D printing of LSCs a wide-scale reality. Finally, the findings of this project will be summarized in the conclusions. It is hoped that the development of this novel manufacturing technique for LSCs will help increase the optical efficiency of devices by improving light transport pathways, introduce rapid prototyping to the field allowing quick comparisons to ray-trace modeling, and allow custom-built designs for easier integration into the built environment.

4. Methodology

The methodology for 3D-printing LSCs can be split into five steps, as shown in Figure 11. First, an accurate CAD model of the desired printed part is created. This entails creating a bulk model of the part, importing the model into a slicer software to generate the 3D printing path, then generating a new 3D model of the part based on the 3D printing path. This ensures all of the intricate features of the eventual printed part are included in the CAD model. Second, ray tracing of the CAD model occurs. This is useful to predict the optical performance of the printed part. An accurate ray tracing software that has been compared to experimental results is essential for this step. Third, the luminescent filament is prepared. There are multiple ways to incorporate the lumophore into the polymer host material, as discussed previously. Once the lumophore has been incorporated into the bulk polymer, cylindrical filament is generated by chopping the bulk into pellets and feeding these pellets through an extruder. The fourth step is the actual 3D printing of the part. To ensure widespread use, a commercially available 3D printer without excessive modifications is used. Finally, the fifth step is to characterize the optical efficiency of the printed part, either with actual sunlight and solar cells, or with a solar simulator and a spectrometer. This characterization is useful to compare the light-transport pathways of a 3D printed LSC versus a bulk LSC (a slab/monolith fabricated with conventional manufacturing techniques). If the optical efficiency is lower than predicted by the ray tracing model, this could suggest an inaccurate CAD model of the 3D printed part, limitations of the ray tracing mode, or a more fundamental flaw in the design of the part. The results of the optical characterization can be fed back to the relevant step in the methodology, and another design can be modeled, simulated, printed, and tested. This five-step cycle thus helps achieve optimal parts. The following sections describe these five steps in detail.

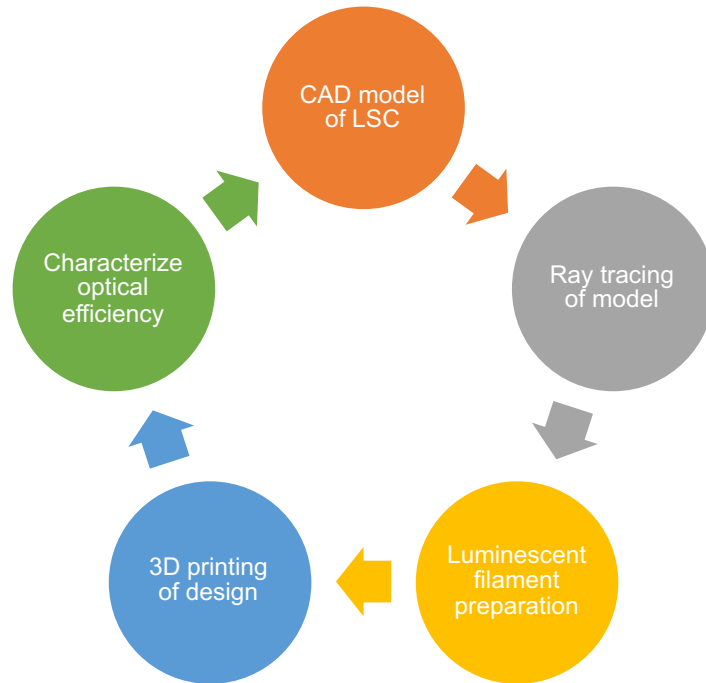


Figure 11: Five-step cycle for the methodology described in this work. An accurate CAD model of the LSC is created and simulated using optical ray tracing techniques. Luminescent filament is prepared for the 3D printing process before the part is actually 3D printed. Finally, optical characterization occurs to calculate the efficiency of the device. The results from optical characterization can be used to optimize the design of the part, and the cycle restarts.

4.1. CAD Model Generation

A rectangular LSC will be used in this section to demonstrate how a 3D CAD model is generated. First, a model of the bulk LSC is created. The geometry of a bulk LSC is equivalent to an LSC fabricated with conventional manufacturing techniques, featuring a homogeneous slab of material. This can be done in any CAD software; Fusion 360 (Appendix Section 9.2.1.1) was chosen for this work. Once the model is designed, it is exported as an STL file that tessellates the geometry of the LSC into triangles. Finally, the STL file is imported into a slicer software that generates layers of the part, as well as a path for each layer that the 3D printer will follow. For this project, Ultimaker Cura was used as the slicer (Appendix Section 9.2.1.2).⁹⁷ These steps, summarized in Figure 12, are part of the conventional 3D printing process for any part.

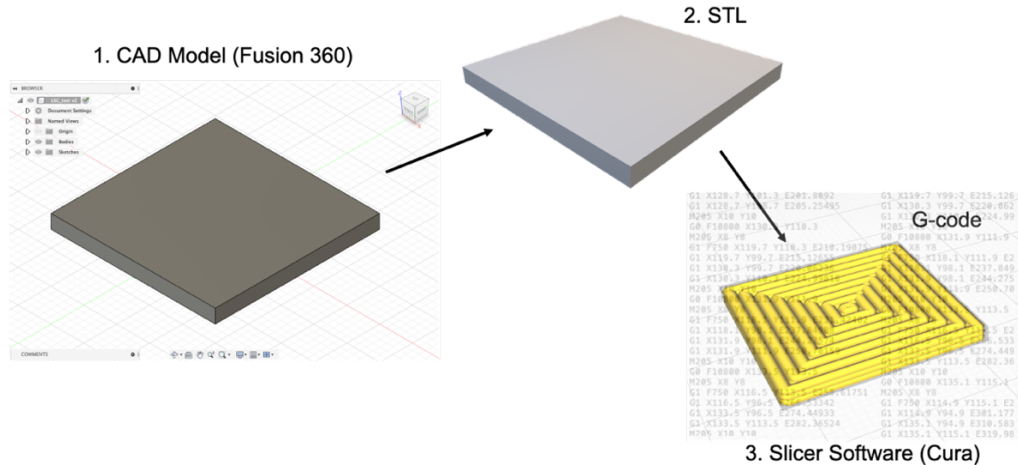


Figure 12: Part 1 of the STL generation process of 3D printed LSCs. These steps are characteristic of any 3D printing project: (1) generated a CAD model of the part, (2) save the CAD model as an STL, and (3) import the STL into a slicer software to generate the 3D printing instructions (G-code) to send to the printer.

At this point, most projects would proceed to the 3D printing step. However, for this study, a new STL file for ray tracing is generated that includes all of the intricacies of the final 3D printed part, including the geometry of the printed path, interfaces, surface characteristics, and air gaps, all of which vastly influence the optical transport pathways. A new STL file can be generated using the layer and path data output by the slicer.

Cura saves the layer/path data as G-code, which is machine code that tells the 3D printer what to do. The G-code then must be parsed to generate an STL of the sliced part. This is done through an open-source Blender add-on that imports G-code and renders a part (Appendix Section 9.2.1.3).^{98,99} The add-on essentially sweeps a cross-sectional profile along a path. The cross-sectional profile is calculated using the line width and height specified, and the path is taken from the x - and y - positions of the extruder.

Unfortunately, as seen in Figure 13(b), using this add-on without modification is inadequate, as the created STL contains separate paths between every 2 points specified by the G-code, instead of connected paths. To fix this, the add-on was modified to continue drawing a single path until the extruder is retracted, which occurs after each path is complete. Adding this modification results in airtight parts, shown in Figure 13(c).

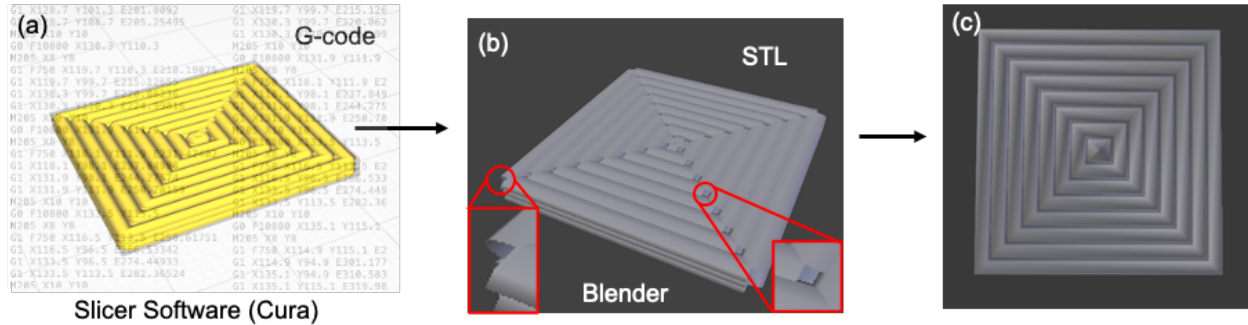


Figure 13: Part 2 of STL generation process. (a) G-code visualization within slicer software, (b) rendering of part provided by Blender add-on for importing G-code, and (c) part resulting from modifying G-code to connect paths.

However, a quick ray-tracing simulation shows that issues arise due to the interfaces generated between layers. As we will see in future sections (5.4.1), these interfaces are practically nonexistent in real-world parts, since the high temperatures of the 3D printing process cause subsequently printed layers to properly fuse with already-deposited layers. In simulation, however, these interfaces play an artificially enhanced role, as seen in Figure 14, which shows an internal view of a few near-infrared rays being traced within a concentric printed plain PMMA part. More detail will be provided about these simulations in Section 4.2, but for now, a few key inaccuracies are immediately evident. Region (a) in Figure 14 shows ray bending, as if there has been a change of refractive index, but the material is the same on both sides of the interface. Further, region (b) indicates one of many reflection events, which should not happen at any significant frequency. The 3D model thus must be updated to eliminate inaccuracies caused by artificial interfaces.

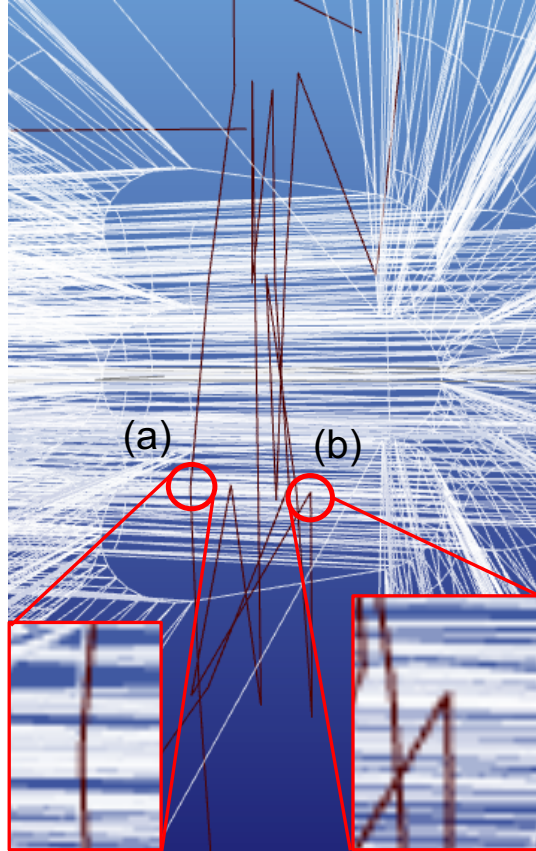


Figure 14: Initial ray tracing simulation of generated CAD model. Note (a) bending of ray as if there is a change of refractive index, and (b) significant reflection events due to interfaces.

This is achieved by changing the cross-sectional profiles used to generate the part. With the built-in settings, the same cross-section is used for each layer. For example, a 3-layer part would have a vertical cross-section as shown in Figure 15(a). Instead, the add-on was updated to change the shape of the cross section based on the layer number. As seen in Figure 15(b), each layer has a different cross section profile. The bottom layer is missing its top face, each middle layer only has its sides, and the top layer is missing its bottom face. Thus, a solid part can be created without intermediary interfaces. Figure 15(c) and (d) show Blender renderings of the before and after results of changing the cross-sectional profile.

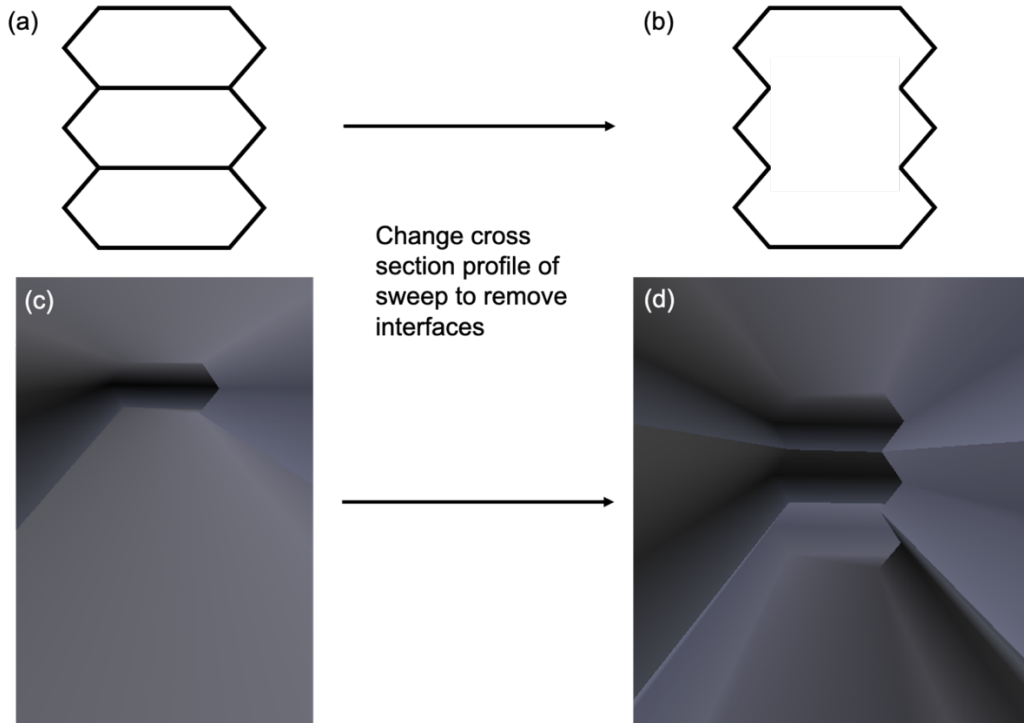


Figure 15: Cross-sectional profile changes to eliminate artificial interfaces between layers. (a) Cross section profile built-in, (b) modified cross-section profile to eliminate interfaces between layers, (c) 3D model before changes, and (d) 3D model after changes.

However, it is noted that this technique does not work for all geometries. Namely, if the layers are not aligned vertically, this methodology would create holes in the 3D model. In that case, other techniques may be used within Blender itself, including removing non-manifold geometry or creating unions between the generated STL and a larger box to remove internal faces. Regardless, the above technique suffices for the majority of cases.

A small optimization that can be performed to increase the accuracy of the generated models is to smooth the cross-sectional profile, since the actual 3D printed part will not have the sharp edges seen in the previous cross section. The interpolation of the cross-section was changed from linear polynomials to b-splines, as shown in Figure 16.

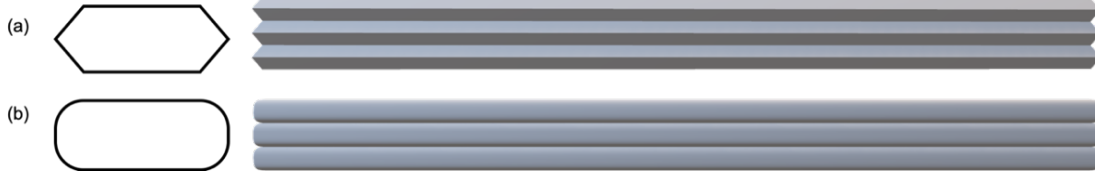


Figure 16: Optimized cross-sectional profile to mimic reality. (a) Cross-section based on linear polynomial spline between 6 points, (b) b-spline interpolation between 6 points for smoother profile.

With these settings, it is possible to generate a wide variety of STL parts that accurately portray the features of 3D printed parts, presented in Section 5.1. The major difference between 3D printed parts and bulk parts is the additional geometry created by the 3D printing paths, which this methodology preserves. While it removes the horizontal interfaces between layers, it retains the vertical interfaces between adjacent paths. The smooth curves of the paths also reflect real-world parts. Now that a robust technique of generating accurate STL files has been developed, ray tracing of these models can be conducted to predict optical performance.

4.2. Ray-Tracing Simulation

Ray tracing is an essential part of designing efficient LSCs. Instead of having to try different shapes, lumophore concentrations, surface properties, *etc.* experimentally, one can save time and resources by simulating performance computationally. Ray tracing is especially useful (compared to other modeling techniques, such as thermodynamic models) for the geometries considered in this study, which can vary widely and have intricate features. The ray tracing module used in this study is called pvTrace (Appendix Section 9.2.1.4), an open-source software for optical ray tracing of luminescent materials written in Python that is user-friendly and easily modifiable.¹⁰⁰

4.2.1. *pvTrace* background

The *pvTrace* code features a top-down architecture to isolate specific properties. It allows users to define nodes which can be designated as geometry or light. Each geometry can have material properties such as refractive index or optical properties such as scattering, absorption, or emission. Each light source has properties such as direction, divergence, and wavelength spectrum. *pvTrace* conducts ray tracing by randomly generating rays and tracking each ray through the defined geometries.¹⁰¹ Once ray tracing is complete, the optical efficiency of objects can be calculated by counting exit *vs.* incident rays. More detail about the software is available in Appendix Section 9.2.1.4.

4.2.2. *Inputs to pvTrace*

Since *pvTrace* allows the import of STL files to define LSC geometry, the software is ideal for the purposes of this work. However, several additional pieces of data are required to generate an accurate simulation of the 3D printed part. These include absorption/scattering coefficients for the waveguide, absorption/emission spectra for the lumophore, and the incident light spectrum.

While data about the absorption coefficient of waveguide materials exist in literature, the filament used in 3D printing may have different properties than pure materials. Particularly, after high-temperature processing in the extruder, the material may undergo changes in optical properties. Thus, it is best to experimentally measure the absorption coefficient of the 3D printed material, and then use this in simulation to predict performance of more complex geometries. Figure 17(a) shows a vertically printed sample with arrows indicating the incident and exit light of a UV-Vis absorption spectrometer (Appendix Section 9.2.3.5). Figure 17(b) shows the absorption coefficient for the printed waveguide polymer as a function of wavelength, which can be input into *pvTrace*.

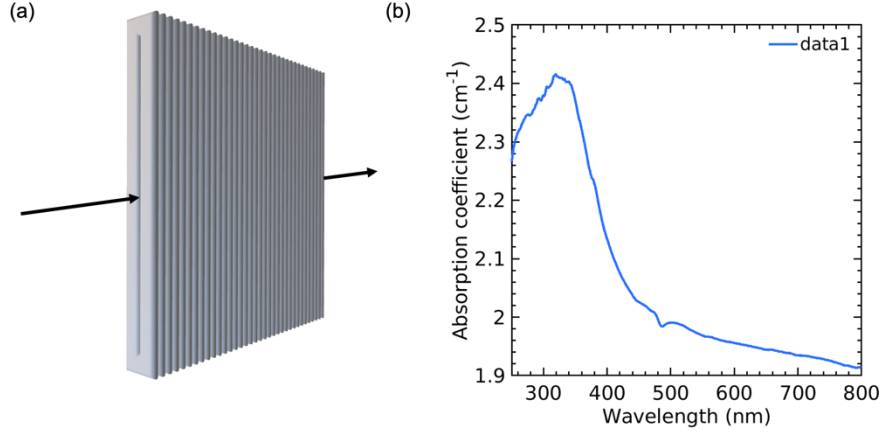


Figure 17: (a) Schematic of UV-Vis spectrometer operation with vertical 3D printed waveguide and arrow depicting entrance/exit rays, (b) absorption coefficient for an ABS waveguide calculated from UV-Vis absorbance.

While pvTrace has the capability to include scattering effects (in addition to absorption), either in the bulk material or on the surfaces of the object, these are not included in the current simulations. This is primarily due to the difficulty in experiment of isolating absorption and scattering effects, though this is an avenue of future work.

The second important inputs to pvTrace are the absorption and emission spectra of the lumophore. In this study, Lumogen F Red 305 (LR305) was exclusively used due to its suitable optical properties, high PLQY, and high thermal stability. pvTrace has built-in absorption and emission spectra for LR305, however, these are normalized to have a maximum of 1. To get the absorption coefficient in the correct units (cm⁻¹), the normalized absorption spectra must be scaled appropriately based on the concentration of the dye. It is necessary to determine an attenuation coefficient ϵ for LR305 such that:

$$\alpha = \epsilon \cdot c \quad (3)$$

where α is the absorption coefficient and c is the concentration. In literature studies where LR305 is embedded in a solid-state polymer matrix, both the dimensions (in cm) and lumophore concentration (in parts per million, ppm) are reported. It is thus possible to calculate the attenuation coefficient ϵ (in cm⁻¹ ppm⁻¹) using Equations (10) and (3):

$$\epsilon = -\frac{\ln 10^{-A}}{cL}. \quad (4)$$

Figure 18(a) shows the attenuation coefficient calculated from various literature sources,^{31,43,58,102} as well as the spectrum actually used in pvTrace. pvTrace can then calculate the absorption coefficient using the lumophore concentration input by the user. Figure 18(b) shows both the attenuation coefficient and emission spectrum used.

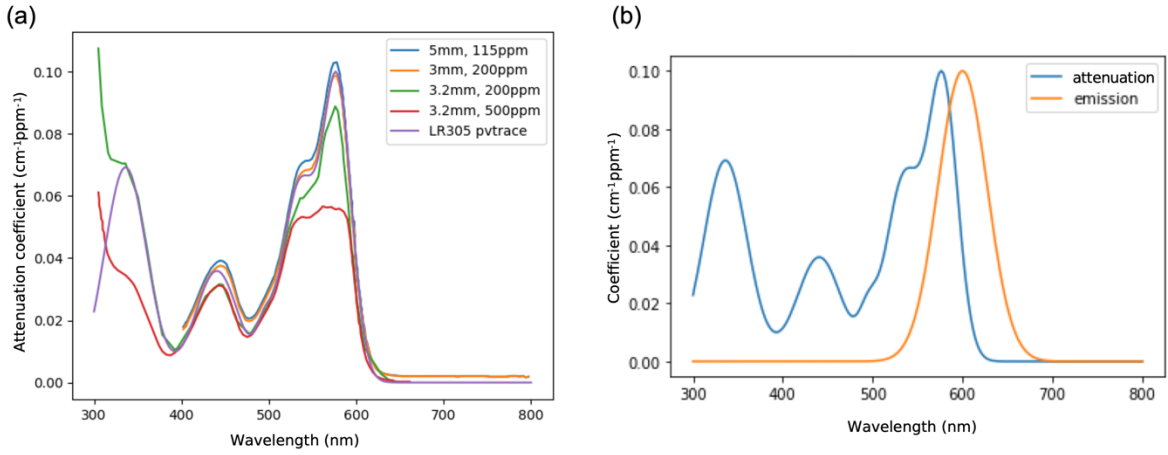


Figure 18: (a) LR305 attenuation coefficient in PMMA calculated from literature sources, as well as the spectrum used in pvTrace calculated by scaling the built-in LR305 spectrum to match. (b) attenuation coefficient and emission spectra used for LR305 in pvTrace. Note that the magnitude of the emission spectrum is arbitrary, as the spectrum is only used to determine the probability distribution of emission wavelengths.

The third important input to pvTrace is the light source spectrum. pvTrace allows any distribution of wavelengths to be the light source; however, it does not have a solar spectrum built in. This was input in three ways – first by calculating spectral radiance of a blackbody at 5800 K (the surface temperature of the sun), as shown in Equation (5):

$$B(\lambda, T) = \frac{2hc^2}{\lambda^5} \cdot \frac{1}{e^{\lambda k_B T} - 1} \quad (5)$$

where B is spectral radiance, h is the Planck constant, c is the speed of light, k_B is the Boltzmann constant, λ is wavelength, and T is temperature. The second way to get a solar spectrum is by importing the global standard spectrum (air mass 1.5 global, AM1.5G) provided by the National Renewable Energy Laboratory (NREL).¹⁰³ The final way is to

import experimentally obtained solar spectra from a solar simulator, which provides a controlled, reliable spectrum that can be used to compare across devices. These three different spectra are shown together in Figure 19, and any one of these can be used as inputs to pvTrace. For this study, the blackbody spectrum was used primarily due to its simplicity. Because the solar spectrums function solely as probability distribution functions for light wavelengths, the importance of the disparities between the different spectra is diminished, especially if only a few ($<10,000$) rays are being generated.

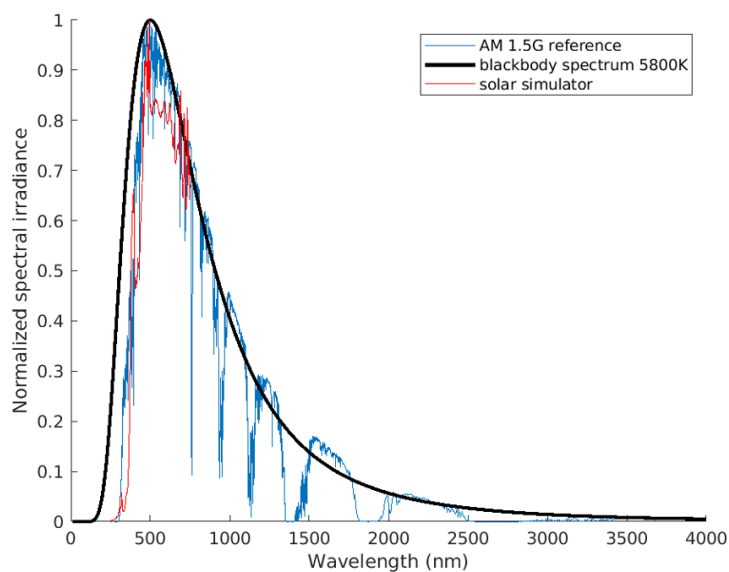


Figure 19: Three different types of solar spectra used as inputs to pvTrace. AM1.5G solar spectra provided by NREL,¹⁰³ calculated blackbody solar spectrum, or solar simulator experimental data.

4.2.3. Changes to pvTrace

While the inputs above are needed to simply model conventional LSCs, additional modifications must be made to the pvTrace code to simulate alternative geometries of interest. pvTrace has the capability of importing STLs, but the functionality in analyzing the efficiency of alternative devices is limited. For example, the current methodology of calculating optical efficiency is restricted to rectangular LSCs – the program gets the exit

position of each ray and compares the x - and y - values to the dimensions of the box. This would be much more difficult to do for circles, hexagons, or triangles. Additionally, pvTrace only has two incident light patterns available, rectangular and circular, which are not sufficient to model a wide variety of geometries. Thus, two major modifications were made to pvTrace to allow characterization of unconventional geometries: efficiency measurement using surface normals and modular masks for incident light.

Efficiency measurement using surface normals allows for greater flexibility in design. Instead of calculating the position of each exit ray, this method calculates the normal of the surface hit by the exiting ray. Then, if this normal is in the desired output direction, the ray is counted. Figure 20(a) shows an example of this being applied to a rectangular box. Rays exiting from the top will have a surface normal of $(0,0,1)$, while rays exiting from the right side will have a surface normal of $(0,1,0)$. If PV cells are placed on the right side of the LSC, it would suffice to count all rays with exit surface normal $(0,1,0)$ as output rays. Figure 20(b) shows the more complex geometry of a leaf LSC. In this case, assume flexible solar cells are placed along the edges of the leaf. Then, any exit ray with surface normal with z -value equal to 0 counts as an output ray. Instead of having to create a complex formula describing the edges of the leaf and comparing the position of exit rays to the edge, we have a much simpler formulation for counting exit rays.

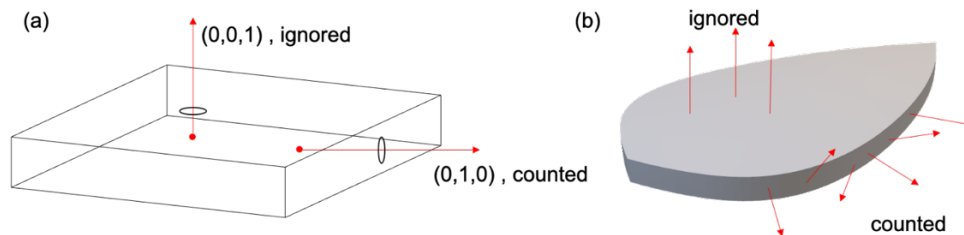


Figure 20: Efficiency measurement using surface normals. (a) Showing surface normals of exit rays at the top and right side of an LSC. (b) Showing exit rays out of the top and sides of LSC - although the direction of the side exit rays are random, the surface normals are consistent.

The second modification made to pvTrace was to fine-tune the incident light mask. pvTrace has both rectangular and circular masks built in, but these are not ideal for complicated geometries. The proposition here is to remove all rays that miss the geometry completely. A rectangular mask is used by default for the simulation, but for each ray generated as part of the mask, if it misses the part and immediately exits the simulation, it will be ignored. We can thus generate a cleaner light input only of rays that are incident on the object. Note that any interaction with the geometry is recorded, so transmission losses are still included, meaning the optical efficiency calculated by pvTrace corresponds to external optical efficiency (η_{ext}) defined in Section 2.1.2. This methodology is more similar to experimental techniques of measuring efficiency, which would likely measure light intensity at the top of the object and multiply by the area of the object. Figure 21 shows the result of this modification for a leaf LSC, plotting the x - and y - positions of entrance and exit rays.

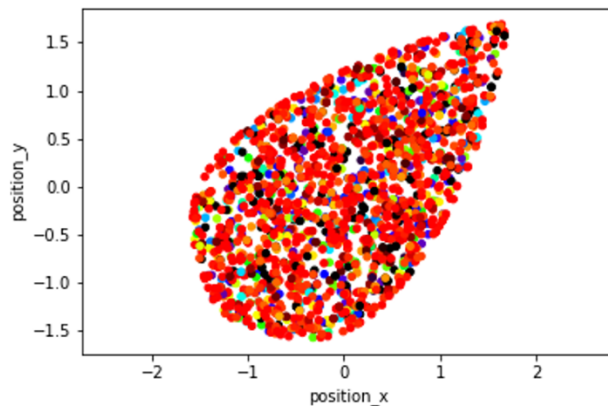


Figure 21: Results of pvTrace simulation showing success of modified mask ignoring all rays missing the object. Shows x/y position of all entrance and exit rays of a leaf LSC with LR305 lumophore.

4.2.4. Experimental Verification of pvTrace Modifications

After making these changes, it was necessary to ensure the results of pvTrace were still accurate when compared to experiment. *Ad hoc* simulations of LSCs using the two versions of pvTrace (v2.1.2, officially released,¹⁰⁴ and v2.1.sv, developed in this work¹⁰⁵)

indicated completely equivalent results, demonstrating the changes to the code did not impact analytical results at all. The next step was to compare the results of the modified pvTrace (v2.1.sv) against literature. Older versions of pvTrace (<v2.0) have been compared to experiment several times before,^{93,100,106} but experimental re-verification is useful to ensure pvTrace is still accurate given changes to the code.

Several studies from the last few years were chosen, with the criteria that the LSCs are bulk (not thin-film), use LR305 embedded in a PMMA matrix, and did not have any back-reflectors. The important parameters from each study were: LSC dimensions, LR305 concentration, refractive index, waveguide parasitic absorption, light source spectrum, and edge emission measurement methodology.

The comparisons indicate pvTrace v2.1.sv retains its accuracy against a wide variety of experimentally produced LSCs. The predicted efficiency is within 1% for most geometries and within 5% for all geometries. The difficulties in simulation that reduce the accuracy include unreported background absorption coefficients, differences in PLQY as a function of concentration, or varying edge emission measurement techniques.

The full results from this comparison are presented in Appendix Section 9.2.1.4.2.

4.2.5. pvTrace Graphical User Interface (GUI)

Now that we understand the inputs to pvTrace and have made the necessary modifications to allow simulation and analysis of unconventional LSC designs, we can optimize the computational process. The first optimization was to create a graphical user interface. Experimental chemistry and materials science groups working on LSCs may not have extensive experience with programming. This GUI helps make pvTrace more accessible for these labs and optimizes the workflow for all users as it makes it easier to save and load input and result files.

Figure 22 shows a screenshot of the GUI developed in this work¹⁰⁷ and the various inputs required for the simulation. The simulation will return the overall optical efficiency as well as the optical efficiency at each edge of the device (of course, for alternative geometries, the efficiencies at the 4 cardinal directions have little meaning). The program will also output five plots as visual aids of optical performance. The full details of the input parameters and output plots are available in Appendix Section 9.2.1.4.3.

4.2.6. pvTrace parallelization

A final optimization made to the pvTrace code was including parallelization. The ray-tracing problem is considered “embarrassingly” parallel, since each ray is independent and does not interact with other rays. For this reason, the simulation can be split across multiple computing cores to speed up computational time. This is especially useful with access to a supercomputer with dozens of cores. For example, if a user wanted to simulate 10,000 rays, a supercomputer with 10 cores could assign 1,000 rays to each core, vastly improving computation time. This optimization is especially useful for STL files – since they have so many tiny surfaces, each ray can take a while to simulate.

pvTrace v2.1.sv uses either the multiprocessing module or the Ray module,^{108,109} depending on whether pvTrace is running on a personal machine or a supercomputer, to parallelize its processes. The parallelization results in a massive reduction in runtime of pvTrace. It takes approximately the same amount of time to run 1,000 rays on a personal computer using the original pvTrace script as it does to run 100,000 rays on a computing cluster using parallelized pvTrace. This new script thus increases the quality of simulations while reducing the time required to complete one experimental cycle (as shown in Figure 11). The full methodology and results of implementing parallelization in pvTrace are detailed in Appendix Section 9.2.1.4.4.

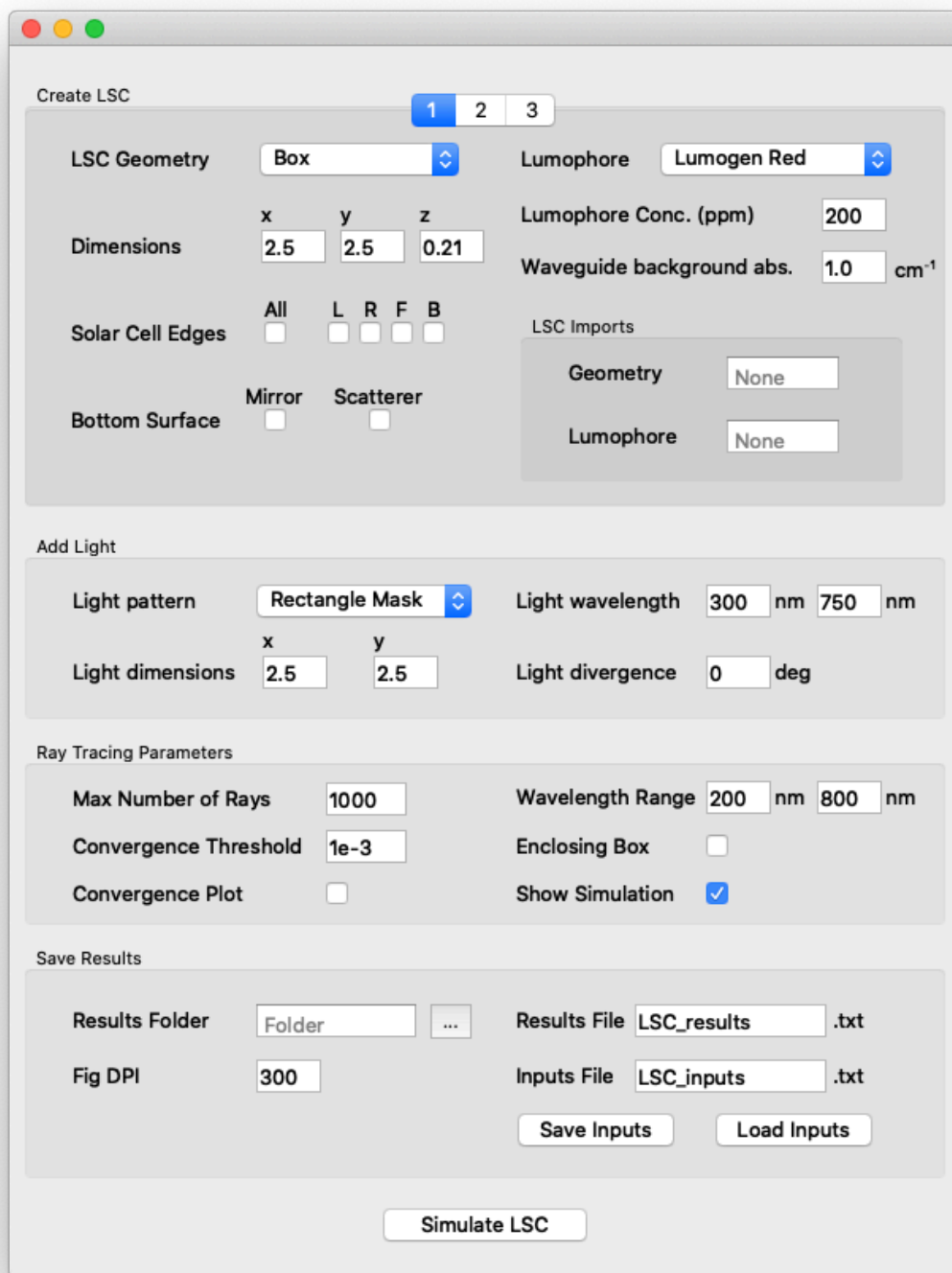


Figure 22: pvTrace GUI showing all capabilities. Basic steps include creating an LSC, adding light, setting ray tracing parameters, and saving results. Clicking "Simulate LSC" using simply the default values will create a Box LSC with 2.5 x 2.5 x 0.2 cm dimensions, 200 ppm LR305 in PMMA (1.0 cm⁻¹ background absorption), with a solar spectrum of light incident on top.

4.2.7. Ray tracing of 3D printed parts

pvTrace simulations were conducted to compare the optical efficiency of bulk *vs.* 3D printed parts. The shapes of these parts were varied based on available literature in the field and are shown in Figure 28 and Figure 29. Conventional rectangular LSCs were first used, with various configurations used for printing. Hollow and solid cylindrical array LSCs were also used, based on Inman *et al.*⁴⁹ Next, polygonal LSCs (triangle, hexagon) and a circle with a flat edge were used, based on Kennedy *et al.*⁵⁵ An LSC based on the Leaf Roof proposed by Reinders *et al.* was also used.⁵⁷ Finally, original designs were used, including another leaf-like LSC and a vertically oriented cylindrical array.

Both bulk and 3D printed versions of all of the above parts were created for comparison. For pvTrace simulations, 10,000 rays were used for STL files (due to the increase in computation time created by the large number of surfaces) and 100,000 rays were used for bulk LSCs. 64 cores were used for both cases.

The simulated results of the 3D printed parts were compared to the experimentally measured optical efficiency of the 3D printed parts to determine the accuracy of the simulations. The first step to 3D printing these LSCs is preparing luminescent filament.

4.3. Luminescent Filament Preparation

The process of preparing luminescent filament occurs in three primary steps. First, the lumophore must be incorporated into the polymer host material. Second, the incorporated bulk material must be powdered so it can be processed. Finally, the powder is fed through an extruder which melts the individual particles into a solid cylindrical filament. Figure 23 shows a schematic of this overall process.

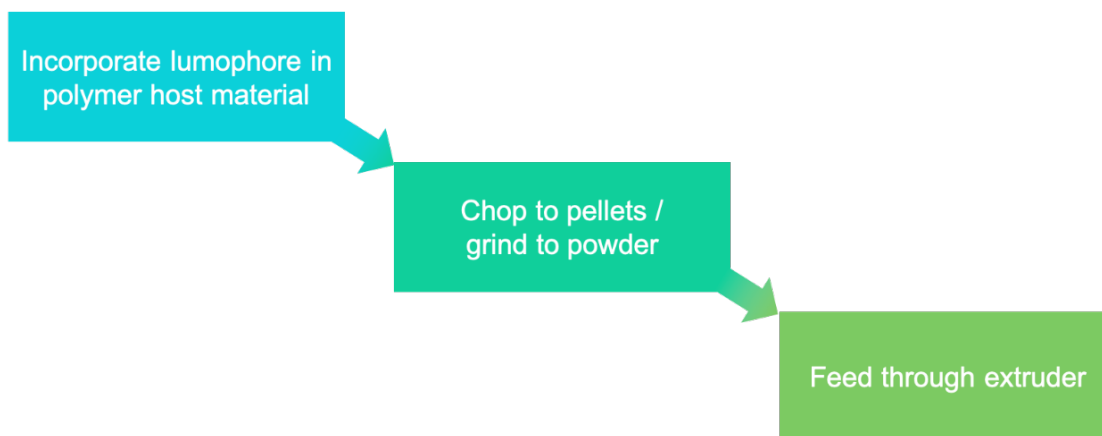


Figure 23: Schematic showing the process of luminescent filament preparation. Lumophores must first be incorporated into the polymer host material, then the bulk material must be powdered, and finally must be fed through an extruder to generate filament.

4.3.1. Lumophore Incorporation

Three different avenues of lumophore incorporation were considered, of increasing complexity. First was simply physically mixing the two components, as shown in Figure 24(a). Since both LR305 and PMMA are sold in powder form, this methodology is straightforward. The second method is solvent casting, as shown in Figure 24(b). In this method, both lumophore and polymer are dissolved in a mutually compatible solvent which is evaporated over a period of time, leaving a bulk material. The final method is lumophore grafting, as shown in Figure 24(c). Here, a methacrylate group is grafted to the head and tail of a LR305 molecule. Then, polymerization of methyl methacrylate (MMA) with functionalized LR305 can occur, resulting in LR305 evenly distributed within a PMMA matrix. Time constraints meant that the actual synthesis of functionalized LR305 was outside the scope of this work; however, the synthetic procedure for how LR305 might be functionalized in the future is available in Appendix Section 9.2.2.3. As physical mixing and solvent casting both generated comparable preliminary results, the decision was made to use the physical mixing method due to its inherent simplicity. Further information about solvent casting is available in Appendix Section 9.2.2.2.

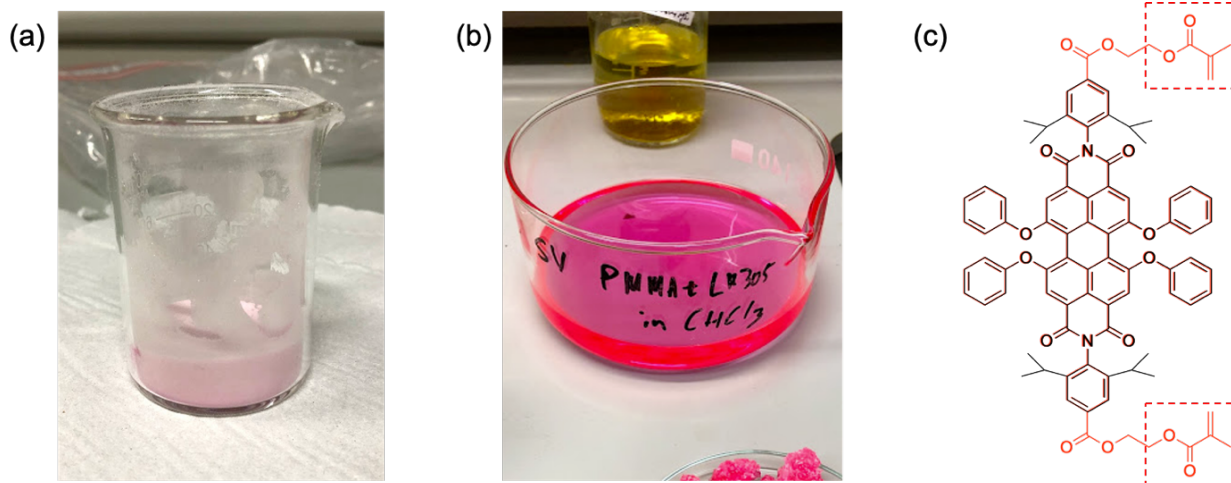


Figure 24: Representations of the three lumophore incorporation techniques investigated. (a) Physical mixing of lumophore and polymer powders. (b) Solvent casting of lumophore and polymer dissolved in mutually compatible solvent. (c) Lumophore functionalization, grafting of monomer group (highlighted in red) on head/tail of lumophore (shown in black) for later polymerization.

4.3.1.1. Physical Mixing

PMMA powder and LR305 at the concentration desired (typically 0.01 wt%) were measured out and added to a beaker. The two powders were then mixed, ensuring the clumps of LR305 were broken up until the entire PMMA powder had a pinkish hue, as shown in Figure 24(a). This ensured relatively even distribution of lumophore in the polymer host, as seen qualitatively, but the distribution could be improved through other incorporation methods. Full experimental details of the procedure can be found in the Appendix, Section 9.2.2.1. Other physical mixing methods, such as using a mixing machine, could be investigated in future work.

4.3.2. Filament Extrusion

The physical mixing method was used to generate luminescent powder for all of the filament extruded in this study. The filament was extruded using a screw extruder to melt the luminescent powder and force the material through a die that determines the

diameter of the filament. The full procedure for filament extrusion is detailed in Appendix Section 9.2.3.2. The extruder used in this study was the commercially-available Noztek Pro Filament Extruder,¹¹⁰ shown in Figure 25, chosen for its accessibility. Once several meters of luminescent filament are produced, they can be used for 3D printing. For reference, ~ 0.5 m of filament is typically enough to print a $2.5 \times 2.5 \times 0.21$ cm part.



Figure 25: Photograph of Noztek Pro Filament Extruder used in this study. Shows the motor, heater, hopper, and dials used to control the extruder. Test, non-luminescent ABS filament is being produced in this picture.

4.4. 3D Printing Parts

To emphasize universal accessibility to 3D printing of LSCs, a cheap, commercially available printer with open-source documentation was chosen: the Prusa MK3S i3,¹¹¹ shown in Figure 26 (and Appendix Section 9.2.3.3). As Ultimaker Cura was used as the slicing software, it was a natural choice for the 3D printing software as well.

Several printing parameters had to be altered in order to print optically transparent parts. Primarily, the infill had to be increased to 100% to ensure the printed part had limited air gaps that could impact light transport pathways and reduce efficiency. Because the infill was so high, there was no need for walls around the part, so this option was also deselected. The temperature had to be fine-tuned for PMMA, which is not as commonly

printed as ABS or PLA. The fan was also not used, as the high temperature of the printed filament allowed better bonding with already deposited layers, reducing optical interfaces.

Line width and layer height were also optimized to maximize transparency. Theoretically, a larger line width would reduce the number of optical interfaces between a re-emitted wave and the edge of the part. A higher layer height would make each printed path have a more suitable cross-section profile for optical transparency. These two parameters thus had to be fine-tuned. Cura also has a variety of infill patterns available, including zigzag, concentric, *etc.*, and these settings were also investigated to determine an optimal configuration. The final optimized conditions are described in Section 5.4.



Figure 26: Photograph of Prusa MK3S printer when first assembled. This is a highly accessible, commercially available printer with modification capabilities.

4.5. Optical Characterization

Finally, once an LSC was successfully 3D printed, it was characterized to determine its optical performance. This was done in two steps: basic optical characterization and optical efficiency measurement. Note that optical efficiency corresponds to external photon efficiency (η_{ext}) as defined in Section 2.1.2, unless noted otherwise.

4.5.1. Basic Optical Characterization

First, the absorption spectrum of commercial filament was compared against that of in-house extruded filament. Then, the absorption spectra of various printed parts from commercial filament were compared against each other to determine which printing conditions best optimize transparency. These results are presented in Section 5.4.1.

The absorption of printed samples of PMMA doped with LR305 was also measured to get a sense of the impact of extrusion and 3D printing on the absorption profile of LR305 in solid state. These results are presented in Section 5.4.2.

Finally, the absorption of bulk parts of PMMA doped with LR305 was also measured as a control reference in Section 5.4.3. Recall that bulk parts are not 3D printed LSCs, but rather LSCs fabricated with conventional manufacturing techniques, and therefore provide a useful baseline comparison for performance evaluation.

All absorption spectra were obtained using a UV-Vis absorption spectrometer, described in Appendix Section 9.2.3.5.

4.5.2. Optical Efficiency Measurement

The optical efficiency was measured using a solar simulator and integrating sphere coupled to a spectrometer, as shown in Figure 27(a) and discussed in Appendix Section 9.2.3.6/9.2.3.8. A sample holder for the printed LSCs was itself 3D printed from gray PLA and is shown in Figure 27(b). A black card and tape were placed below and to the right of the LSC to prevent any back- and side-scattering events.

The LSC was placed on top of the sample holder, and a solar simulator was placed above the LSC. The distance of the solar simulator above the sample was calibrated such that 1 sun ($1000 \pm 10 \text{ W/m}^2$) of light intensity shined on the top of the LSC. One edge of the LSC faced the integrating sphere.

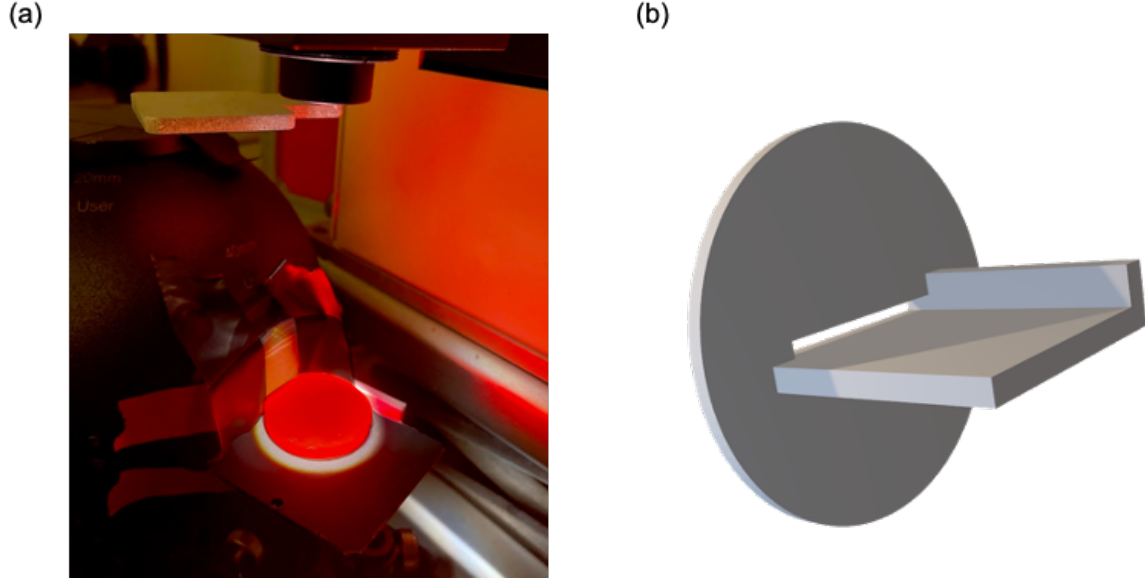


Figure 27: Optical efficiency characterization of 3D printed LSCs. (a) Shows a picture of the setup with a solar simulator shining on the top of a cut circular LSC, and the edge emitting into an integrating sphere spectrometer. (b) Shows a CAD model of the sample holder printed for the purpose of holding the LSC, serving as a mask for emitted light, and blocking out environmental light to limit noise and interference with results.

It was thus possible to measure the edge emission of each edge, sum these values, and divide by the incident light power to calculate the optical efficiency. Specifically, the external photon efficiency was calculated by:

$$\eta_{ext} = \frac{\sum_k \left[\int_{\lambda_1}^{\lambda_2} I_{s_k} d\lambda \cdot A_{s_k} \right]}{\int_{\lambda_1}^{\lambda_2} I_F d\lambda \cdot A_F} \quad (6)$$

where s_k is the k^{th} edge of the LSC, I_{s_k} is the light intensity (W/m²/nm) emitted from that edge, A_{s_k} is the area of that edge, I_F is the light intensity on the top surface of the LSC, A_F is the area of the top surface of the LSC, and λ_1 and λ_2 are the lower and upper bounds of the wavelength region, respectively. Internal photon efficiency can be calculated by convoluting the input light spectrum by the absorption of the lumophore (α_{LR}):

$$\eta_{int} = \frac{\sum_k \left[\int_{\lambda_1}^{\lambda_2} I_{s_k} d\lambda \cdot A_{s_k} \right]}{\int_{\lambda_1}^{\lambda_2} I_F \alpha_{LR} d\lambda \cdot A_F} \quad (7)$$

Note that this setup only works for LSCs with at least one flat edge. An alternative setup must be used to measure edge emission of unconventional geometry, perhaps using flexible polymer solar cells attached to the LSC with refractive index-matching adhesive, but this is a topic for future work.

Now that the methodology for designing, simulating, printing, and characterizing LSCs has been defined, it is possible to conduct a full evaluation of performance. The following section will discuss the results of the work conducted in this study.

5. Results and Discussion

5.1. STL Generation

Figure 28 shows examples of STL files of bulk parts, while Figure 29 shows STL files of the same parts but 3D printed. Note again that bulk parts are defined as LSCs that can be manufactured with conventional methods. The STL files of 3D printed parts were generated with the methodology presented in Section 4.1.

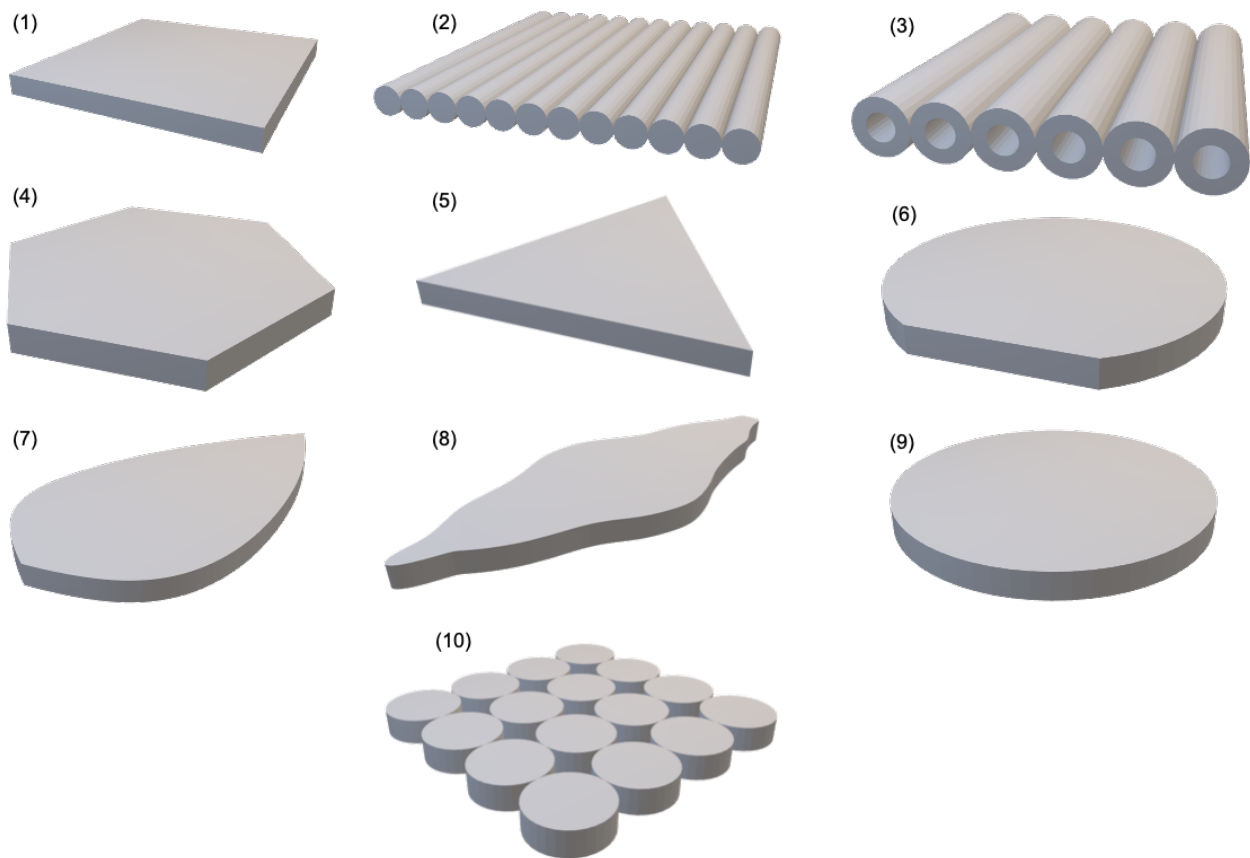


Figure 28: 3D CAD models of bulk parts considered for simulated efficiency analysis in this study. Note that bulk parts are manufactured with conventional methods (mold polymerization or subtractive manufacturing) and do not contain 3D printing interfaces. (1) Rectangular, (2) cylindrical array, (3) hollow cylindrical array, (4) hexagonal, (5) triangular, (6) circular cut, (7) leaf, (8) leaf roof, (9) circular, and (10) vertically oriented cylindrical array.

Most of the 3D printed shapes (11, 12, 14-22) were generated using a cyclic methodology, since this version was more suitable to their geometry. Shape (13) was generated using a non-cyclic methodology, allowing a comparison of optical efficiency (both in simulation and experiment) between the two generation techniques.

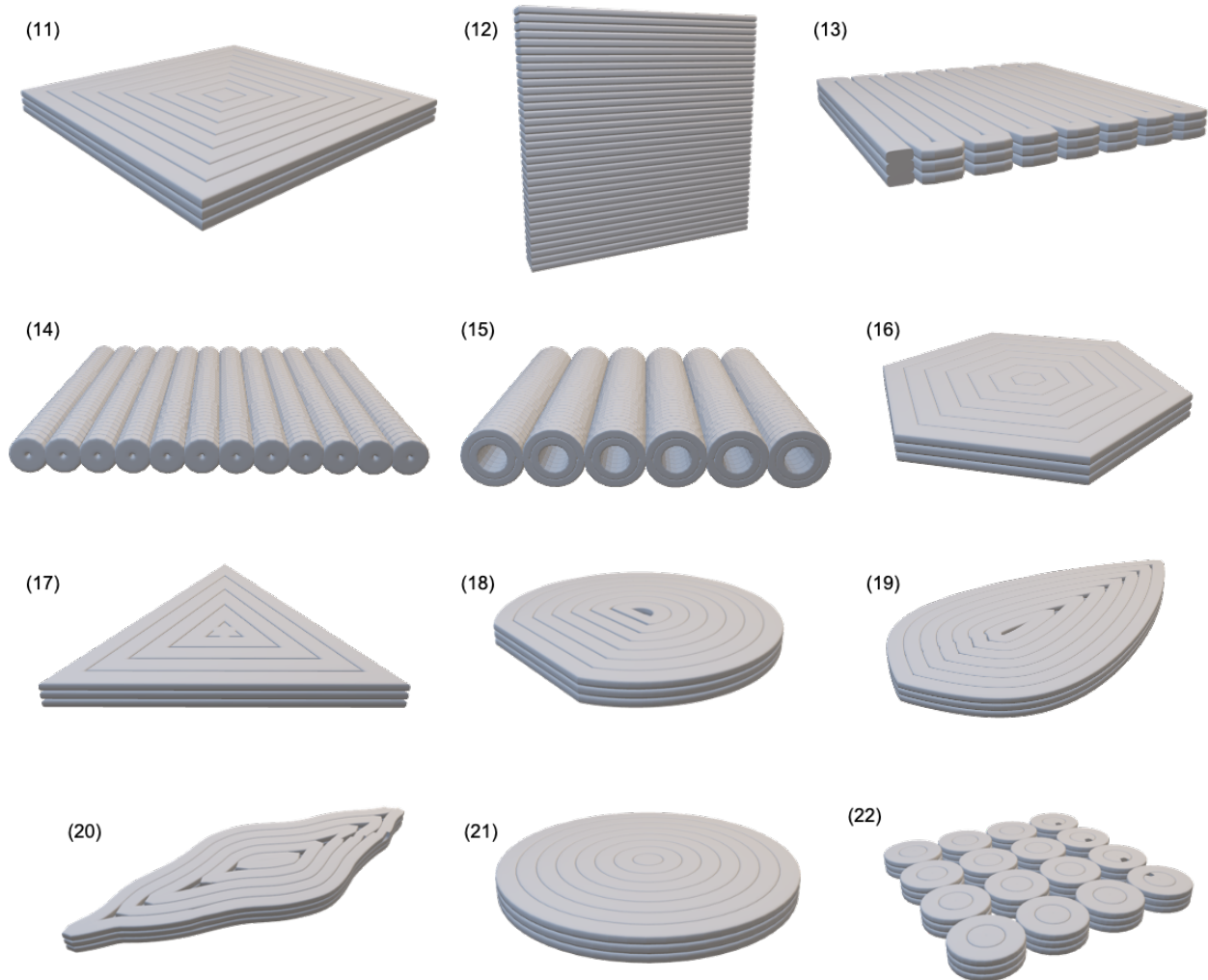


Figure 29: 3D CAD models of 3D printed LSCs. Numbering continued from Figure 28 for clarity in reporting results. (11) concentric printed rectangle, (12) vertically printed rectangle, (13) zigzag printed rectangle, (14) vertically printed cylindrical array, (15) vertically printed hollow cylindrical array, (16) concentric printed hexagon, (17) concentric printed triangle, (18) concentric printed cut circle, (19) concentric printed leaf, (20) concentric printed leaf roof, (21) concentric printed circle, (22) concentric printed vertically oriented cylinder array.

As seen, the cyclic technique works well for generating CAD files for a wide variety of geometries. All of the generated parts have the intricacies and details of the 3D printed path included.

Some shapes, notably (18), (19), (20), and (22), have holes created where LSCs fabricated using conventional manufacturing techniques would not. This is not a result of the STL generation process but rather a feature of the 3D printed part itself. The line width set by the 3D printer to enhance optical transparency of the part results in sharper curves not being filled in properly. Note the broader curves in (11), (16), (17), and (21) do not create these holes.

5.2. Ray Trace Analysis

5.2.1. Bulk vs. 3D Printed LSCs

The optical efficiency of 3D printed LSCs will be compared against bulk LSCs in this section. The first methodology of comparison uses the *surface normal method*. This method counts all rays exiting all of the edges of the LSC as collected rays. The results are shown in Table 2, which reports the simulated η_{ext} for various device geometries.

As seen, the simulated efficiency does not change much between bulk parts. The non-cylindrical parts have similar to slightly higher efficiency than the rectangular LSC, which is expected from the studies reported in Section 2.1.3.2. The cylindrical parts have higher efficiencies, around 15-20%, which is also supported by experimental and simulated results as presented in Section 2.1.3.2. While the parts were all standardized to have the same frontal area, the variation in efficiency could be due to different gains between parts.

Most concentric printed devices have enhanced efficiency as compared to bulk devices. For parts featuring an increase in efficiency, there is an average of $4.97 \pm 2.37\%$

efficiency increase, for which there are several potential explanations. One possibility is that the curved surfaces resulting from the printed path reduce escape cone losses. Zewail *et al.* reported an increase in edge emission for concave LSCs.¹¹² Another potential explanation is the 3D printing paths function similarly to fiber optic cables and help guide light to the edges of the device. A result of these two effects would be increased efficiency due to improved directionality of light, as photons are guided more effectively towards the edges and are emitted more orthogonally than in bulk parts.

One part that saw a *reduction* in efficiency after concentric 3D printing was the vertical cylinder array (10/22). This could be due to greater reabsorption events in 3D printed parts – applying the directionality argument here implies re-emitted rays are more likely to be emitted perpendicular to the edges, thus being more likely to enter another cylinder and be reabsorbed by the lumophore or parasitically absorbed by the waveguide.

The box was the only geometry where non-concentric (i.e. vertical (12), zigzag (13)) printing methods were explored. For the zigzag pattern, the increase in efficiency was approximately the same as the concentric pattern. However, the vertically printed box had significantly lower efficiency to the bulk part. Other vertically printed parts (14, 15) also saw a reduction in efficiency after 3D printing. This can be explained by directionality effects, as vertically printed parts (as shown in Figure 29) would direct more light towards the top and bottom surfaces rather than to the edges. Another explanation would be the lack of side-oriented edges in vertically printed parts, due to the curvatures introduced by the 3D printing process, meaning there are only a few edge faces that would satisfy the criteria of being counted with the *surface normal* method.

Table 2: Simulated efficiency of bulk vs. 3D printed parts using pvTrace. First column enumerates the geometries based on their numbering in Figure 28 and Figure 29, second column shows the general geometry of the devices, third column shows the method of fabrication (for printed parts shows the pattern used), and the last column shows the external optical efficiency (η_{ext}) in percent.

Num.	LSC Shape	Printing Method	η_{ext} (%) (surface normal)
(1)	Box	Bulk	10.68
(11)	Box	Concentric	18.76
(12)	Box	Vertical	2.93
(13)	Box	Zigzag	19.99
(2)	Cylinder Array	Bulk	18.17
(14)	Cylinder Array	Concentric	4.68
(3)	Cylinder Array	Hollow, bulk	20.69
(15)	Cylinder Array	Hollow, concentric	4.91
(4)	Hexagon	Bulk	11.72
(16)	Hexagon	Concentric	13.93
(5)	Triangle	Bulk	15.22
(17)	Triangle	Concentric	19.48
(6)	Circle (cut)	Bulk	10.61
(18)	Circle (cut)	Concentric	15.67
(7)	Leaf	Bulk	10.42
(19)	Leaf	Concentric	13.98
(8)	Leaf Roof	Bulk	14.98
(20)	Leaf Roof	Concentric	23.29
(9)	Circle	Bulk	10.42
(21)	Circle	Concentric	13.76
(10)	Cylinder Array	Vertical, bulk	21.19
(22)	Cylinder Array	Vertical, concentric	15.77

While the *surface normal* efficiency analysis method is useful, there are clearly limitations. Additionally, from an experimental standpoint, the preferred method for evaluating LSC optical efficiency experimentally is with a solar simulator and spectrometer attached to an integrating sphere. The use of an integrating sphere requires one edge of the printed device to be directed towards an input port. To mimic this in simulation, instead of counting all rays exiting from the edges of the device, the device is first enclosed in a box, and all rays exiting from the edges of the enclosing box are counted. An example of this for the 3D printed circle STL is shown in Figure 30. The results from this analysis are shown in Table 3, which compares bulk efficiency to printed efficiency using the *enclosing box efficiency analysis method*.

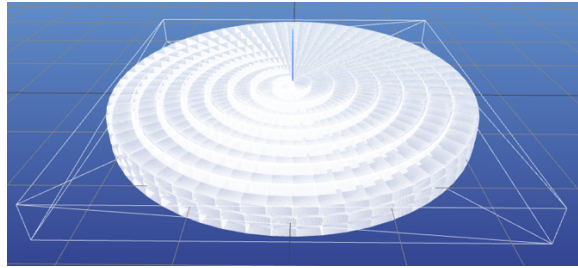


Figure 30: Example of enclosing box created around STLs. This allows better comparison of simulation to experiment, as integrating spheres often require a flat edge as input.

For device geometries (1)-(3) and (11)/(13), the results are essentially equivalent to the surface normal method. This is because these geometries are essentially rectangular, so adding an enclosing box around them should not change their efficiency. For devices (4)-(10) and (16)-(22), there is a reduction in efficiency between the two measurement techniques. This is likely due to the increased distance the exit rays have to travel from the edge of the device to the edge of the enclosing box. Some rays may be angled such that they exit the top or bottom of the box. However, for devices (4)-(6) and (16)-(18), since each has a flat edge, in experiment it would be possible to align the flat edge of the device with the input to the integrating sphere and essentially replicate the *surface normal* technique, providing 2 different ways to validate simulation.

Table 3: Optical efficiency results using the enclosing box method for simulated performance analysis of different LSC designs. Results from the surface normal method are largely confirmed. Numbering corresponds to parts as shown in Figure 28 and Figure 29. Last column shows absolute change from surface normal method (i.e. if surface normal predicted 11% and enclosing box predicted 10%, the column would show -1).

Num.	LSC Shape	Printing Method	η_{ext} (%) (enclosing box)	change from surface normal
(1)	Box	Bulk	10.49	-0.19
(11)	Box	Concentric	19.28	+0.52
(12)	Box	Vertical	9.63	+6.70
(13)	Box	Zigzag	20.36	+0.37
(2)	Cylinder Array	Bulk	18.52	+0.35
(14)	Cylinder Array	Concentric	15.05	+10.37
(3)	Cylinder Array	Hollow, bulk	18.99	-1.70
(15)	Cylinder Array	Hollow, concentric	14.06	+9.14
(4)	Hexagonal	Bulk	7.47	-4.25
(16)	Hexagonal	Concentric	11.76	-2.17
(5)	Triangle	Bulk	6.65	-8.57
(17)	Triangle	Concentric	11.47	-8.01
(6)	Circle (cut)	Bulk	7.98	-2.63
(18)	Circle (cut)	Concentric	11.52	-4.15
(7)	Leaf	Bulk	5.03	-5.39
(19)	Leaf	Concentric	10.11	-3.87
(8)	Leaf Roof	Bulk	5.71	-9.27
(20)	Leaf Roof	Concentric	15.69	-7.60
(9)	Circle	Bulk	6.74	-3.68
(21)	Circle	Concentric	12.28	-1.48
(10)	Cylinder Array	Vertical, bulk	16.53	-4.66
(22)	Cylinder Array	Vertical, concentric	12.20	-3.57

The trend of increased efficiency for concentric 3D printed parts is upheld, with an average increase of $6.01 \pm 2.42\%$ efficiency. For the box device featuring different printing patterns (11-13), the zigzag pattern (13) again performs similarly to the concentric pattern (11). We see the problems with vertical printing again, with devices (12), (14), and (15) showing reduced efficiency compared to their bulk versions (1), (2), and (3) respectively. However, the *enclosing box* efficiency for these vertically printed devices is much higher than the *surface normal* efficiency, due to larger number of rays being counted. With the *surface normal* method, fewer rays were counted as fewer edge faces had surface normals matching the criteria, but the *enclosing box* method counts all rays hitting the edge of the enclosing box, regardless of which surface they exit from, thus increasing the number of rays counted.

We again see the vertical cylinder array as the only geometry where efficiency decreases after concentric 3D printing, this time by 4.33%, potentially due to the same reason as before of directional re-emission and reabsorption by adjacent cylinders.

The results above are promising, with simulation consistently showing an increase in optical efficiency for 3D printed LSCs compared to their bulk counterparts for both simulation methods. Based on these results, it makes sense to proceed to the next step of this study, generating luminescent filament for 3D printing.

5.3. Luminescent Filament Generation

Before generating luminescent filament, plain PMMA filament was extruded to test the extrusion process and evaluate its impact on the optical transparency of PMMA.

Filaments were processed at 180°C. Although a 1.75 mm die was used in the extruder, 2.0 mm filament was initially produced. Since the 3D printer nozzle has low tolerance for error in filament diameter (it must be less than 1.85 mm¹¹³), the filament

was pulled with gentle force using tweezers as it exited the extruder, stretching the filament to the desired filament diameter. This optimized technique produced filament with diameter ranging from 1.4 mm to 1.8 mm, which is more compatible with the 3D printer (shown in Figure 31). To reduce this wide variation, in the future a purpose-built filament pulling machine could provide a pulling force dependent on measured diameter.

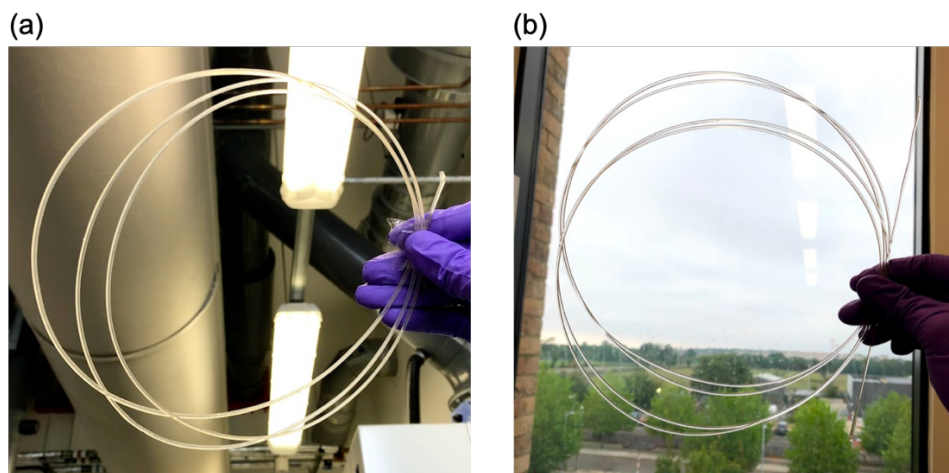


Figure 31: Pictures of plain PMMA filament produced from extruder using optimized filament pulling technique. (a) showing background of indoor lighting and (b) natural sunlight to show transparency of filament.

UV/Vis absorption spectroscopy was used to quantify the transparency of the extruded PMMA. Figure 32 shows the absorption coefficient for single strands of commercially available PMMA filament versus experimentally extruded PMMA filament, for comparison. Clearly, the extruded filament has a higher absorption coefficient and thus lower transparency. There are several reasons to explain this difference – impurities in the extruder, air bubbles caused in temperature variations in the heating band, lack of control over extrusion speed, and incompatibility of the extruder used with powdered PMMA. This low transparency will be taken into account when evaluating the performance of parts printed from this filament.

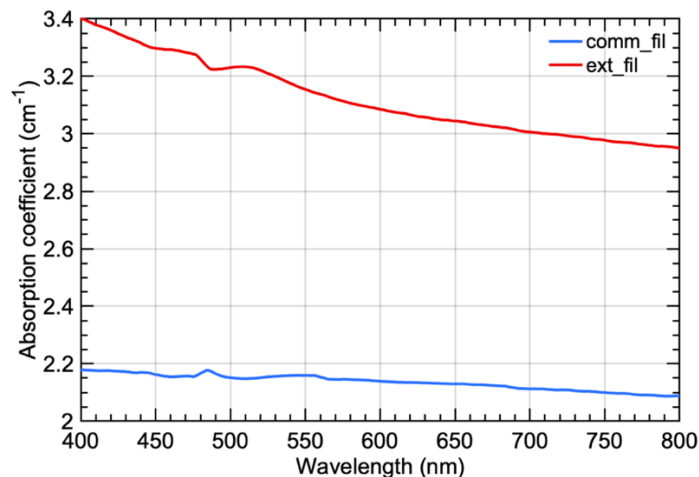


Figure 32: Transparency of commercial (*comm_fil*) vs. extruder (*ext_fil*) filament, showing the better optical transparency that can be achieved with commercial production.

After optimizing pure PMMA extrusion, PMMA doped with LR305 using the physical mixing method was extruded. To accommodate the increased viscosity of the filament due to dispersed LR305 particles, the PMMA with LR305 mixture was run at 190°C instead of 180°C. The same pulling mechanism was used as before to generate filament shown in Figure 33. The diameter of the filament ranged from 1.2 mm to 1.8 mm.

Following production of luminescent filament, 3D printing of parts could occur, as discussed in the following section.

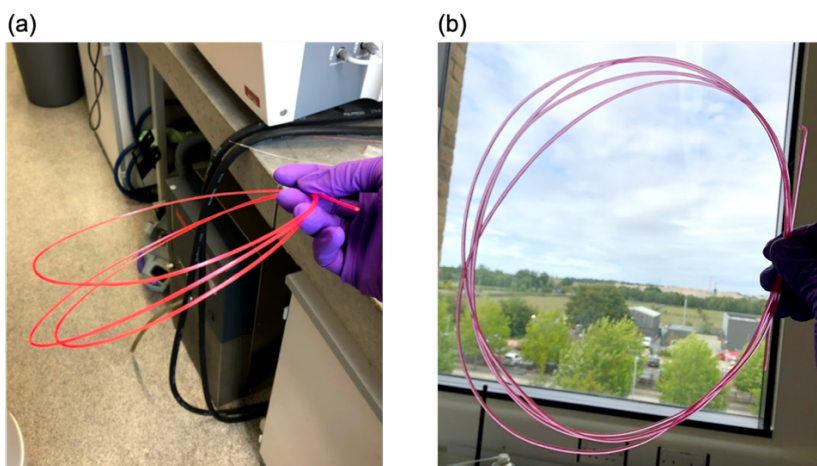


Figure 33: Pictures of extruded PMMA+LR305 filament after optimizing the extrusion process. 0.01 wt% LR305 was again used. (a) note the luminescent characteristics of the filament under indoor lighting by the window, (b) note the optical transparency of the filament held up to natural outdoor lighting.

5.4. 3D Printing

5.4.1. *Plain PMMA Parts*

The printing parameters were first optimized using commercially available plain PMMA filament. The key parameters were temperature, speed, line width/layer height, and printing pattern.

Temperature and printing speed were first set to maintain consistency across parts. High temperatures improve flow rate but can also create bubbles within the part. Lower temperatures improve optical properties but can cause barrel jams if the filament does not soften sufficiently. For commercial PMMA filament, a temperature of 230 °C and print speed of 40 mm/s was used.

The next parameters to be optimized were line width and layer height. Line width is defined as the width of the path deposited by the extruder nozzle, while layer height is the thickness of the deposited path. The ratio between these parameters is critical for optical transparency. If the ratio is too close to 1, the paths become cylindrical, limiting the number of straight paths from the center of the printed part to its edges. To investigate this effect experimentally, a variety of line width/layer height ratios were printed. For this comparison, two printing methods were used. First, parts were printed with the zigzag technique, with layer height of 0.4 mm and line width varying from 1.6 mm to 0.4 mm. Then, the part was printed vertically, also using a layer height of 0.4 mm and line widths from 0.4 mm to 1.6 mm. When combined, these layouts resulted in parts with width/height ratios ranging from 0.25 to 4.00, shown in Figure 34. Additional parts of layer heights 0.15 and 0.7 mm were also printed for further comparison, and similar results were obtained.

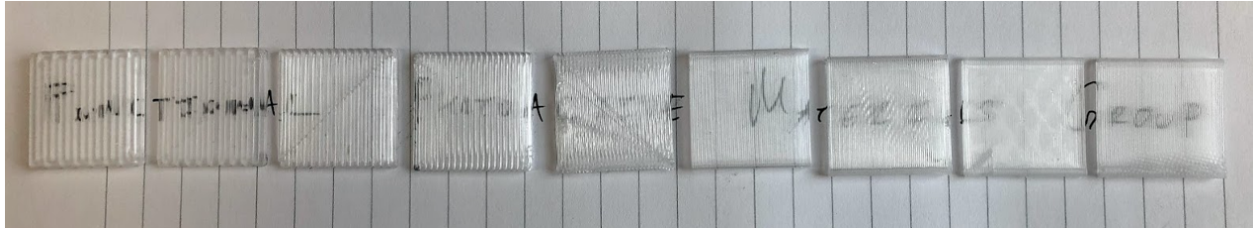


Figure 34: Pictures of various 3D printed parts from plain, commercially available PMMA filament. Showing the progression of layer height/line width ratios from 0.5 (leftmost) to 4 (rightmost)

UV/Vis absorption spectroscopy was used to evaluate the absorption coefficient, and thus transparency, of the printed parts, shown in Figure 35. As expected, there is a maximum when the ratio is 1, and a reduction in absorption is seen as the ratio tends away from 1. The absorption coefficient also generally matches regardless of layer height, suggesting the importance of the ratio of height/width over either individual parameter in predicting the optical transparency of the part.

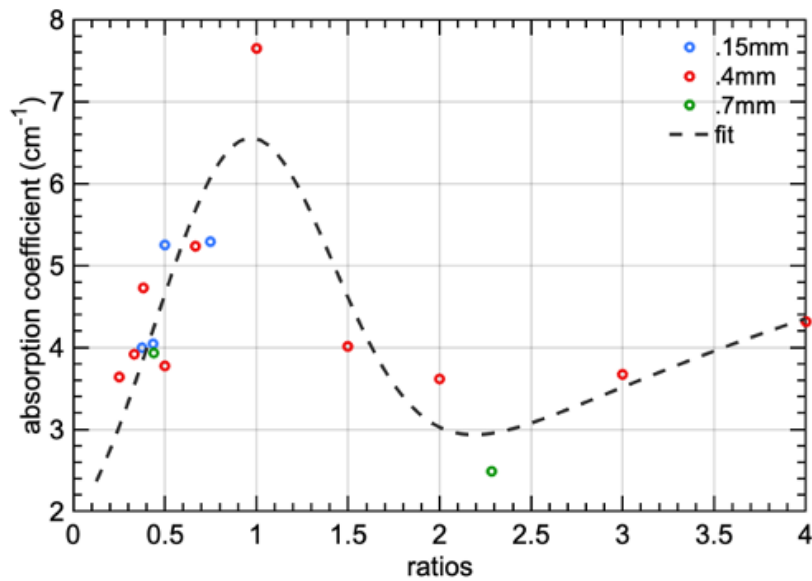


Figure 35: Absorption coefficient for printed samples from commercially available plain PMMA filament. Shows a maximum of absorption when the ratio equals 1, with a local minimum around 2. Blue circles show the measured absorption coefficient for 0.15 mm layer height printed samples, red circles for 0.4mm layer, and green circles for 0.7 mm layer height. The dashed line shows the fit generated using a double Gaussian fit and is used simply to show phenomenological trends. All data points generally match the fit curve regardless of layer height used.

To validate these experimental observations, the same parts were also simulated in pvTrace using a broadband light spectrum of 400 to 800 nm to mimic the UV/Vis spectrometer. The absorption coefficient was calculated by dividing the number of rays exiting the bottom of the part by the number of incident rays, as shown in Figure 36. The general characteristics of the experimental curve can be seen in simulation as well. There is a peak in absorption around a ratio of 1.5, a local minimum around 2, and reduction in absorption coefficient as the ratio tends farther away from 1.

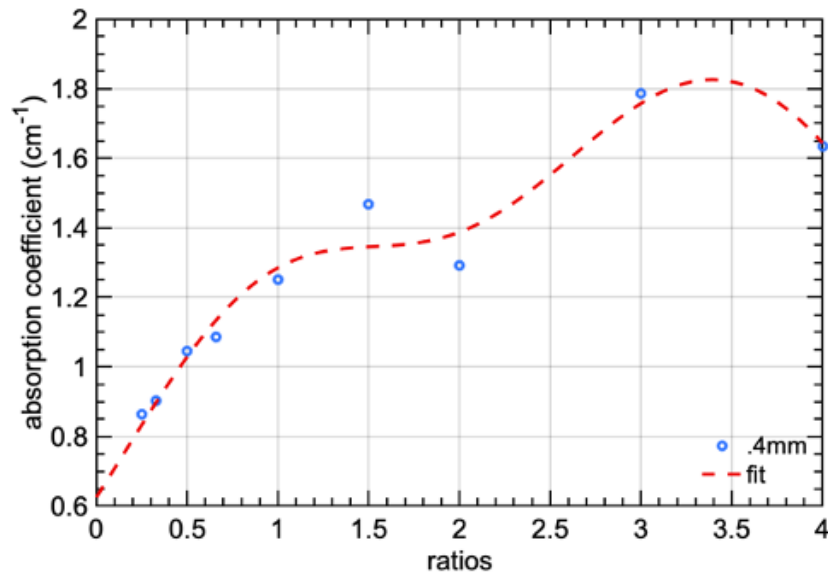


Figure 36: Simulated optical transparency for printed plain PMMA parts. Blue circles show data points for 0.4 mm layer height parts, and red dashed line shows the fit using a double Gaussian curve.

Both experiment and simulation suggest reducing the ratio as much as possible should result in the maximum optical transparency. For this reason, the layer height was reduced to 0.05 mm and the line width set to 0.4 mm, giving a ratio of 0.125, or 8 for the vertically printed version. The printed parts are shown in Figure 37(a,b). The UV/Vis absorption was measured and is plotted against the previous data in Figure 37(c). As seen, the measured absorption coefficient matches the previously generated curve fit, showing excellent agreement with predictions.

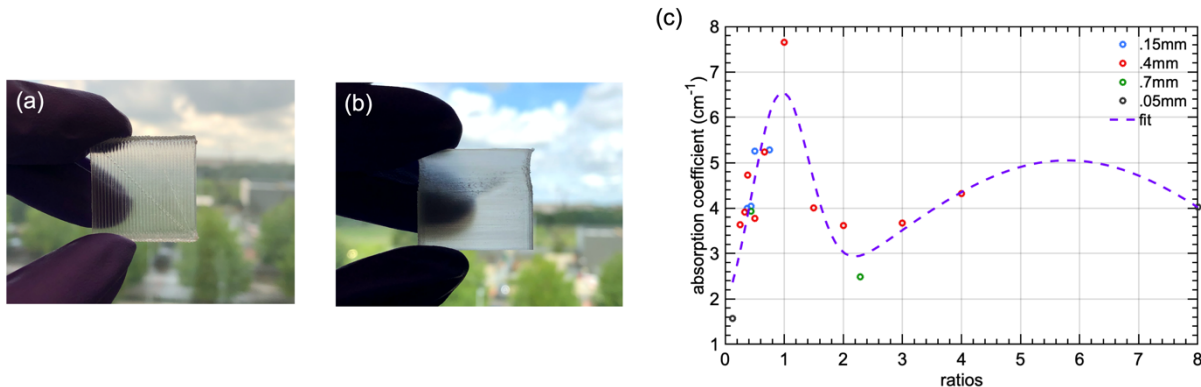


Figure 37: Pictures of optimized printed parts, using 0.05 mm layer height and 0.4 mm line width, in a (a) zigzag and (b) vertical pattern. (c) Plot of absorption coefficient vs. different height/width ratios, including the 0.05 mm layer height parts in black circles and the double Gaussian curve fit in purple.

The next step was to optimize the print pattern. Various patterns are available in Cura,⁹⁷ but the only ones allowing for 100% infill are concentric and zigzag. Figure 38 shows the various printing patterns considered in this study. First is a sample printed with built-in settings as a control sample. The second, third, and fourth parts are printed with concentric, zigzag, and vertical patterns, respectively. Note that the vertical pattern uses the zigzag printing method on a vertically oriented part.

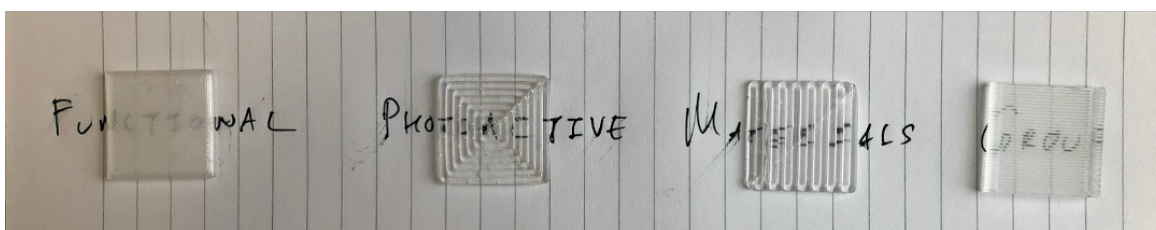


Figure 38: Picture of various printing patterns considered in this study. From left to right: normal settings shown as a control, concentric printing, zigzag printing, and vertical printing.

UV/Vis absorption spectroscopy was used to evaluate the optical characteristics of the different patterns. This was conducted in two configurations: first the typical z -axis measurement where the light source passes through the thickness of the part, and second an xy -axis measurement where the light passes through the width of the part. Schematics of each method are shown below each plot in Figure 39.

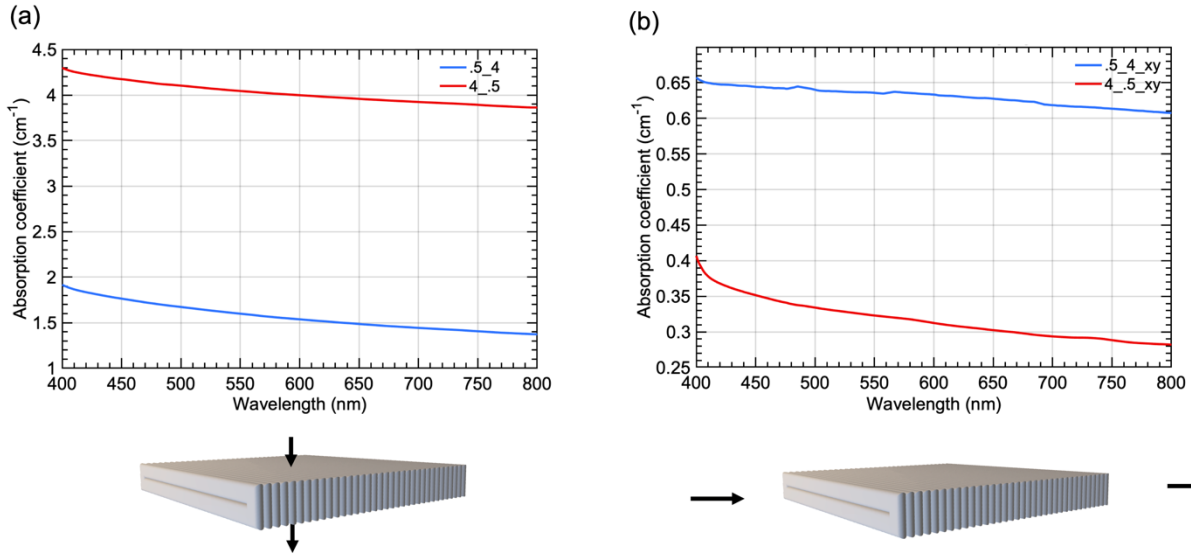


Figure 39: UV/Vis absorption data for zigzag printed parts in blue (.5_4) and vertically printed parts in red (4_.5). (a) Shows z-axis absorption coefficient as a function of wavelength along with a schematic showing direction of incident and output light, (b) shows x/y-axis absorption coefficient also with a schematic.

As seen, the zigzag printed part has better transparency in the z -axis, while the vertically printed part has better x/y -axis transparency. This is unfortunately a tradeoff in FDM 3D printing, and it is difficult to get high transparency in both dimensions. These transparency results help corroborate the claims about interface transparency introduced in Section 4.1. For both z - and x/y -axis absorption results, the part with layers oriented normal to the incident beam has better transparency, indicating the interfaces between print layers are well bonded.

With these optimized printing parameters, it is now possible to proceed to 3D printing luminescent parts.

5.4.2. Luminescent Parts

For luminescent filament, the nozzle temperature had to be increased slightly to 250°C, likely due to the increased viscosity of the filament caused by LR305 particles distributed in the polymer matrix. All other printing parameters remained unchanged.

Figure 40 shows 3D printed rectangular LSCs with various printing patterns. The nominal dimensions for all LSCs were $12.5 \times 12.5 \times 1.6$ mm, with slight variations due to minor inaccuracies in printing. The top row shows transparency of the parts when held up to sunlight, while the bottom row shows re-emission of absorbed sunlight. Note a new printing method of alternating zigzag was introduced here; this is simply a zigzag pattern that alternates direction between 0° and 90° every other layer.

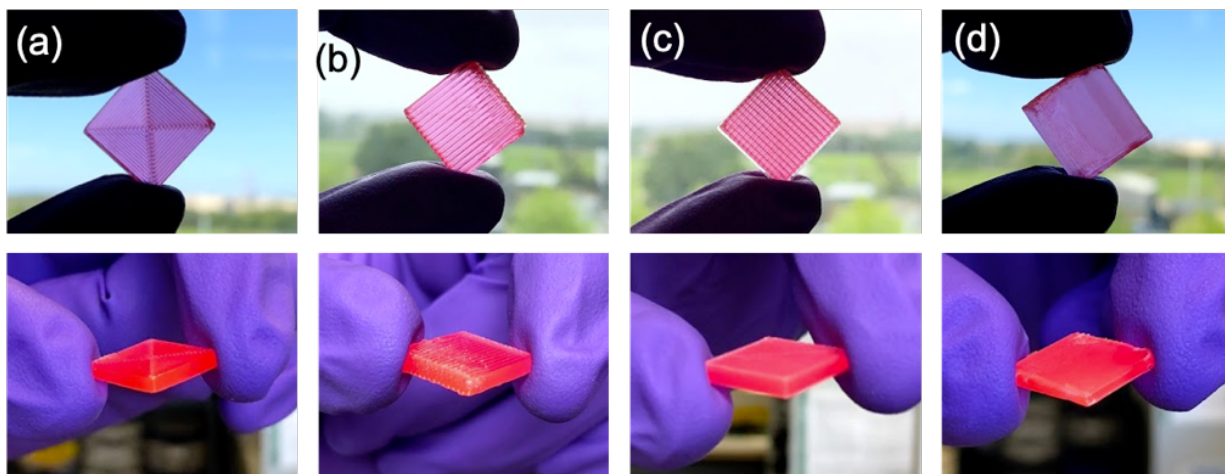


Figure 40: Pictures of 3D printed rectangular LSCs. Top row showing optical transparency to outdoor sunlight, bottom row showing re-emission of absorbed sunlight. 4 columns depicting different printing methods: (a) concentric, (b) zigzag, (c) alternating zigzag, (d) vertical.

Preliminary characterization of the luminescent 3D printed samples was conducted to ensure the transparency remained comparable to plain PMMA parts, as shown in Figure 41. Note that the transparency can only be compared beyond 650 nm, where the lumophore has no activity. As expected, the concentric, zigzag, and vertical patterned parts have similar absorption coefficient to their corresponding plain PMMA parts, (*cf.* Figure 39(a)). Note that slight increases in transparency are expected due to the higher quality of commercial PMMA filament used in plain PMMA parts.

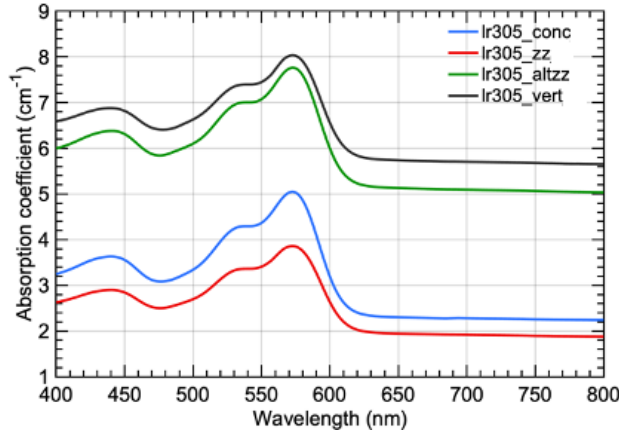


Figure 41: Absorption coefficient vs. wavelength for various printed parts with a 0.05 mm layer height. Concentric (lr305_conc) and zigzag (lr305_zz) printed parts have similar, low absorption coefficient, while alternating zigzag (lr305_altzz) and vertical (lr305_vert) have higher coefficients.

Now that 3D printing of luminescent parts has been proven to work, it is possible to print other shapes. For ease of efficiency measurement, flat-faced shapes were printed, including a triangle, hexagon, and cut circle. The exact top surface area for all shapes is reported in Table 4, along with their geometric gains, defined as the ratio of the top surface area to the total edge area. Since these parameters are reasonably similar, direct efficiency comparison can be made.

Table 4: Top surface areas and geometric gains for all 3D printed LSC geometries.

LSC Shape	Top Surface Area (mm ²)	Geometric Gain
Rectangle	156	1.95
Circle	151	2.09
Hexagon	154	2.18
Triangle	145	1.65

The concentric, zigzag, and (in some cases) alternating zigzag printing patterns were used due to their ease of applicability to a variety of designs. Figure 42(a) shows concentric printed parts under sunlight illumination, while Figure 42(b) shows concentric

and zigzag printed parts under UV illumination. Note the strong edge emission of the 3D printed parts.



Figure 42: (a) Picture of concentric printed parts under natural sunlight illumination. (b) Picture of concentric (bottom row) and zigzag (top row) printed parts under UV illumination.

5.4.3. Bulk parts

While the 3D printed parts qualitatively look promising, it is necessary to measure the efficiency of the samples and compare them against conventionally manufactured parts to get a better understanding of the performance. A slab of bulk PMMA (3.8 mm thick) doped with LR305 was milled down to 1.6 mm thickness and laser cut to match the 3D printed samples, giving bulk box, circle, hexagon, and triangle geometries. Figure 43(a) shows the parts under sunlight, while Figure 43(b) shows the parts under UV illumination.



Figure 43: (a) Picture of laser cut PMMA + LR305 LSC under natural sunlight illumination. (b) Picture of laser cut LSCs under UV illumination.

The UV/Vis absorption spectra of these parts were measured to determine the approximate background absorption coefficient of the PMMA. Figure 44(a) shows the absorption spectrum from 400 to 800 nm, which is useful in determining the concentration of LR305 in the sample (*ca.* 108 ppm), and Figure 44(b) shows the absorption spectrum from 650 to 800 nm, useful to determine the background absorption coefficient of the PMMA host (calculated to be 0.21 cm^{-1}). The small variations in the 650-800 nm region can be attributed to photo-/thermo-initiators used in polymerization of the sample.

Now that we have control samples to compare against, we can move onto optical characterization of the 3D printed parts.

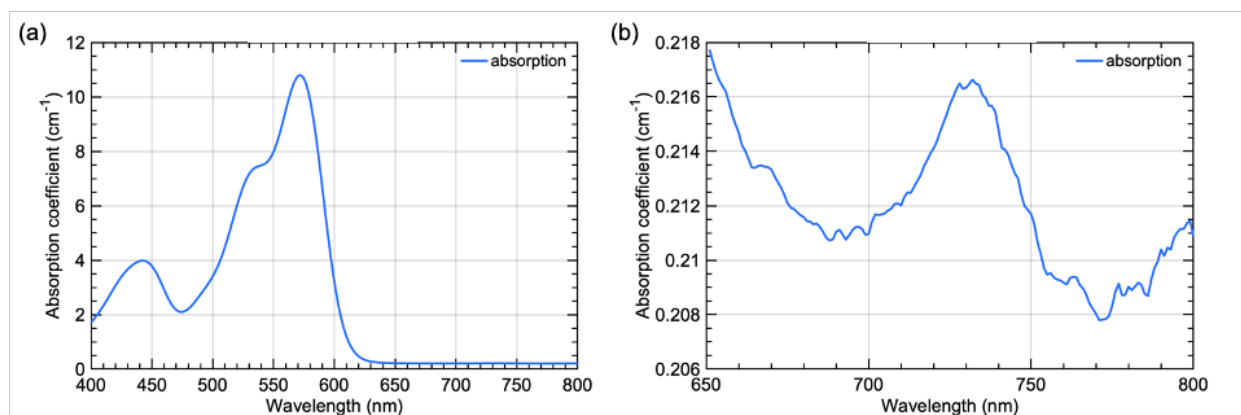


Figure 44: Absorption coefficient as a function of wavelength for laser cut PMMA + LR305 samples. (a) 400 to 800 nm range, and (b) 650 to 800 nm range to avoid the influence of LR305.

5.5. Optical Characterization

Optical efficiency measurements were made using a solar simulator, as detailed in Section 4.5.2. Note again that all references to optical efficiency correspond to external photon efficiency (η_{ext}). Appendix Section 9.3.1 contains the raw data collected from the solar simulator for edge emission of all parts, as well as the incident light spectrum. Figure 45 shows measured efficiency for each part, calculated by summing the edge emission intensity at each side of the part and dividing by the incident light intensity.

The data in Figure 45 provide unique insights about a variety of characteristics of 3D printed LSCs. First, the variation in efficiency of the bulk parts can be attributed to various factors. Because only one part of each geometry was created, there could have been variations in the quality of the parts. Additionally, while the frontal area was made consistent across parts, the gain varied, which could impact efficiency. Regardless, the important part is the comparison of efficiency of bulk parts to 3D printed parts.

It is immediately evident that the efficiency of many 3D printed devices is within a few percent of their bulk counterparts, even considering error bars, which is promising. We can go further in our analysis of their performance – by splitting up the efficiency measurements into various wavelength ranges, we can alter the effects of scattering.

To illustrate this point, consider the edge emission of a concentric printed box against the incident solar spectrum, as shown in Figure 46; it is evident that some regions are artificially inflated due to scattering. For example, the peak between 450 to 500 can be attributed to a peak in incident light at 450 to 500, implying scattering is causing this edge emission, rather than the action of the lumophore. Similarly, the peaks above 700 nm can be closely matched to peaks in incident light in the same range. Thus, by selecting specific wavelength ranges, it is possible to reduce the effect of scattering and isolate the contributions of the lumophore to edge emission.

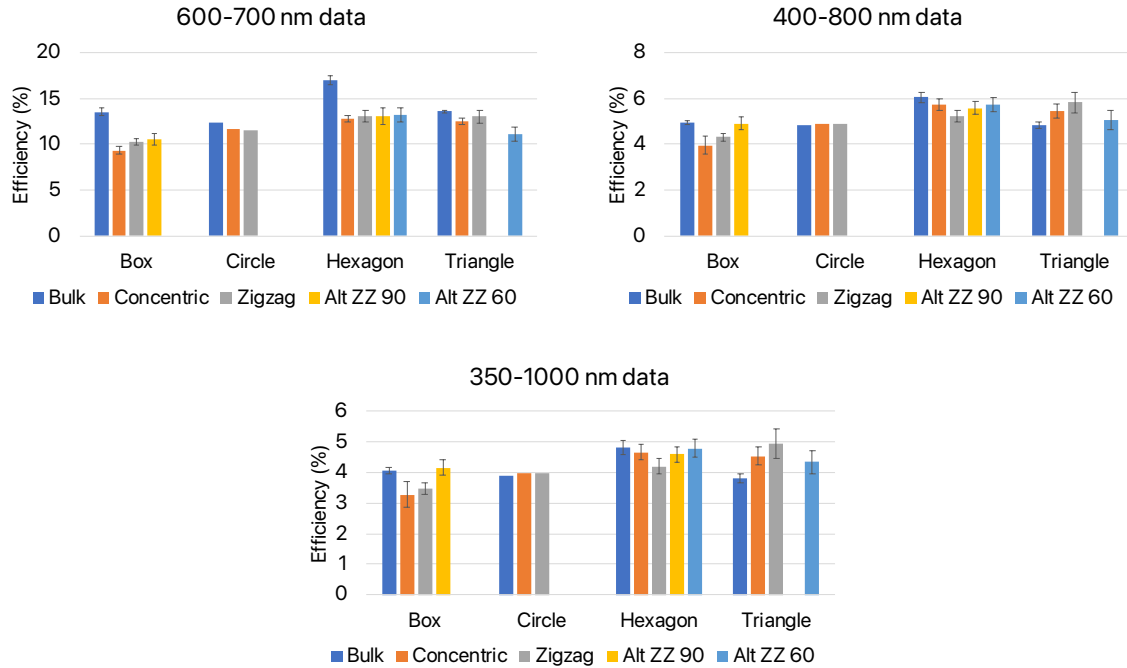


Figure 45: Experimentally measured efficiency for various LSC geometries fabricated either by conventional manufacturing techniques (bulk) or with 3D printing (concentric, zigzag, alternating zigzag). Efficiency measurements are presented for various wavelength ranges to vary the effects of scattering on efficiency. Error bars calculated from standard deviation of edge emission measurement for each side. Percentage data found in Table 11 in the Appendix.

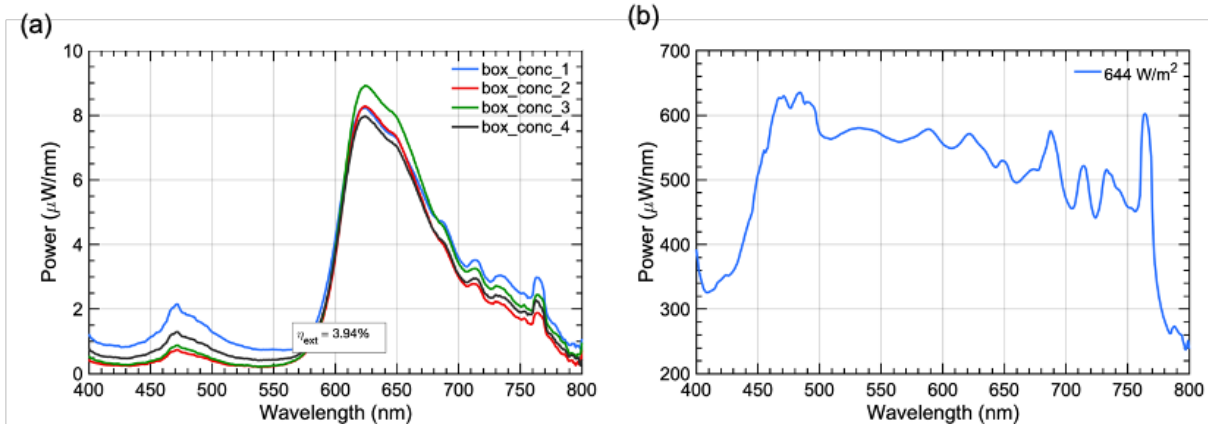


Figure 46: (a) Example edge emission for concentric printed box of wavelength range 400 to 800. (b) Incident light spectrum from solar simulator.

For example, by considering the 600-700 nm range, it is possible to eliminate most scattering events, though clearly not all of them. This will overestimate the actual device efficiency, since light is being absorbed that is not counted (between 300 and 600 nm for

LR305), but for the purposes of comparison between different devices, this methodology is still useful.

For the 600-700 nm range, Figure 45 shows that the bulk geometries clearly outperform the 3D printed parts, although some parts including the concentric circle and zigzag triangle come close to the bulk efficiency. Expanding the wavelength range to 400-800 nm shows some printed parts exceed the efficiency of bulk parts, including the printed circles and triangles. Further expanding the range to 350-1000 nm shows several printed parts beating bulk parts, including the alternating zigzag box, circles, alternating zigzag hexagon, and triangles.

This analysis suggests the scattering caused by the 3D printing process is actually beneficial and improves the overall efficiency of the LSC. This is further promising as the filament produced in this study is not fully optimized as the absorption is still fairly high, suggesting commercially produced filament could boost the efficiency of 3D printed LSCs even further. However, it is important to note that these are still small-scale devices, so the beneficial effects of the scattering could be overstated in these samples.

The next step to verifying these experimental results is to model the printed parts and calculate their simulated optical efficiency in pvTrace. This is first done using the *surface normal* method discussed in Section 4.2.3, using a wavelength range of 400 to 800 nm. The results for the simulated box LSCs are shown in column 3 of Table 5.

Here, we see reasonable agreement between the measured and simulated optical efficiency of the 3D printed parts, but the simulated performance of the bulk part is vastly overestimated. The bulk part should be the easiest to model, suggesting an issue with the simulation. One potential disparity between the simulation and the experimental setup is the inclusion of the mask for experimental measurements, as seen in Figure 27(b). There is an approximately 4 mm distance between the LSC and the integrating sphere, with the

distance bridged by the mask. It is likely the mask absorbs some light emitted from the edge rather than transmitting it to the integrating sphere. For this reason, the *surface normal* method of efficiency calculation is unsuitable. Instead, the *enclosing box* method may be more applicable to this situation. An enclosing box with edges 4 mm away from the LSC was created, and the simulated efficiencies are reported in column 4 of Table 5.

Table 5: Simulated efficiency of 3D printed LSCs using the enclosing box method to correct for mask usage in experimental setup. Measured efficiency and surface normal simulated efficiency included for comparison convenience.

LSC Geometry	Measured Ext. Phot. Eff.	Simulated Ext. Phot. Eff. (Surface Normal)	Simulated Ext. Phot. Eff. (Enclosing Box)
Bulk	4.94%	14.06%	4.31%
Concentric	3.95%	4.88%	4.20%
Zigzag	4.30%	6.07%	5.17%
Alt. zigzag	4.91%	6.16%	4.96%
Vertical	4.27%	5.18%	3.17%

The *enclosing box* method results in simulated optical efficiencies that are in much better agreement with the measured values for both printed and bulk parts. However, there is no clear systematic under- or over-estimation, perhaps because there are reasons for either to occur. The model could underestimate efficiency since it assumes the mask absorbs all rays, while in reality the mask may reflect a fraction of rays. On the other hand, it could overestimate efficiency due to lack of control over surface properties and imperfections, use of a constant waveguide background absorption, and assumption of 100% PLQY. A combination of these factors in different magnitudes could explain why the model underestimates in certain cases while overestimating in others.

Regardless, the *enclosing box* method does a better job of predicting performance of the bulk part and most 3D printed parts than the *surface normal* method. It is also interesting to note the difference in efficiency reduction between the bulk part and the 3D printed parts when switching to the *enclosing box* method. The bulk part showed a reduction of 66%, while on average the 3D printed parts only reduced efficiency by 22%. This suggests the 3D printed parts are better at directional emission than bulk parts, as more of their re-emitted light is likely to exit the LSC at the correct direction.

As mentioned before, the extruded filament in this study has higher absorption than commercially available filament. Now that we have verified the accuracy of our simulations against experimental data, it is possible to extrapolate these results to parts with low absorption to predict their performance.

First, note that in Figure 32 it was demonstrated that commercial PMMA filament had approximately 66% the absorption coefficient of extruded PMMA filament. However, because the filament was so thin (~ 2 mm diameter), the UV/Vis absorption may not be accurate as there might be significant scattering caused by the cylindrical filament that would not be present in the printed part. Instead, Figure 44 shows the background absorption coefficient of a commercially produced LSC, which should be a better indicator of the true absorption coefficient of commercially produced filament. Table 6 below shows the results of simulations using either the measured background absorption coefficient of the commercial filament or the commercial LSC, with the *surface normal* method of efficiency calculation.

Table 6: Simulated LSC efficiency for devices with lower absorption coefficients than in the current study. (high abs) column corresponds to the absorption coefficients in the current study, (med abs) corresponds to 66% of the current absorption coefficient, and (low abs) corresponds to absorption matching the commercial PMMA+LR305 slab.

LSC Geometry	Simulated Ext. Phot. Eff. (high abs)	Simulated Ext. Phot. Eff. (medium abs)	Simulated Ext. Phot. Eff. (low abs)
Bulk	–	–	14.06%
Concentric	4.88%	7.31%	15.97%
Zigzag	6.07%	8.23%	15.96%
Alt. zigzag	6.16%	8.74%	26.26%
Vertical	5.18%	6.70%	10.02%

From these results, we can predict the performance of future parts that would have better absorption characteristics than those in the current study. It is evident that 3D printed parts generally would have comparable efficiency to bulk parts, with some parts out-performing bulk parts. Additionally, 3D printed parts would have the benefits presented earlier of improved directionality of emission. This directionality would mimic lumophore alignment on a macro scale to direct light in a certain desired direction, increasing the functionality of 3D printed devices. With the combined benefit of high efficiency and built-in directionality, 3D printed LSCs could have promising applications.

In this results section, we have covered end-to-end analysis of 3D printed parts – initial CAD file generation, fine tuning the 3D printing process, measuring efficiency and comparing it to simulation, and extrapolating results to predict performance of better fabricated parts. While these preliminary results are promising, there are several areas that require future work, as discussed in the next section.

6. Future Work

Immediate future work would include obtaining additional measurements of the already-printed samples to further characterize their performance. First and foremost would be to simulate the other printed geometries (triangle, hexagon, cut circle) in pvTrace to ensure the simulation methods remain accurate. Additional experimental measurements could include scattering measurements – Appendix Section 9.3.2 begins some of this analysis based on the solar simulator data, but using an experimental setup dedicated to measuring scattering, such as described in Appendix Section 9.2.3.7, would be more beneficial. Additional UV-Vis measurements could be used to validate the claim in Section 4.1 that the impact of vertical interfaces is minimal. Additional measurements using polarized light could be used to validate the claims of dye alignment. Further, designing a new mask for edge emission measurement could both increase the quality of measurements and also allow for measurement of emission as a function of angular direction, which could quantitatively show directional emission. Finally, using solar cells to measure edge emission would more closely match the *surface normal* method in simulation and provide additional experimental verification of simulated results.

Beyond additional characterization, the parts themselves could be improved. Printing larger-scale parts would help isolate absorption vs. scattering effects. Sanding or laser cutting the edges would improve the surface properties of printed parts. Finally, solvent casting or LR305 functionalization (Appendix Section 9.2.2.3) could perhaps achieve better dispersion of lumophore in the polymer matrix and improve efficiency.

On a broader scale, the results of this study present promising directions for expansion of the field. The parts printed in this work were largely extrusions of 2D designs, so conventional manufacturing techniques are capable of fabricating these parts. (Although they would be wasteful, for example the 3.8 mm thick PMMA+LR305 stock

had to be milled down to 1.6 mm and then laser cut, wasting several cubic centimeters of usable material.) The next step would be to print truly 3D parts that would be impossible to make using subtractive manufacturing and to characterize their performance.

The fact that FDM 3D printing already provides promising results should also bode well for other types of 3D printing. SLA printing should also be investigated in future work, as the photopolymerization techniques used in SLA could achieve better bonding between layers and printing paths, improving optical transparency of the parts. It would be interesting to see how the reduction of interfaces (and therefore scattering) in SLA printing might impact efficiency.

7. Conclusions

In this study, we have conducted end-to-end performance analysis of 3D printed LSCs, starting with ray tracing simulation and ending with optical characterization of the printed parts. Both simulation and experiment confirm that 3D printed LSCs could have as high or even higher efficiency than conventionally manufactured parts, with the potential added benefit of improved directionality of edge emission in 3D printed parts.

As the first study to 3D print LSCs, much of the methodology had to be developed from scratch or adapted from other works. A 5-step cycle for 3D printing LSCs was introduced, which includes: generation of an accurate CAD model, ray trace analysis on this model, generation of luminescent filament, 3D printing the part, and characterization of the optical efficiency of the part.

A novel way of generating CAD models has been developed, based on an open-source G-code interpreter, that mimics the intricacies of the 3D printed part, including interfaces between paths and the cross-sectional profile of the paths. Additions to the open-source ray tracing software pvTrace were developed to simplify simulation of unconventional geometries. The results of these simulations indicate a potential for twofold increase in the optical efficiency of LSCs when using 3D printing versus conventional manufacturing.

Luminescent filament was generated through extrusion of physically mixed polymer host pellets and lumophore powder. The filament was then 3D printed with optimized parameters to result in high-transparency parts. To the author's knowledge, this study is the first to FDM print an optical waveguide with organic dye polymer filament.

Finally, optical characterization of printed parts showed that 3D printed parts have similar efficiency to conventional parts (within 1%). Analysis of the data indicates scattering may help boost the efficiency of printed parts by allowing more incident light

to reach the edges. Simulation suggests this scattering is actually waveguiding of incident and re-emitted light by the 3D printed paths to improve directionality of edge emission, but this is to be confirmed in future work. Extrapolation of the results of this study to 3D printed parts with more representative optical properties (i.e. lower absorption coefficient) indicated even better performance, with some 3D printed parts exhibiting the twofold efficiency increase predicted by simulation.

Overall, this study aimed to bridge the gap between additive manufacturing and LSCs. 3D printing allows fabrication of parts with a variety of shapes that would be impossible to make with conventional manufacturing techniques. It also reduces material waste and enables rapid prototyping. This study served as a preliminary test to prove 3D printing of LSCs is worth pursuing. While this study focused on a few basic LSC geometries, expansion to more complicated geometries would be interesting in the future.

At their core, LSCs are of interest when compared to traditional solar cells due to their ease of integration into the built environment. The increased customization as a result of 3D printing results in greater diversity of design, which creates more options for LSC installations. LSCs can thus be an incredibly useful complementary technology for solar photovoltaics, helping ease the transition to a cleaner future.

8. References

- 1 S. Mekhilef, R. Saidur and A. Safari, *Renew. Sustain. Energy Rev.*, 2011, 15, 1777–1790.
- 2 N. Kannan and D. Vakeesan, *Renew. Sustain. Energy Rev.*, 2016, 62, 1092–1105.
- 3 L. qun Liu, Z. xin Wang, H. qiang Zhang and Y. cheng Xue, *Renew. Sustain. Energy Rev.*, 2010, 14, 301–311.
- 4 K. Kapoor, K. K. Pandey, A. K. Jain and A. Nandan, *Renew. Sustain. Energy Rev.*, 2014, 40, 475–487.
- 5 A. Bahadori and C. Nwaoha, *Renew. Sustain. Energy Rev.*, 2013, 18, 1–5.
- 6 K. H. Solangi, M. R. Islam, R. Saidur, N. A. Rahim and H. Fayaz, *Renew. Sustain. Energy Rev.*, 2011, 15, 2149–2163.
- 7 G. K. Singh, *Energy*, 2013, 53, 1–13.
- 8 L. L. Kazmerski, *Renew. Sustain. Energy Rev.*, 1997, 1, 71–170.
- 9 M. A. G. De Brito, L. P. Sampaio, L. G. Junior and C. A. Canesin, in *COBEP 2011 - 11th Brazilian Power Electronics Conference*, 2011, pp. 531–537.
- 10 L. El Chaar, L. A. Lamont and N. El Zein, *Renew. Sustain. Energy Rev.*, 2011, 15, 2165–2175.
- 11 Z. Fan, K. Sun and J. Wang, *J. Mater. Chem. A*, 2015, **3**, 18809–18828.
- 12 A. K. Chilvery, A. K. Batra, B. Yang, K. Xiao, P. Guggilla, M. D. Aggarwal, R. Surabhi, R. B. Lal, J. R. Currie and B. G. Penn, *J. Photonics Energy*, 2015, **5**, 057402.
- 13 T. D. Lee and A. U. Ebong, *Renew. Sustain. Energy Rev.*, 2017, 70, 1286–1297.
- 14 J. Yu, Y. Zheng and J. Huang, *Polymers (Basel)*, 2014, **6**, 2473–2509.
- 15 M. G. Debije and P. P. C. Verbunt, *Adv. Energy Mater.*, 2012, 2, 12–35.
- 16 B. McKenna and R. C. Evans, *Adv. Mater.*, 2017, **29**, 1606491.
- 17 D. J. Farrell and M. Yoshida, *Prog. Photovoltaics Res. Appl.*, 2012, **20**, 93–99.
- 18 L. R. Wilson, *Eng. Phys. Sci.*, 2010, 369.
- 19 I. Gibson, D. W. Rosen and B. Stucker, *Additive manufacturing technologies: Rapid prototyping to direct digital manufacturing*, Springer US, 2010.
- 20 T. D. Ngo, A. Kashani, G. Imbalzano, K. T. Q. Nguyen and D. Hui, *Compos. Part B Eng.*, 2018, 143, 172–196.
- 21 S. H. Huang, P. Liu, A. Mokeddar and L. Hou, *Int. J. Adv. Manuf. Technol.*, 2013, 67, 1191–1203.
- 22 Z. Chen, Z. Li, J. Li, C. Liu, C. Lao, Y. Fu, C. Liu, Y. Li, P. Wang and Y. He, *J. Eur. Ceram. Soc.*, 2019, 39, 661–687.
- 23 D. G. Moore, L. Barbera, K. Masania and A. R. Studart, *Nat. Mater.*, , DOI:10.1038/s41563-019-0525-y.
- 24 A. Le Duigou, M. Castro, R. Bevan and N. Martin, *Mater. Des.*, 2016, **96**, 106–114.
- 25 W. E. Frazier, *J. Mater. Eng. Perform.*, 2014, 23, 1917–1928.
- 26 B. Evans, *Practical 3D printers*, Apress, 2012.
- 27 B. C. Gross, J. L. Erkal, S. Y. Lockwood, C. Chen and D. M. Spence, *Anal. Chem.*, 2014, **86**, 3240–3253.
- 28 F. C. Krebs, *Sol. Energy Mater. Sol. Cells*, 2009, 93, 394–412.
- 29 T. M. Eggenhuisen, Y. Galagan, A. F. K. V. Biezemans, T. M. W. L. Slaats, W. P. Voorthuijzen, S. Kommeren, S. Shanmugam, J. P. Teunissen, A. Hadipour, W. J. H. Verhees, S. C. Veenstra, M. J. J. Coenen, J. Gilot, R. Andriessen and W. A. Groen, *J. Mater. Chem. A*, 2015, **3**, 7255–7262.

- 30 X. Peng, J. Yuan, S. Shen, M. Gao, A. S. R. Chesman, H. Yin, J. Cheng, Q. Zhang and D. Angmo, *Adv. Funct. Mater.*, 2017, **27**, 1703704.
- 31 M. Zettl, O. Mayer, E. Klampaftis and B. S. Richards, *Energy Technol.*, 2017, **5**, 1037–1044.
- 32 G. Griffini, *Front. Mater.*, , DOI:10.3389/fmats.2019.00029.
- 33 D. Zaremba, R. Evert, J. Kielhorn, F. Jakobs, R. Caspary, W. Kowalsky and H.-H. Johannes, *Polym. Int.*, 2018, **67**, 1179–1185.
- 34 F. Gianfaldoni, F. De Nisi, G. Iasilli, A. Panniello, E. Fanizza, M. Striccoli, D. Ryuse, M. Shimizu, T. Biver and A. Pucci, *RSC Adv.*, 2017, **7**, 37302–37309.
- 35 R. Mori, G. Iasilli, M. Lessi, A. B. Muñoz-García, M. Pavone, F. Bellina and A. Pucci, *Polym. Chem.*, 2018, **9**, 1168–1177.
- 36 Y. Li, X. Zhang, Y. Zhang, R. Dong and C. K. Luscombe, *J. Polym. Sci. Part A Polym. Chem.*, 2019, **57**, 201–215.
- 37 BASF, *Lumogen F Collector Dyes: Technical Information* , 1997.
- 38 L. H. Slooff, E. E. Bende, A. R. Burgers, T. Budel, M. Pravettoni, R. P. Kenny, E. D. Dunlop and A. Büchtemann, *Phys. status solidi - Rapid Res. Lett.*, 2008, **2**, 257–259.
- 39 M. G. Debije, P. P. C. Verbunt, B. C. Rowan, B. S. Richards and T. L. Hoeks, *Appl. Opt.*, 2008, **47**, 6763–6768.
- 40 L. R. Wilson, B. C. Rowan, N. Robertson, O. Moudam, A. C. Jones and B. S. Richards, *Appl. Opt.*, 2010, **49**, 1651–1661.
- 41 Z. Krumer, W. G. J. H. M. van Sark, R. E. I. Schropp and C. de Mello Donegá, *Sol. Energy Mater. Sol. Cells*, 2017, **167**, 133–139.
- 42 R. Reifeld and C. K. Jorgensen, *Struct. Bond.*, 1982, 1–36.
- 43 L. Desmet, A. J. M. Ras, D. K. G. de Boer and M. G. Debije, *Opt. Lett.*, 2012, **37**, 3087.
- 44 E. Loh and D. J. Scalapino, *Appl. Opt.*, 1986, **25**, 1901.
- 45 S. Tsoi, D. J. Broer, C. W. Bastiaansen and M. G. Debije, *Opt. Express*, 2010, **18**, A536.
- 46 P. T. M. Albers, C. W. M. Bastiaansen and M. G. Debije, *Sol. Energy*, 2013, **95**, 216–223.
- 47 P. P. C. Verbunt, A. Kaiser, K. Hermans, C. W. M. Bastiaansen, D. J. Broer and M. G. Debije, *Adv. Funct. Mater.*, 2009, **19**, 2714–2719.
- 48 B. J. Bruijnaers, A. P. H. J. Schenning and M. G. Debije, *Adv. Opt. Mater.*, 2015, **3**, 257–262.
- 49 R. H. Inman, G. V. Shcherbatyuk, D. Medvedko, A. Gopinathan and S. Ghosh, *Opt. Express*, 2011, **19**, 24308.
- 50 S. F. H. Correia, P. P. Lima, P. S. André, M. R. S. Ferreira and L. A. D. Carlos, *Sol. Energy Mater. Sol. Cells*, 2015, **138**, 51–57.
- 51 J. J. H. Videira, E. Bilotti, A. J. Chatten and J. W. H. Weber, *Opt. Express*, , DOI:10.1364/OE.24.0A1188.
- 52 K. R. Mcintosh, N. Yamada and B. S. Richards, *Appl. Phys. B*, 2007, **88**, 285–290.
- 53 B. Vishwanathan, A. H. M. E. Reinders, D. K. G. de Boer, L. Desmet, A. J. M. Ras, F. H. Zahn and M. G. Debije, *Sol. Energy*, 2015, **112**, 120–127.
- 54 I. A. Carbone, K. R. Frawley and M. K. McCann, *Int. J. Photoenergy*, 2019, **2019**, 1–9.
- 55 M. Kennedy, S. J. McCormack, J. Doran and B. Norton, in *ISES Solar World Congress 2007, ISES 2007*, 2007, vol. 2, pp. 1484–1488.
- 56 M. D. Hughes, C. Maher, D. A. Borca-Tasciuc, D. Polanco and D. Kaminski, *Renew. Energy*, 2013, **52**, 266–272.
- 57 A. Reinders, M. G. Debije and A. Rosemann, *IEEE J. Photovoltaics*, 2017, **7**, 1663–1666.
- 58 M. G. Debije, J. P. Teunissen, M. J. Kastelij, P. P. C. Verbunt and C. W. M. Bastiaansen, *Sol.*

- Energy Mater. Sol. Cells*, 2009, **93**, 1345–1350.
- 59 F. Mateen, H. Oh, J. G. Kang, S. Y. Lee and S. K. Hong, *Renew. Energy*, 2019, **138**, 691–696.
- 60 D. T. Pham and R. S. Gault, *Int. J. Mach. Tools Manuf.*, 1998, **38**, 1257–1287.
- 61 O. A. Mohamed, S. H. Masood and J. L. Bhowmik, *Adv. Manuf.*, 2015, **3**, 42–53.
- 62 E. Tekin, B. J. De Gans and U. S. Schubert, *J. Mater. Chem.*, 2004, **14**, 2627–2632.
- 63 B.-J. de Gans and U. S. Schubert, *Macromol. Rapid Commun.*, 2003, **24**, 659–666.
- 64 J. Alamán, R. Alicante, J. I. Peña and C. Sánchez-Somolinos, *Materials (Basel)*, 2016, **9**.
- 65 Y. He, Y. Wu, J. Fu, Q. Gao and J. Qiu, *Electroanalysis*, 2016, **28**, 1658–1678.
- 66 X. Wang, M. Jiang, Z. Zhou, J. Gou and D. Hui, *Compos. Part B Eng.*, 2017, **110**, 442–458.
- 67 M. R. Hartings and Z. Ahmed, *Nat. Rev. Chem.*, 2019, **3**, 305–314.
- 68 J. O. Palaganas, N. B. Palaganas, L. J. I. Ramos and C. P. C. David, *ACS Appl. Mater. Interfaces*, 2019, **11**, 46034–46043.
- 69 D. Pintossi, A. Colombo, M. Levi, C. Dragonetti, S. Turri and G. Griffini, *J. Mater. Chem. A*, 2017, **5**, 9067–9075.
- 70 F. Castles, D. Isakov, A. Lui, Q. Lei, C. E. J. Dancer, Y. Wang, J. M. Janurudin, S. C. Speller, C. R. M. Grovenor and P. S. Grant, *Sci. Rep.*, , DOI:10.1038/srep22714.
- 71 M. R. Skorski, J. M. Esenther, Z. Ahmed, A. E. Miller and M. R. Hartings, *Sci. Technol. Adv. Mater.*, 2016, **17**, 89–97.
- 72 L. Alison, S. Menasce, F. Bouville, E. Tervoort, I. Mattich, A. Ofner and A. R. Studart, *Sci. Rep.*, , DOI:10.1038/s41598-018-36789-z.
- 73 M. A. León-Cabezas, A. Martínez-García and F. J. Varela-Gandía, *Procedia Manuf.*, , DOI:10.1016/j.promfg.2017.09.130.
- 74 E. Tekin, E. Holder, V. Marin, B.-J. de Gans and U. S. Schubert, *Macromol. Rapid Commun.*, 2005, **26**, 293–297.
- 75 C.-L. Tai, W.-L. Hong, Y.-T. Kuo, C.-Y. Chang, M.-C. Niu, M. Karupathevar Ponnusamythevar Ochath, C.-L. Hsu, S.-F. Horng and Y.-C. Chao, *ACS Appl. Mater. Interfaces*, 2019, **11**, 30176–30184.
- 76 S. Suresh Nair, A. Heinrich, M. Klein and S. Steenhusen, *SPIE-Intl Soc Optical Eng*, 2019, p. 4.
- 77 F. Frascella, G. González, P. Bosch, A. Angelini, A. Chiappone, M. Sangermano, C. F. Pirri and I. Roppolo, *ACS Appl. Mater. Interfaces*, 2018, **10**, 39319–39326.
- 78 J. Y. Kim, C. Ingrosso, V. Fakhfouri, M. Striccoli, A. Agostiano, M. L. Curri and J. Brugger, *Small*, 2009, **5**, 1051–1057.
- 79 E. Tekin, P. J. Smith, S. Hoepfener, A. M. J. van den Berg, A. S. Sussha, A. L. Rogach, J. Feldmann and U. S. Schubert, *Adv. Funct. Mater.*, 2007, **17**, 23–28.
- 80 Y. Zhou, K. Mintz, C. Oztan, S. Hettiarachchi, Z. Peng, E. Seven, P. Liyanage, S. De La Torre, E. Celik and R. Leblanc, *Polymers (Basel)*, 2018, **10**, 921.
- 81 R. Krini, C. W. Ha, P. Prabhakaran, H. El Mard, D.-Y. Yang, R. Zentel and K.-S. Lee, *Macromol. Rapid Commun.*, 2015, **36**, 1108–1114.
- 82 C. D. Brubaker, T. M. Frecker, J. R. McBride, K. R. Reid, G. K. Jennings, S. J. Rosenthal and D. E. Adams, *J. Mater. Chem. C*, 2018, **6**, 7584–7593.
- 83 M. Wan, X. Jiang, J. Nie, Q. Cao, W. Zheng, X. Dong, Z. H. Fan and W. Zhou, *J. Appl. Polym. Sci.*, 2019, 48644.
- 84 T. Rimpingpisarn, W. Wattanathana, K. Sukthavorn, N. Nootsuwan, Y. Hanlumyuang, C. Veranitisagul and A. Laobuthee, *Mater. Lett.*, 2019, **237**, 270–273.
- 85 F. Wang, Y. Chong, F. K. Wang and C. He, *J. Appl. Polym. Sci.*, , DOI:10.1002/app.44988.

86 A. Renny, C. Yang, R. Anthony and R. R. Lunt, *J. Chem. Educ.*, 2018, **95**, 1161–1166.
87 J. ter Schiphorst, M. L. M. K. H. Y. K. Cheng, M. van der Heijden, R. L. Hageman, E. L. Bugg,
T. J. L. Wagenaar and M. G. Debije, *Energy Build.*, 2019, 109625.
88 F. Zhao, D. Cambié, J. Janse, E. W. Wieland, K. P. L. Kuijpers, V. Hessel, M. G. Debije and T.
Noël, *ACS Sustain. Chem. Eng.*, 2018, **6**, 422–429.
89 C. Credi, D. Pintossi, C. L. Bianchi, M. Levi, G. Griffini and S. Turri, *Mater. Des.*, 2017, **133**,
143–153.
90 M. Carrascosa, S. Unamuno and F. Agullo-Lopez, *Appl. Opt.*, 1983, **22**, 3236.
91 D. Cambié, F. Zhao, V. Hessel, M. G. Debije and T. Noël, *React. Chem. Eng.*, 2017, **2**, 561–566.
92 A. Kerrouche, D. A. Hardy, D. Ross and B. S. Richards, *Sol. Energy Mater. Sol. Cells*, 2014, **122**,
99–106.
93 W. G. J. H. M. van Sark, K. W. J. Barnham, L. H. Slooff, A. J. Chatten, A. Büchtemann, A.
Meyer, S. J. McCormack, R. Koole, D. J. Farrell, R. Bose, E. E. Bende, A. R. Burgers, T. Budel,
J. Quilitz, M. Kennedy, T. Meyer, C. D. M. Donegá, A. Meijerink and D. Vanmaekelbergh, *Opt.*
Express, 2008, **16**, 21773.
94 R. Hardman, *Environ. Health Perspect.*, 2006, 114, 165–172.
95 U. Resch-Genger, M. Grabolle, S. Cavaliere-Jaricot, R. Nitschke and T. Nann, *Nat. Methods*, 2008,
5, 763–775.
96 K. Jakubowski, C. S. Huang, A. Gooneie, L. F. Boesel, M. Heuberger and R. Hufenus, *Mater.*
Des., 2020, **189**, 108518.
97 Ultimaker Cura: Powerful, easy-to-use 3D printing software,
<https://ultimaker.com/software/ultimaker-cura>, (accessed 16 July 2020).
98 blender.org - Home of the Blender project - Free and Open 3D Creation Software,
<https://www.blender.org/>, (accessed 5 September 2020).
99 S. Kirkby, GitHub - iraytrace/BlenderGcodeImport: Python script to load gcode files produced by
Slic3r into Blender, <https://github.com/iraytrace/BlenderGcodeImport>, (accessed 6 July 2020).
100 A. J. Chatten, D. J. Farrell, R. Bose, A. Dixon, C. Poelking, K. C. Gödel, M. Mazzer and K. W.
J. Barnham, in *Conference Record of the IEEE Photovoltaic Specialists Conference*, 2011, pp.
000852–000857.
101 D. J. Farrell, Imperial College London, 2008.
102 B. Rahul, F. D. J., C. A. J., P. MAURO, B. Andreas and B. K. W. J., .
103 Reference Air Mass 1.5 Spectra | Grid Modernization | NREL, [https://www.nrel.gov/grid/solar-
resource/spectra-am1.5.html](https://www.nrel.gov/grid/solar-resource/spectra-am1.5.html), (accessed 23 July 2020).
104 Release pvtrace-2.1.2 · danieljfarrell/pvtrace · GitHub,
<https://github.com/danieljfarrell/pvtrace/releases/tag/v2.1.2>, (accessed 5 September 2020).
105 pvtrace-sv/v2.1.sv at master · shomikverma/pvtrace-sv · GitHub,
<https://github.com/shomikverma/pvtrace-sv/tree/master/v2.1.sv>, (accessed 5 September 2020).
106 O. Y. Edelenbosch, M. Fisher, L. Patrignani, W. G. J. H. M. van Sark and A. J. Chatten, in
Optics InfoBase Conference Papers, Optical Society of America, 2012, vol. 21, pp. A503–A514.
107 pvtrace-sv/GUI at master · shomikverma/pvtrace-sv · GitHub,
<https://github.com/shomikverma/pvtrace-sv/tree/master/GUI>, (accessed 5 September 2020).
108 multiprocessing — Process-based parallelism — Python 3.8.6rc1 documentation,
<https://docs.python.org/3/library/multiprocessing.html>, (accessed 11 September 2020).
109 ray-project/ray: An open source framework that provides a simple, universal API for building
distributed applications. Ray is packaged with RLlib, a scalable reinforcement learning library,

- and Tune, a scalable hyperparameter tuning library., <https://github.com/ray-project/ray>, (accessed 11 September 2020).
- 110 Noztek Pro Desktop Filament Extruder | Produce your own Filament, <https://www.noztek.com/product/noztek-pro/>, (accessed 14 September 2020).
- 111 Original Prusa i3 MK3S - Prusa3D - 3D Printers from Josef Průša, <https://www.prusa3d.com/original-prusa-i3-mk3/>, (accessed 14 September 2020).
- 112 A. H. Zewail and ; J Samuel Batchelder, *Luminescent solar energy concentrator devices*, 1979.
- 113 Hotend PTFE tube (MK2.5S, MK3S, MMU2S) - Prusa Research, <https://shop.prusa3d.com/en/mk3mk3s/929-hotend-ptfe-tube-mk25s-mk3s-mmu2s.html>, (accessed 6 September 2020).
- 114 C. B. Murray, C. R. Kagan and M. G. Bawendi, *Annu. Rev. Mater. Sci.*, 2000, **30**, 545–610.
- 115 I. Roppolo, A. Chiappone, A. Angelini, S. Stassi, F. Frascella, C. F. Pirri, C. Ricciardi and E. Descrovi, *Mater. Horizons*, 2017, **4**, 396–401.
- 116 Cloud Powered 3D CAD/CAM Software for Product Design | Fusion 360, <https://www.autodesk.co.uk/products/fusion-360/overview>, (accessed 6 September 2020).
- 117 Downloads - Prusa3D - 3D Printers from Josef Průša, <https://www.prusa3d.com/drivers/>, (accessed 16 July 2020).
- 118 shomikverma/CustomCuraProfiles, <https://github.com/shomikverma/CustomCuraProfiles/tree/master>, (accessed 7 September 2020).
- 119 shomikverma/GCodetoSTLBlender, <https://github.com/shomikverma/GCodetoSTLBlender/tree/master>, (accessed 7 September 2020).
- 120 D. J. Farrell, GitHub - danieljfarrell/pvtrace: Optical ray tracing for luminescent materials and spectral converter photovoltaic devices, <https://github.com/danieljfarrell/pvtrace>, (accessed 6 July 2020).
- 121 GitHub - shomikverma/pvtrace-sv, <https://github.com/shomikverma/pvtrace-sv>, (accessed 5 September 2020).
- 122 P. S. Friedman, *Opt. Eng.*, 1981, **20**, 206887.
- 123 Research Computing Services HPC Documentation — CSD3 1.0 documentation, <https://docs.hpc.cam.ac.uk/hpc/>, (accessed 23 July 2020).
- 124 Laserscript LS3060 Pro CO2 Laser Cutter | HPC Laser, <https://hpclaser.co.uk/co2-laser-cutters/ls3060/>, (accessed 5 September 2020).

9. Appendix

9.1. Literature Review

9.1.1. 3D Printing Photoluminescent Parts

In order to make the resulting print glow, luminescent materials must be added to the polymers in one of two methods: covalent-grafting or doping. The most common luminescent materials used are quantum dots (QDs), rare earth ions, or organic dyes. Several past studies have successfully 3D printed photoluminescent parts using various printing techniques (inkjet, SLA, FDM), as summarized in Table 1.

QDs are interesting as fluorescent materials due to the ability to tune their emission wavelength based on their size.¹¹⁴ QD-polymer printing has been demonstrated in almost all types of 3D printing. For instance, inkjet printing of QDs has seen extensive success for the past decade. Kim *et al.* embedded CdSe/ZnS nanocrystals in a poly(styrene) (PS) matrix dissolved in chloroform for inkjet printing.⁷⁸ In 2007, Tekin *et al.* embedded CdTe nanocrystals in a PVA matrix for inkjet printing, and, with the addition of ethylene glycol to prevent ring formation, were able to produce both green-emitting and red-emitting inks by tuning the QD diameter.⁷⁹ More recently, SLA printing with QDs has become possible. In 2018, Zhou *et al.* embedded orange carbon dots into a sodium polyacrylate ink for use in SLA printing.⁸⁰ In 2019, Nair *et al.* used CdSe/ZnS QDs embedded in a hybrid polymer resin called ORMOCER for multimaterial SLA printing by varying the size of QDs.⁷⁶ Krini *et al.* were able to encapsulate CdSe and CdZnS QD's in a functionalized silica shell that was covalently bonded to the ORMOCER polymer matrix, and could be 3D printed with two-photon polymerization.⁸¹ There have even been some works developing filaments doped with QDs for FDM printing. Brubaker *et al.* dispersed CdSSe QDs in a PLA matrix

through solvent casting to produce a hard plastic, which was then shredded and extruded to form filament.⁸² Tai *et al.* expanded upon this work by developing filament with encapsulated FAPbBr₃ perovskite nanocrystals in a poly(caprolactone) (PCL) matrix.⁷⁵

Rare earth ions are also often used as fluorescent materials. Wan *et al.* incorporated SrAl₂O₄:Eu²⁺,Dy³⁺ phosphor powders modified with SiO₂ into a PLA matrix, forming green fluorescent filament using a melt blending method for FDM printing.⁸³ Rimpongpisarn *et al.* used a similar methodology to embed MgAl₂O₄:Sm³⁺ phosphor powders modified with 3-aminopropyl triethoxysilane in a PLA matrix to create a filament for FDM printing.⁸⁴ In 2005, Tekin *et al.* created copolymers with rare transition metals Ru(II) and Ir(III) bonded with polypyridyl and poly(methyl methacrylate) (PMMA) or PS, respectively, creating orange and yellow inks for inkjet printing.⁷⁴

Organic dyes are another type of additive used in luminescent 3D printing. Wang *et al.* dispersed common organic dyes (Rhodamine B, Solvent Yellow 98, and BBOT) with small stabilizing acrylate monomer additives in a di(ethylene glycol) diacrylate (DEGMA) resin for SLA/DLP printing, and they were able to produce brightly fluorescent printed parts.⁸⁵ Frascella *et al.* used a custom-created NBD-MA (an amino derivative of 7-nitrobenz-2-oxa-1,3-diazole functionalized with a methacrylic double bond) fluorescent dye covalently grafted to the monomer bisphenol A ethoxylate diacrylate (BEDA) for SLA printing.⁷⁷ An interesting note to include here is that most SLA printers require a dye by default to control light penetration and avoid over-polymerization, but these dyes typically are not luminescent and are thus generally useless in the printed object except for aesthetic appeal.⁷⁷ A more thoughtful use of dyes could thus potentially result in more versatile 3D printed objects.¹¹⁵

9.2. Experimental

The general methodology of this work is presented in Section 4. This appendix section provides specific details about the software, materials, and instrumentation used.

9.2.1. *Software*

Various software were used in the first two parts (as shown in Figure 11) of this study, CAD model generation and ray tracing modeling of the LSC. The specific software are detailed below.

9.2.1.1. *Autodesk Fusion 360*

Autodesk Fusion 360 is a cloud-based CAD software free for students and educators.¹¹⁶ Fusion 360 was used to CAD the bulk LSCs before passing them through the slicer software. The LSCs were manually created, which is straightforward to do given the simple geometry of bulk LSCs. Once the bulk design is finalized, it is saved as an STL file which can be exported to the slicer software.

9.2.1.2. *Ultimaker Cura*

Ultimaker Cura is a free commercial software used for 3D printing.⁹⁷ Its primary purpose is converting STLs into instructions for Ultimaker 3D printers. Since the Prusa MK3S printer was used in this study, a driver was downloaded to make the output from Cura compatible with Prusa printers.¹¹⁷ The slicing software slices the STL part into several layers and generates a path the printer nozzle should follow for each layer. While there are default settings, the user is able to change various settings based on the specific application desired. For this study, the biggest changes made were changing the layer

height and line width, increasing the infill percent to 100%, removing the walls, and reducing the print speed. Fan cooling of the part was also turned off to allow fusing of layers. The infill pattern was either zigzag or concentric, depending on the application, though concentric was used more often. The Cura settings used for this study can be found in profiles available on the author's Github.¹¹⁸

9.2.1.3. *Blender*

Blender is a free, open-source graphics software that allows Python integration, which makes it easy to automate processes.⁹⁸ An add-on developed by iraytrace and Simon Kirkby was used to import the G-code generated by Cura into Blender.⁹⁹ Note that this add-on only works for Blender versions 2.7.x, not for newer versions. Changes were made to this add-on to suit our purposes, as discussed in the methodology, including changing the cross-section profile and path generation technique. The amended code is available on the author's Github.¹¹⁹

A small change must be made for non-cyclic infills. Previously, the concentric option for infill pattern meant the start and end point of each path was the same. However, this may not be the case for all infill patterns. For example, a zigzag infill starts at one corner of the part and ends at the other corner, as shown in Figure 47(a). Using the same settings as the cyclic part would create an unwanted link between the start and end points, as seen in Figure 47(b), as the program attempts to close the loop. Simply unchecking the cyclic parameter does not fix the issue, as seen in Figure 47(c), since the ends become flared and the middle layers are missing a face at the ends. It is additionally necessary to decrease the order of the polynomial spline and add rectangular surfaces at the ends to cover the holes, as shown in Figure 47(d), to complete the optimized non-cyclic part.

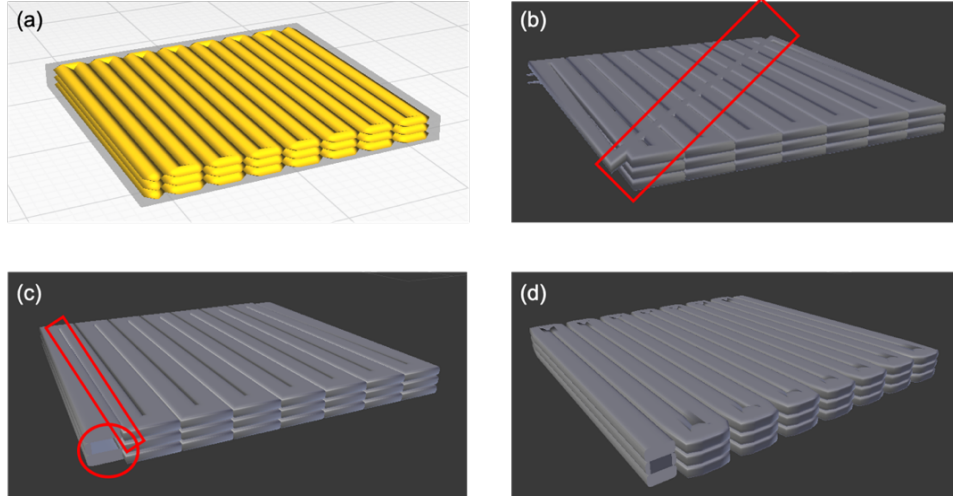


Figure 47: Non-cyclic part model generation. (a) Visualization in slicer software (Cura), (b) Blender rendering using previous settings, (c) Blender rendering without cyclic parameter, (d) Blender rendering with optimized settings.

9.2.1.4. *pvTrace*

pvTrace is an open-source ray-tracing software used to model luminescent materials. The original code was developed by Daniel Farrell¹⁰¹ and is available on his Github.¹²⁰ The code features a top-down architecture to isolate specific properties. The ray tracing occurs in a scene, which is a data structure consisting of several nodes. Each node can be designated as geometry or light. Within each geometry, general material properties such as refractive index can be defined, or more specific properties such as surface characteristics, absorption/scattering coefficients, and lumophores can be added. Each light source can be similarly tuned to have a certain direction, divergence, and wavelength spectrum. *pvTrace* then conducts ray tracing by tracking each generated ray through the defined geometries. A schematic of *pvTrace*'s code architecture is shown in Figure 48.

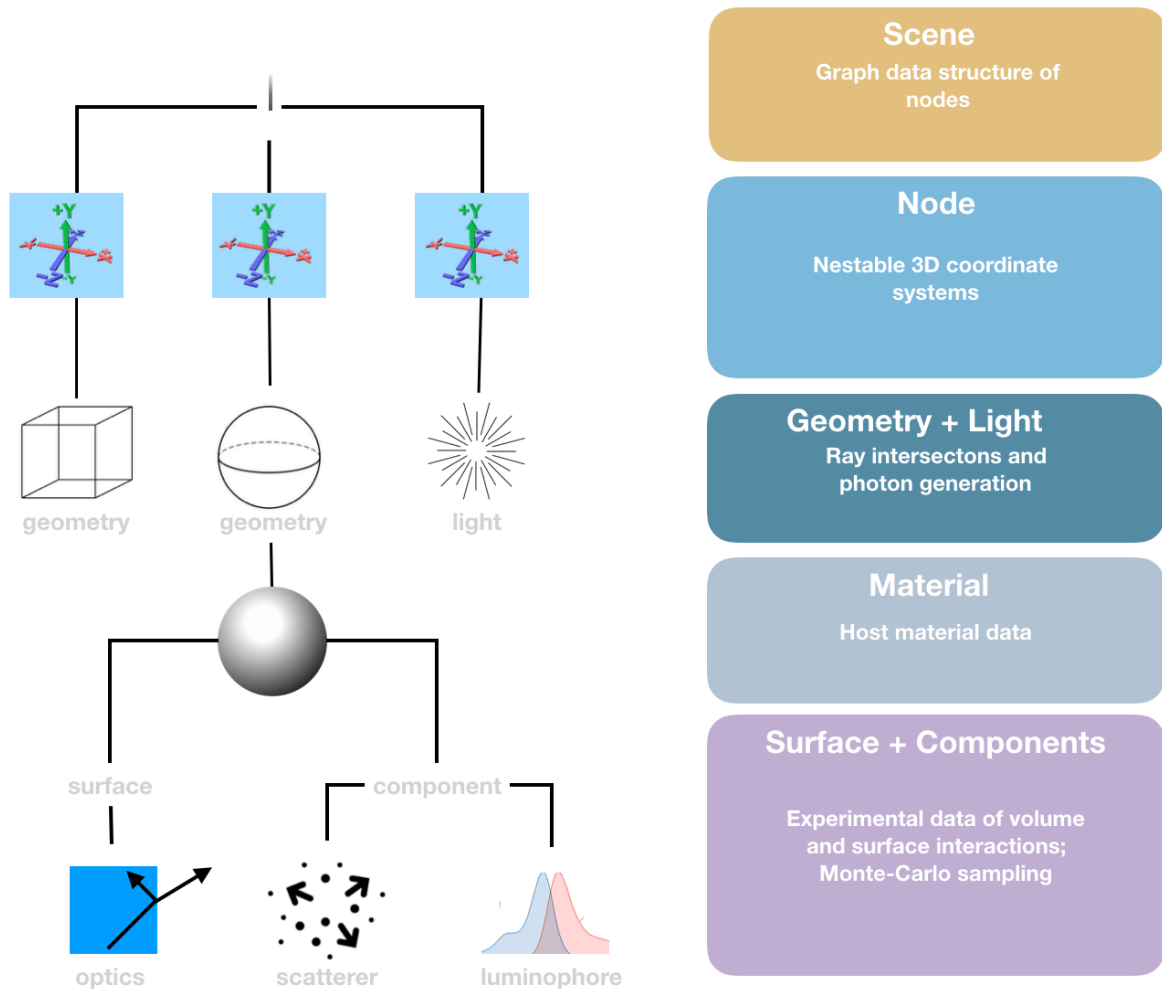


Figure 48: Code architecture of pvTrace, showing the top-down design. All objects exist within a scene, which contains nodes of geometry or light. General material properties such as refractive index can be defined for each geometry, or more specific properties such as surface characteristics, absorption/scattering, and emission can also be set. Reproduced from Farrell.¹²⁰

Once ray tracing is completed, the optical efficiency of objects can be calculated by counting exit *vs.* incident rays. Since it allows the import of STL files, the software is ideal for the purposes of this work. As discussed in Methodology, pvTrace was adapted for this study to accurately analyze non-conventional geometries. This was done by changing the edge emission measurement technique as well as including different types of masks. The increase in computational time resulting from the complicated alternative geometries was mitigated by use of parallelization. A GUI was also created to help non-computational

researchers to use the software. The final code used in this study including all of these modifications and additions is available on the author's Github.¹²¹

9.2.1.4.1. Inputs to pvTrace

For the absorption coefficient, note that a conversion is necessary: the UV-Vis absorption spectrometer will output absorbance A such that:

$$I(L) = I_0 \cdot 10^{-A}, \quad (8)$$

where $I(L)$ is the light intensity at path length L and I_0 is the initial light intensity. However, pvTrace requires absorption coefficient α such that:

$$I(L) = I_0 \cdot e^{-\alpha L}, \quad (9)$$

implying the α input to pvTrace can be calculated by:

$$\alpha = -\frac{\ln(10^{-A})}{L}. \quad (10)$$

To verify that the absorption coefficient was input correctly, it is possible to simulate ray transmission through a similar waveguide in pvTrace. Using a broadband spectrum incident on the top of a rectangular box, the number of rays exiting the box on the other side can be counted, and thus calculate transmittance over a range of wavelengths. Figure 49(a) shows a visualization of the ray tracing simulation, while Figure 49(b) shows the simulated results versus measured data. As seen, the simulation matches experimental data quite well, ensuring the absorption coefficient was properly defined.

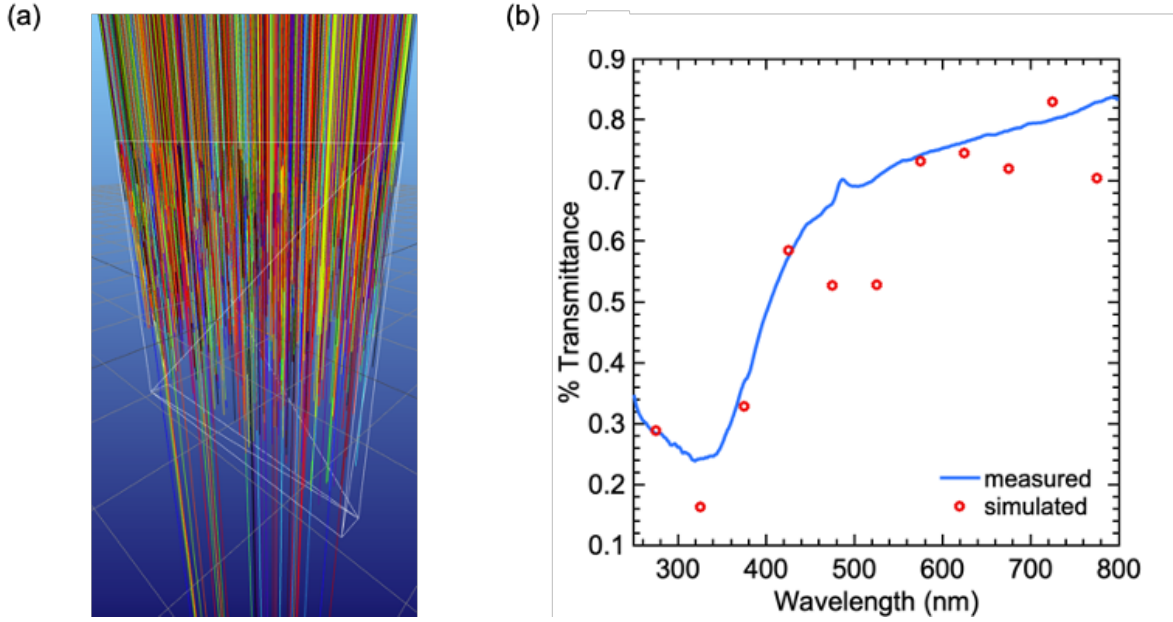


Figure 49: (a) Visualization of transmittance test featuring rectangular waveguide with broadband light spectrum incident on top, (b) transmission data for plain ABS waveguide comparing simulated results to measured data.

9.2.1.4.2. Experimental Verification of pvTrace Modifications

pvTrace v2.1.sv was compared against various literature studies of LSC efficiency to ensure the changes made to the code did not impact accuracy. This preliminary comparison was done with papers using LR305 embedded in a PMMA matrix in conventional bulk rectangular LSCs. The specific inputs taken from each study are specified in Section 4.2.4. Note that all references to optical efficiency in this section correspond to external optical efficiency (η_{ext}) as defined in Section 2.1.2.

The first study chosen was a 2012 paper by Desmet *et al.* which is consistently cited in literature as a useful benchmark for a standard LSC.⁴³ They used a $5 \times 5 \times 0.5$ cm LSC with 115 ppm LR305 in PMMA, a Halogen lamp solar simulator as well as the actual sun (two separate cases) as the light source, and silicon solar cells with 16.2% power conversion efficiency to measure the edge output. They do not report the background parasitic absorption of the PMMA waveguide, so a value of 0.3 cm^{-1} was set as a baseline.

Table 7 shows the results of simulation compared to reported values for external photon efficiency (η_{ext}). As seen, although the results do not match exactly, they are fairly close. The first row (light range 400-900 nm) was experimentally measured using a solar simulator which had very little UV radiation, while the second row of (light range 300-900 nm) was measured using outdoor sunlight which had some UV radiation. In pvTrace, the NREL AM1.5G spectrum was used for both cases, with the boundaries adjusted to match the reported range.

The inclusion of UV radiation explains the increase in efficiency in both simulation and experimental values, since LR305 has strong absorption in the UV region. However, the increase in the optical efficiency determined by simulation is not as drastic as experiment. This could be due to a number of factors including differences in the incident solar spectrum, variations in the optical characteristics of LR305, or differences in the background absorption of the waveguide.

Table 7: pvTrace comparison to Desmet *et al.* using a $5 \times 5 \times 0.5$ cm rectangular LSC.⁴³ Optical efficiency roughly matches for 10,000 simulated rays. Note the increase in efficiency when light range is extended to include the UV region, and a similar increase reported in literature.

Light Range (nm)	Num. Rays	pvTrace v2.1.sv η_{ext}	Desmet <i>et al.</i> η_{ext}
400-900	10,000	13.15%	14.2%
300-900	10,000	14.71%	19.0%

A second work used for comparison is a 2016 paper by Zetzl *et al.*, in which they compared several polymers as host materials for LSCs.³¹ They used $6 \times 6 \times 0.32$ cm LSCs with 200 and 500 ppm LR305 in PMMA, a Xenon lamp solar simulator as the light source, and a fiber optic cable attached to one edge of the LSC for edge emission measurement.

This study also included absorbance values for the bare waveguide as a measurement of parasitic absorption.

Table 8 summarizes the comparison between pvTrace v2.1.sv (10,000 rays) and Zetl *et al.* The third column shows the results using a broadband parasitic absorption of 0.525 cm^{-1} , as reported in the study, while the fourth column shows the results using a background parasitic absorption of 0.3 cm^{-1} , as used in the baseline comparison with Desmet *et al.*, which matches much better with the experimental results. The results in the third column might be lower than expected due to the edge emission measurement technique utilized by Zetl *et al.* They used a $20 \text{ }\mu\text{m}$ fiber optic cable placed at the center of one of the edges, which would overestimate optical efficiency since edge emission at the center of the LSC is typically higher than the edges.¹²² Regardless, we again see fairly well-matched results between simulation and experiment.

Table 8: pvTrace comparison to Zetl *et al.* using a $6 \times 6 \times 0.32 \text{ cm}$ rectangular LSC.³¹ Shows fairly consistent results. Decrease in parasitic absorption compared to reported values resulted in higher accuracy simulation.

LR305 ppm	Num. Rays	pvTrace v2.1.sv η_{ext} (0.53 cm^{-1})	pvTrace v2.1.sv η_{ext} (0.3 cm^{-1})	Zetl <i>et al.</i> η_{ext}
200	10,000	6.2%	7.6%	7.5%
500	10,000	7.4%	8.8%	8.9%

The third paper was a 2009 study by Debije *et al.* investigating the effects of a scattering layer on edge output.⁵⁸ The base case of this study had no backscattering layer, and this configuration was used for comparison, though the other two cases (backscatterer directly attached *vs.* at a small distance) could also be compared in future studies. They used a $5 \times 5 \times 0.3 \text{ cm}$ LSC with LR305 concentrations ranging from 10 to 400 ppm, poly(carbonate) as the waveguide, a solar simulator, and integrating sphere for edge

emission measurement. Again, no spectrum for the background absorption of the waveguide was provided, so a broadband value of 0.3 cm^{-1} was used.

Table 9 shows the results of this comparison. As seen, the efficiency at a lumophore concentration of 130 ppm matches well, while the efficiency overshoots when increased to 382 ppm. This could be due to known issues associated with the use of LR305 at high concentration, including aggregation-induced quenching or increasing instances of nonradiative relaxation which reduce the PLQY.¹⁶ However, the general trend is again upheld.

Table 9: pvTrace results compared to Debije et al. using a $5 \times 5 \times 0.3 \text{ cm}$ rectangular LSC.⁵⁸ Shows strong match at 130 ppm, but increase to 382 ppm overshoots experimental efficiency. Likely due to various issues with high-concentration LR305 such as aggregation.

LR305 ppm	Num. Rays	pvTrace v2.1.sv η_{ext}	Debije et al. η_{ext}
130	10,000	7.11%	7.2%
382	10,000	10.1%	8.5%

A final comparison returns back to some of the original publications of pvTrace and its comparison to experimental values.¹⁰² All useful inputs to pvTrace are measured and reported, making the comparison between experiment and simulation much easier. The LSC dimensions were $5 \times 5 \times 0.3 \text{ cm}$ with 50 and 150 ppm LR305 in PMMA (background absorption $\sim 0.02 \text{ cm}^{-1}$), a solar simulator as the light source, and solar cells for edge emission measurement.

Table 10 shows the simulated *vs.* experimental results. This time, the results match quite well, with an almost equivalent increase in efficiency from 49 ppm to 161 ppm. The small discrepancies can once more be attributed to the lack of complete reporting of background absorption (a single value was given for the entire spectrum). By fine-tuning

the absorption coefficient and adding wavelength dependence, it is likely that a closer match may be obtained.

Table 10: *pvTrace* comparison to Bose *et al.* using $5 \times 5 \times 0.3$ cm rectangular LSC.¹⁰² Shows good agreement between simulated and experimental values.

LR305 ppm	Num. Rays	<i>pvTrace</i> v2.1.sv η_{ext}	Bose <i>et al.</i> η_{ext}
49	10,000	17.24%	19.44%
161	10,000	32.18%	38.64%

Thus, extensive comparison has proven that the modified version of *pvTrace* developed in this work, *i.e.* *pvTrace* v2.1.sv, retains its accuracy when compared to experimental results. Note that all of the above studies used conventional rectangular LSCs. An area of future work would be to compare simulated results to alternative LSC geometries reported in literature, though this may be more difficult due to the vastly different edge emission techniques employed in each study.

9.2.1.4.3. *pvTrace* GUI

Figure 22 shows a screenshot of the GUI developed in this work¹⁰⁷ and the various inputs required for the simulation. First, the user must create an LSC. The GUI gives the option of adding up to 3 LSCs which will be created one top of one another. The geometry of the LSC can be a Box, Cylinder, Sphere, or users can also import their own STL files. The dimensions (automatically updated for imported STL files) must be provided as well as any additions to the LSC including solar cell edges or a scattering/mirroring bottom surface. The lumophore must then be selected – either LR305, which is built in, or an import of another lumophore. The concentration of the lumophore must also be specified, along with the background absorption of the waveguide.

Next, the light pattern is selected. Rectangular masks are the default, though a circular mask or a point source may also be used. The dimensions of the light should already be updated to match the size of the LSC. The wavelength range and divergence of the light source should also be input.

Third, the ray-tracing parameters must be set. The maximum number of rays for the simulation and the convergence threshold are used to determine how long the simulation will run. The wavelength range is primarily used to calculate the lumophore spectra from a polynomial fit of the input data, to ensure the absorption/emission is 0 beyond the bounds of the lumophore. An enclosing box can be used if an alternative method for ray counting is desired. Checking either the convergence plot or show simulation boxes will display either as requested.

Finally, it is possible to easily save results. One can choose a folder location and file name to save the results, as well the resolution of the figures. It is also possible to save the inputs in a file or load an input file for ease of repeating simulations.

Note that from this point forward all references to “optical efficiency” refer to external photon efficiency (η_{ext}) as defined in Section 2.1.2 unless specified otherwise. The simulation will return the overall optical efficiency as well as the optical efficiency at each edge of the device (of course, for alternative geometries the efficiencies at the 4 cardinal directions have little meaning). The program will also output five plots, as shown in Figure 50. Figure 50(a) shows the optical efficiency as the program runs and generates additional rays. This is useful for the user to know if the optical efficiency changes significantly while the program is running or if it is generally stable. Figure 50(b) shows the convergence plot of the optical efficiency. This compares each new optical efficiency value with the average of all previous values, and then plots the difference. If the convergence value reaches below the threshold, the simulation is said to converge, and

the simulation automatically stops. Figure 50(c) shows the distribution of entrance wavelengths on top of the input spectrum used, to prove that they match. Figure 50(d) shows the distribution of exit wavelengths along with the absorption and emission spectra of the lumophore. This is useful to visualize any reabsorption losses caused by the dye, and to ensure the lumophore optical properties were incorporated accurately. Finally, Figure 50(e) shows the x - and y - positions of the entrance and exit rays, which is a useful qualitative visualization of efficiency (*e.g.* note the red dots on the edges of the device) and to ensure the object was detected properly.

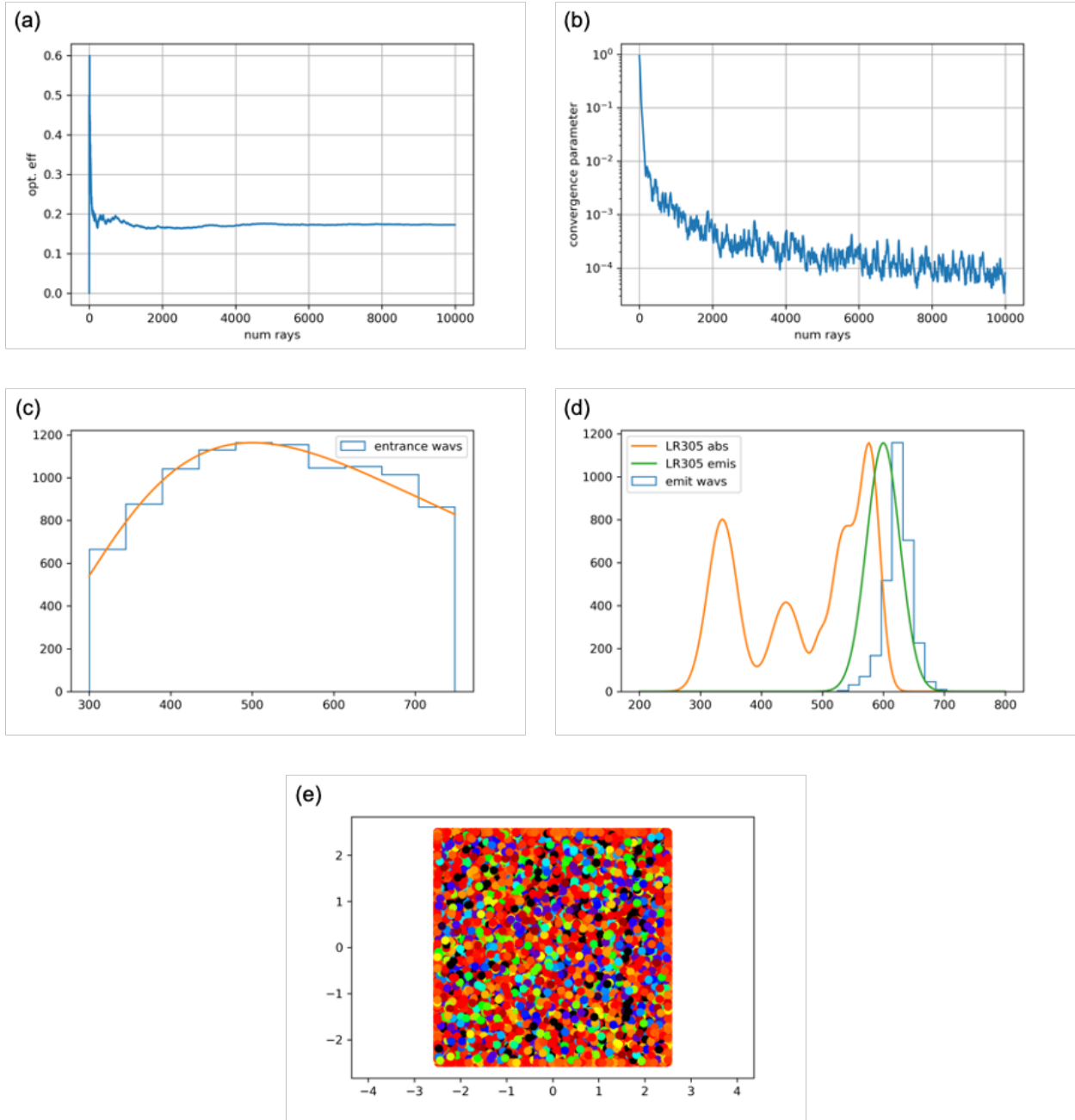


Figure 50: Various figure outputs of pvTrace GUI. (a) Optical efficiency as the simulation generates more rays, (b) convergence of optical efficiency towards a final value, (c) wavelength of generated entrance rays versus the input spectrum, (d) wavelength of exit rays versus the absorption/emission spectra of the lumophore, and (e) x- and y-positions of the entrance and exit rays.

9.2.1.4.4. *pvTrace* parallelization

A simulation consisting of a bulk cylindrical (6 cm diameter, 0.32 cm height) LSC with a rectangular mask of light incident was chosen to test runtime. To test the compile time of serial (non-parallelized, using only 1 computing core) *pvTrace*, ten simulations were done with both 1,000 and 10,000 rays, and the average completion time was recorded. Figure 51(a) (blue bars) shows completion time for serialized *pvTrace*, averaging 10 runs of 1,000 or 10,000 rays. As expected, we see an approximately ten times increase in completion time since there are ten times as many rays. For 10,000 rays, while 100 s running time is not prohibitively high, the runtime increases drastically for more complex parts. Recall that for this speedup analysis, a simple cylindrical LSC was used. For more complex LSCs, such as STLs with several surfaces, the runtime can be as much as 10 times longer, motivating the need for parallelization.

An easy way to reduce computation time is to parallelize *pvTrace* just using the cores available on a PC/Mac, since most laptops and desktops have multiple cores. For example, the 2017 MacBook Pro used to write this thesis has 2 cores. It is possible to implement the multiprocessing package in Python to take advantage of these additional cores. This package creates a pool of all available cores and distributes tasks amongst them in the most efficient way possible, which typically means the rays are evenly distributed amongst the cores. On a laptop with 2 cores, therefore, we would expect a 2x improvement in computation time. Figure 51(a) (orange bars) show the results of running *pvTrace* while implementing a multiprocessing pool of the 2 cores available on the 2017 MacBook Pro, with completion time averaged over 10 runs. As expected, the completion time when running on 2 cores is approximately half that of running serialized *pvTrace*.

While simply parallelizing on a personal machine is the most accessible option for speeding up *pvTrace*, it is also possible to run the code on a computing cluster. Clusters

typically have several nodes, and each node has multiple CPUs or cores. In the Cambridge Service for Data-Driven Discovery (CSD3) cluster,¹²³ each node has 16 cores, so accelerated completion time is expected compared to a 2-core laptop. Figure 51(b) shows the results of running 10,000 rays in parallelized pvTrace on the Cambridge computing cluster,¹²³ running on a single node with a multiprocessing pool of 1, 2, or 16 cores, averaged over 10 runs. It is qualitatively clear that doubling the number of cores halves the computation time, while increasing to 16 cores reduces time 16-fold. To more quantitatively prove this, Figure 51(c) shows a log-log plot of runtime vs. number of cores, including 4 and 8 cores as well, with a power curve fit plotted as well.

To gain access to more cores and reduce runtime further, it is necessary to switch the Python package used for parallelization, since multiprocessing only supports single-node computation. Instead of multiprocessing, Ray was used for distributed computation. It allows programmers to use the same syntax as multiprocessing, still creating a pool of cores, but is able to handle communication between nodes. Figure 51(d) shows completion time for pvTrace using the Ray pool, 100,000 rays, and an increasing number of cores. Figure 51(e) shows the same data in a log-log plot. While the data is initially linear in log-log, indicating a power curve fit, the relationship breaks down as cores are increased further, following an exponential decay instead, as computation time reaches a minimum. This is likely due to the overhead created by initializing pvTrace and the Ray package, establishing a minimum runtime.

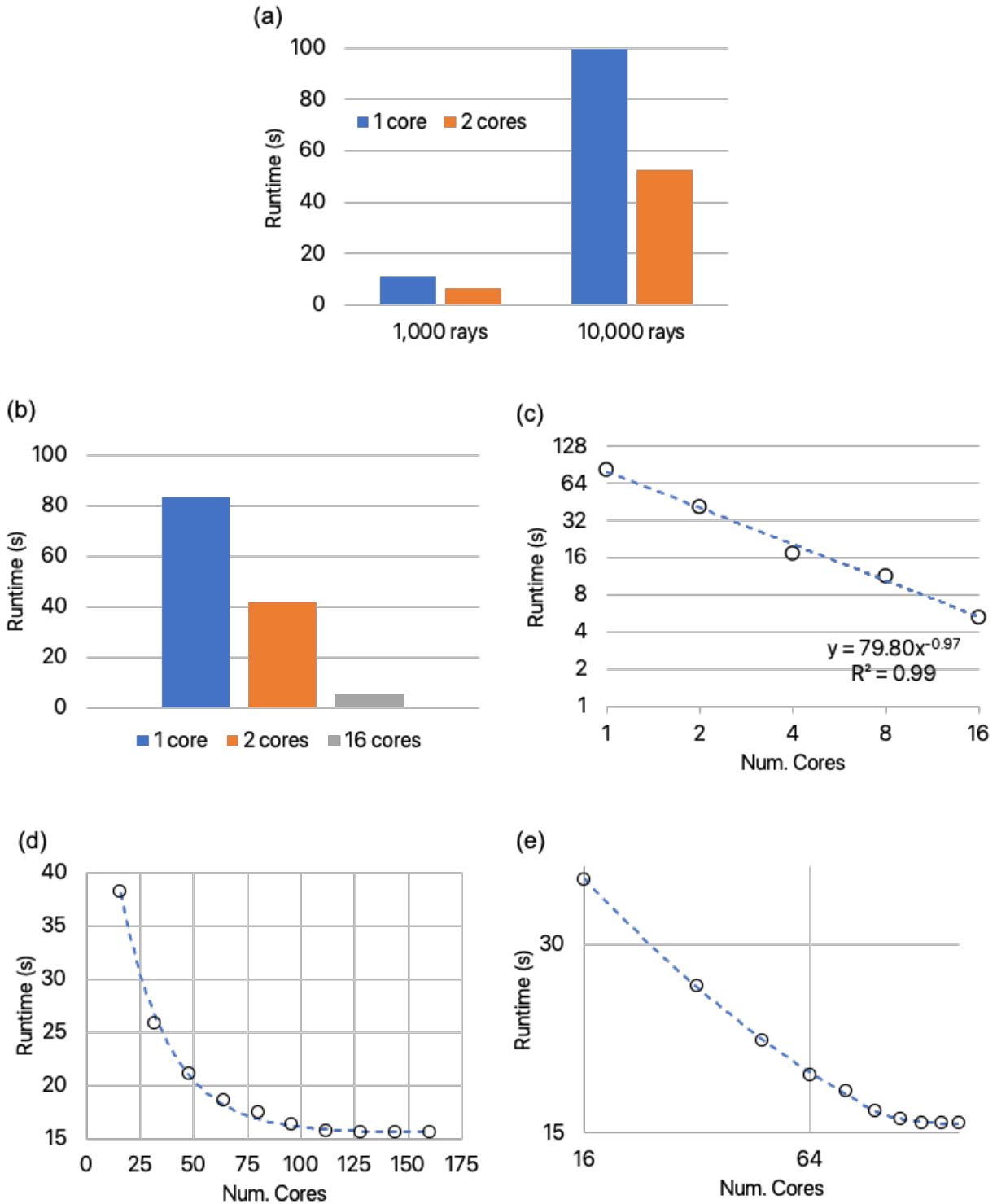


Figure 51: Various plots of runtimes for *pvTrace v2.1.sv* simulating a circular LSC with 6 cm diameter, 0.32 cm height and rectangular light mask. (a) Completion time of *pvTrace* script for 1,000 and 10,000 rays run on a laptop, using either serial (non-parallel, 1 core) configuration or the 2 cores available. (b) Runtime for parallelized *pvTrace* on a single node in the CSD3 cluster, for various numbers of cores. (c) same as (b) but on a log-log plot and including 4 and 8 cores. (d) Runtime for parallelized *pvTrace* on multiple nodes in the CSD3 cluster. Implements the Ray package

for distributed computing across various nodes. Increasing cores decreases runtime to a certain extent, but overhead from various python packages increases minimum runtime. (e) same as (d) but on a log-log plot.

9.2.1.5. Cambridge Computing Cluster

The Cambridge Peta4 supercomputer offered as part of the Cambridge Service for Data-Driven Discovery (CSD3) was used this work.¹²³ The Skylake nodes offer 1 core with 6 GB of memory per task, and multiple cores can be requested per node, up to a maximum of 16 (physical) cores. Service Level 3 allowed a maximum of 200,000 core-hours for this project and a maximum per-job limit of 320 cores.

9.2.2. Materials

The materials used for luminescent filament preparation are detailed below.

PMMA was obtained from Alfa Aesar (550 kDa), Sigma Aldrich (120 kDa) and Fisher Scientific (35 kDa). Lumogen F Red 305 (LR305) was gifted by BASF. Poly(ethylene glycol) (PEG) was obtained from Sigma Aldrich. Poly(lactic acid) and poly(acrylonitrile-*co*-butadiene-*co*-styrene) (ABS) filaments (both diameter, $d = 1.75$ mm) were purchased from Verbatim. Poly(ethylene terephthalate glycol) filament ($d = 2.85$ mm) was purchased from Filamentive. Additionally, chloroform (>99.8%) was used as the solvent and was obtained from Fisher Scientific.

4-aminobenzoic acid (>99%), 3,4,9,10-perylenetetracarboxylic dianhydride (perylene dianhydride, PTCDA) (>98%), iodine (I_2) (>99.5%), chlorosulfuric acid ($HClSO_3$) (>97%), propionic acid (>95%), phenol (>99%), N-methyl-2-pyrrolidinone (NMP) (>99%), and chloroform ($CHCl_3$) (>99.8%) were purchased from Fisher Scientific. 4-(dimethylamino)pyridine (DMAP) (>99%) and potassium carbonate (K_2CO_3) (>99%) were purchased from Alfa Aesar. 2-hydroxyethyl methacrylate (HEMA) (>97%) was

purchased from Sigma Aldrich. 1-(3-dimethylaminopropyl)-3-ethylcarbodiimide HCl (EDC.HCl) (>98%) was purchased from Carbosynth.

All materials were used as received. The experimental procedure for combining or reacting the materials is provided in each section below, separated by the three techniques discussed for filament preparation, physical mixing, solvent casting, and Lumogen functionalization.

9.2.2.1. Physical mixing

The desired mass of PMMA (typically 10-100 g) was weighed into a beaker using a Technical Balance from Denver Instrument. Then, the mass of LR305 based on the desired weight percent (typically 0.01 wt%) was calculated and weighed into a small vial using an Analytical Balance from Fisher Scientific. The mass of LR305 within the small vial was then tipped into the beaker. The PMMA and LR305 mixture was stirred, breaking the clumps of LR305, until all of the PMMA was dyed a pinkish hue.

9.2.2.2. Solvent casting

In this method, PMMA and LR305 were first separately dissolved in chloroform, before mixing the solutions to achieve the required wt% of LR305 solution, as shown in Figure 52(a) and (b). The mixed solution was transferred to an evaporating basin and left in the fume hood (partially covered to limit air flow effects while also allowing solvent to escape) to evaporate, as shown in Figure 52(c). The full procedure is described below.

The weighing procedures for PMMA, PEG, and LR305 are identical to Section 9.2.2.1. After measuring out the desired mass of PMMA powder, this was deposited in a round-bottom flask. Then, enough chloroform was added to have a 20% m/v (g/mL) ratio of PMMA to chloroform. The round-bottom flask was placed above a stir plate and a

mixing rod was used to mix the PMMA powder with the chloroform until it was fully dissolved, usually after 3-4 hours.

In a separate vial, the desired concentration of LR305 (usually 0.01 wt%) was added, along with a few mL of chloroform. The LR305 easily dissolved in chloroform and did not require significant mixing.

Once both powders were dissolved, the LR305 solution was added to the polymer solution in the round-bottom flask and the solutions were mixed for a few minutes (exposed to air, no need for an inert atmosphere), until the resulting solution was homogeneously red. Then, the solution was transferred to an evaporating disk that was covered with a funnel to limit air flow effects while still allowing solvent to evaporate. The solution was left for 48 hours or until it became solid to touch.

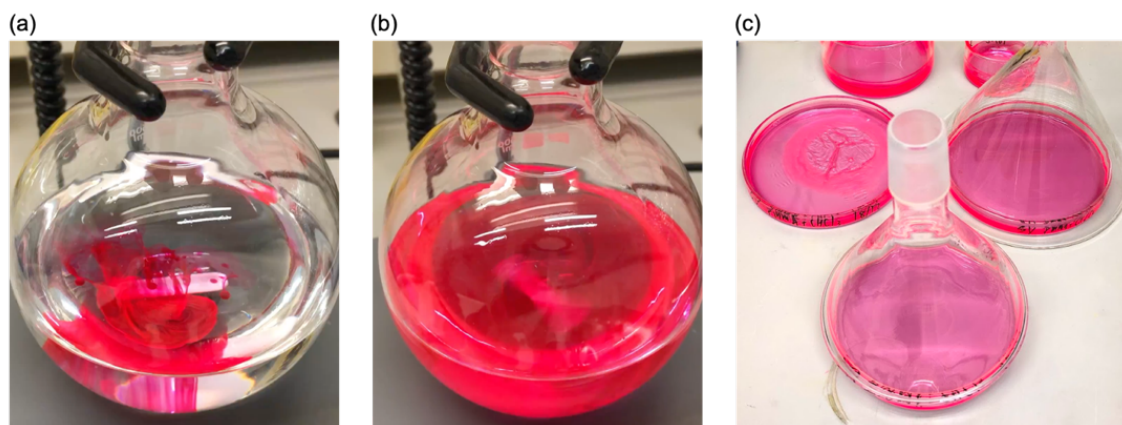


Figure 52: (a) Before and (b) after pictures for PMMA and LR305 solution mixing. PMMA is first fully dissolved in a round-bottom flask (usually around 3-4 hours), then LR305 solution is added. An evenly distributed mixture is obtained after a few seconds of mixing, but the sample is allowed to mix for few minutes to ensure completion. (c) After mixing, the solution is transferred to a partially covered evaporating basin for at least 48 hours.

This process is fairly standard and is flexible to allow for additions or modifications if required. For example, PMMA need not be used. Several commercially available transparent filaments exist, primarily made of poly(acrylonitrile-*co*-butadiene-*co*-styrene) (ABS), poly(lactic acid) (PLA), or glycol-modified poly(ethylene terephthalate) (PETG). All of these were tested for compatibility with solvent casting in chloroform and all gave

good results, as shown in Figure 53, although doped PLA and ABS were cloudier than PMMA. The procedure for dissolving the various types of filament (PLA, PETG, ABS) is identical to PMMA, but first the filament was chopped to small pieces to increase the surface area. This enables comparison between non-luminescent transparent filament and filament doped with LR305, which allows waveguide absorption and scattering analysis.

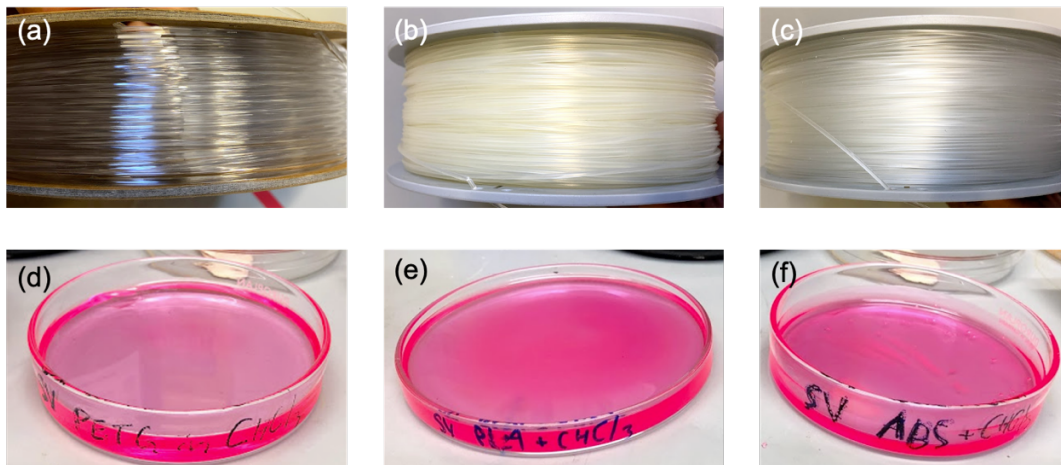


Figure 53: Solvent casting of commercial 3D printing filament with LR305 solution added. (a) PETG, (b) PLA, and (c) ABS filament purchased and cut into pellets which were then dissolved in chloroform. After addition of LR305 solution and mixing in a round-bottom flask, the contents were poured into evaporating basins, as shown in (d), (e), and (f).

9.2.2.3. Lumogen Functionalization

Through this technique, a methacrylate group is grafted to the head and tail of the LR305 molecule. Then, polymerization can occur with an MA monomer solution containing functionalized LR305 in the desired wt%, such that the MMA group on the LR305 becomes part of the polymer chain, creating a PMMA polymer with evenly distributed LR305. Note that there are two MA groups grafted to each LR305 molecule, implying that the functionalized LR305 would cause crosslinking in the PMMA produced. However, since the modified LR305 is added in such low concentration, this crosslinking is likely negligible. Figure 54 shows the structure of a functionalized LR305.

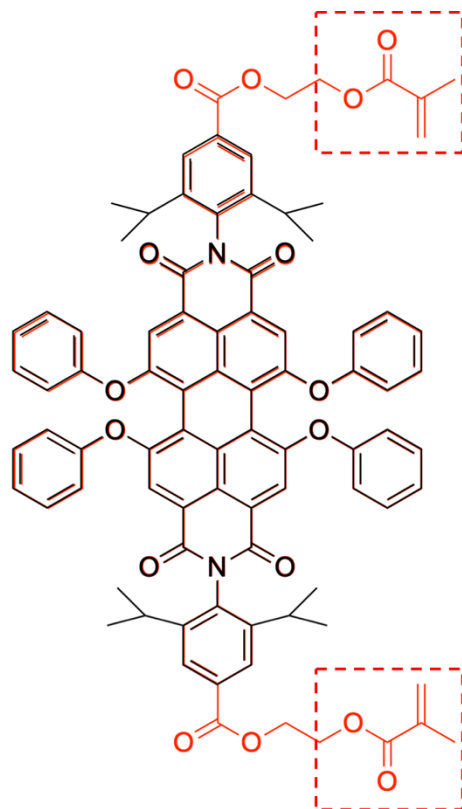


Figure 54: Chemical structure of functionalized LR305 with MMA groups outlined in red.

The scheme for Lumogen 305 functionalization is shown in Figure 55.

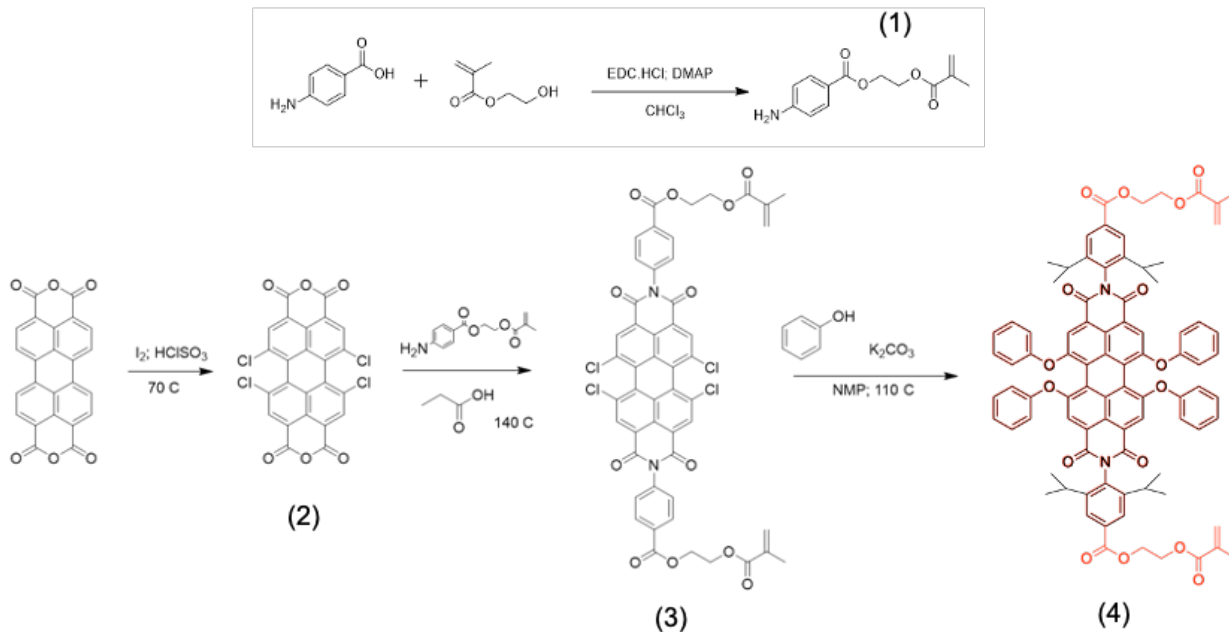


Figure 55: Scheme for synthesis of functionalized LR305. Due to the configuration of commercial LR305, the MMA group cannot be directly grafted. Instead, we must build LR305 from the precursor molecules in-house, adding the MMA group during the process. The final molecule shows the commercially-available LR305 in black and the functionalized LR305 in red.

Synthesis of product 1: 4-aminobenzoic acid (10.0 g, 72.92 mmol) and 4-(dimethylamino)pyridine (1.34 g; 10.94 mmol; 0.15 eq.) were added to a dried flask, and the atmosphere was exchanged for nitrogen *via* repeated evacuation/refill cycles before the addition of chloroform (100 mL) and 2-hydroxyethyl methacrylate (10.62 mL; 87.50 mmol). The reaction was stirred, cooled to 0°C, and the cooling was maintained during the slow addition of N-(3-dimethylaminopropyl)-N'-ethylcarbodiimide hydrochloride (16.77 g; 87.50 mmol) dissolved in chloroform (100 mL) through Cannula transfer under a nitrogen atmosphere. The reaction was sealed under a nitrogen atmosphere and stirred at room temperature overnight. The reaction was then transferred to a separating funnel and washed sequentially with deionized water (3°× 150 mL) and saturated brine (1°× 150 mL). The chloroform layer was isolated, dried over anhydrous magnesium sulphate, filtered, and the solvent removed under reduced pressure.

Synthesis of product 2: reacting 3,4,9,10-perylenetetracarboxylic dianhydride (perylene dianhydride, PTCDA) with iodine (I_2) and chlorosulfuric acid ($HCISO_3$) at elevated temperature ($70\text{ }^\circ\text{C}$) to chlorinate the perylene precursor. This allows the phenols to attach to the sides of the perylene base in product 4.

Synthesis of product 3: reacting the chlorinated perylene with the MAEAB in the presence of propionic acid at elevated temperatures ($140\text{ }^\circ\text{C}$). This grafts the MAEAB to the top of the perylene base.

Finally, synthesis of product 4: reacting product 3 with phenol and potassium carbonate (K_2CO_3) in the presence of 1-methyl-2-pyrrolidinone (NMP) at elevated temperature ($110\text{ }^\circ\text{C}$) to produce our final functionalized LR305.

9.2.3. Instrumentation

The instrumentation for steps 3, 4, and 5 (luminescent filament generation, 3D printing, optical characterization) of this study are listed below.

9.2.3.1. Coffee grinder

For physical mixing of lumophore and polymer, this instrument is not needed. However, for both solvent casting and lumophore functionalization, the result of the incorporation step is a solid bulk polymer. In order to reshape this into a filament, it is first necessary to grind the bulk polymer to a powder. Figure 56(a,b) show the top and side views, respectively, of the resulting polymer bulk from solvent casting after solidification and removal from the evaporating disk. Figure 56(c,d) show the before and after pictures of grinding the bulk polymer into a powder using a commercial coffee grinder.

While using a coffee grinder is one option to break up the bulk polymer, simply cutting the bulk polymer with scissors also works. The pellets generated are naturally much larger, and using scissors is more time consuming. For this work, therefore, the coffee grinder was primarily used.

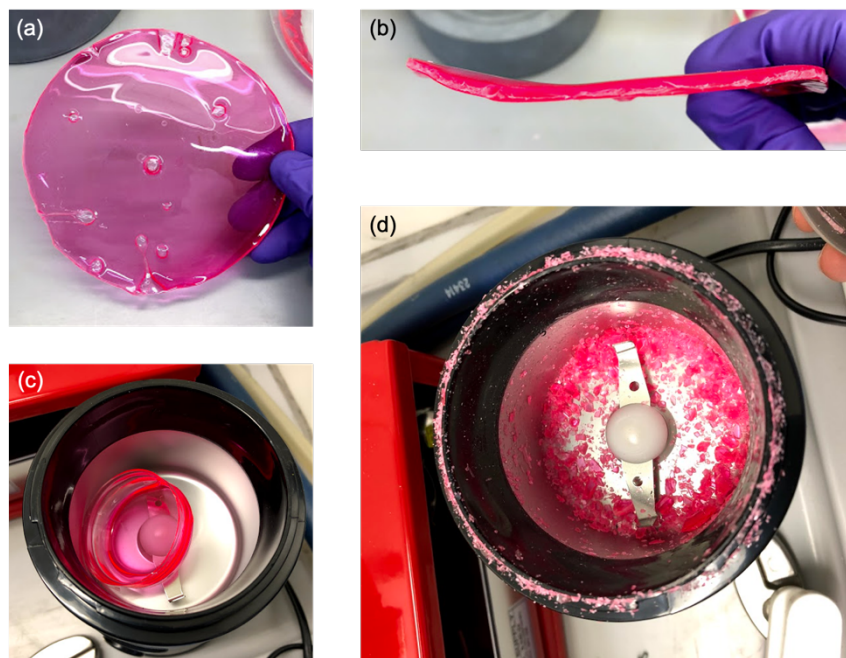


Figure 56: Results from solvent casting and generation of luminescent powder. (a) Top view of bulk polymer after solvent casting, (b) side view, (c) polymer inside coffee grinder before powder generation, (d) luminescent powder after grinding bulk polymer.

Two models of commercially available coffee grinders were used in this study. A 150 W, 50 g version was purchased from Kitchen Perfected. However, the metal blades within the grinder degraded quickly, within a dozen uses of generating powdered PMMA. A 120 W, 80 g version was also purchased from Kitchen Perfected, and it performed better than the previous version for powder generation.

After solvent casting was completed, the bulk solid PMMA slab doped with LR305 was placed inside the grinder. The grinder was pulsed on and off with a frequency of 1s

for about 10s. This was to ensure the powder generated was not too fine, but all of the bulk was still converted to powder.

9.2.3.2. Extruder

As discussed in Section 4.3.2, PMMA powder of various molecular weights (MW) were extruded. Figure 57 shows the results of the extrusion process.

All of these filaments were processed at 180°C. Qualitatively, there was no impact of MW on extrusion, since all three weights resulted in transparent, smooth filament at the same temperature. 120 kDa PMMA was used for the remainder of this study due solely to the larger size of the pellets and therefore greater compatibility with the extruder used. Note that the slightly reddish hue in the PMMA was due to residual LR305 from previous operation. In future runs, a batch of poly(propylene) was used in between runs to cleanse the barrel of impurities.

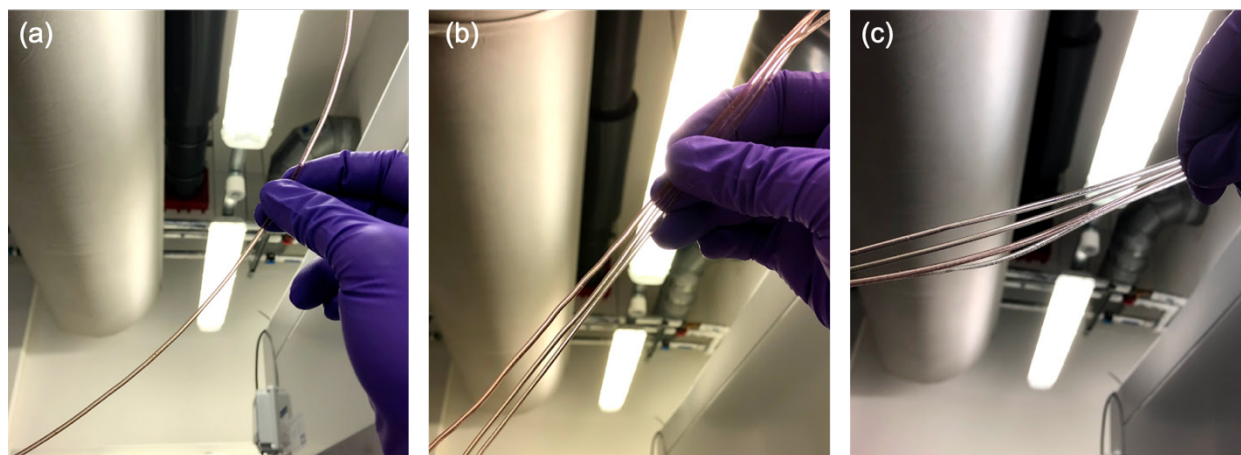


Figure 57: Pictures of plain PMMA extruded filament of various MW. (a) 550 kDa MW PMMA, (b) 120 kDa MW PMMA, and (c) 35 kDa MW PMMA. Note qualitatively the optical transparency of the extruded filament, regardless of the MW used, as well as the relative thickness of the filament (~2.0 mm).

Figure 58 shows the first attempt at extruding luminescent filament. While the lumophore has clearly been incorporated well, the filament has many issues. Specifically,

the surface of the extruded filament is uneven. Running at the same processing temperature of 180°C, transitioning from pure PMMA to PMMA with LR305 powder resulted in filament created from the mixture to be bumpy. The diameter of the filament ranges from 2.0 mm to 2.2 mm. This unevenness could be caused by the higher viscosity created by LR305 particles suspended in PMMA. This would suggest a higher operating temperature would be better.

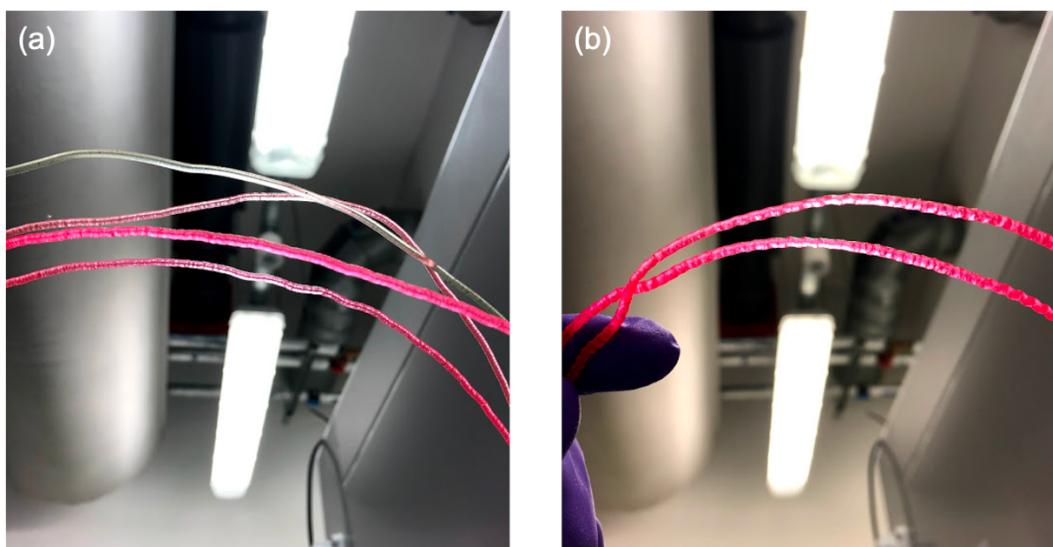


Figure 58: Pictures of extruded luminescent filament composed of PMMA doped with 0.01 wt% LR305 dye. (a) Showing the transition between plain PMMA and PMMA+LR305 as the extruder takes in lumophore-incorporated pellets. (b) uniform pieces of PMMA+LR305 filament.

The Noztek Pro Filament Extruder was used for this study.¹¹⁰ The Noztek Pro is a desktop screw-based extruder. It consists of a hopper where material can be filled, a barrel screw powered by a motor, a pre-heating band, a heating band, and a swappable die nozzle. The procedure for extrusion is detailed below.

The extruder is set at the desired temperature (for PMMA/PMMA+LR305 between 180 and 210 °C) and allowed to stabilize for 1 – 1.5 hours. This ensures the entire length of the extruder is at this high temperature.

The motor is turned on once the temperature has stabilized to make sure no material is jammed from previous operation. If the barrel is jammed, the temperature is

set higher and the process is repeated. Once the barrel jam is cleared, the temperature is reduced to the desired setpoint, and the barrel is checked once again. If it turns without resistance, it is ready.

Powder is added to the hopper. The level of the powder should be high enough so that the powder exerts pressure on the bottom, forcing itself into the extruder. Additional weight may need to be applied by the user if the level is low.

After 5-10 minutes (allowing the heat to penetrate into the layer of powder), the motor can be turned on and filament produced. The first few strands may be slightly bubbly, but after 2-3 minutes of operation the filament produced should be smooth.

9.2.3.3. 3D printer

The Original Prusa i3 MK3S¹¹¹ kit was purchased from Prusa Research and assembled in-house according to instructions – no extensive modifications were made. Ultimaker Cura with the Prusa driver installed (see Section 9.2.1.2) was used for the 3D printing software. The specific printing parameters were already set when generating the STL based on the G-code and were not changed.

Before printing the part, the surface was wiped with acetone wipes to eliminate any contaminants on the surface. The extruding nozzle was also cleaned between prints. The actual 3D printing of the part was completely handled by the G-code generated by Cura, with the settings set by the user. Post-printing, the part was allowed to cool for 5-10 minutes, ensuring the part solidifies completely and preventing flexure by any post-processing. The Prusa MK3S comes with a removable base, allowing easy removal of parts. The base was removed from the 3D printed and then flexed until the part detached.

9.2.3.4. *Laser Cutter*

The LaserScript LS3060 laser cutter¹²⁴ was used to fabricate bulk parts, including the box, circle, hexagon, and triangle geometries mentioned in Section 5.4. 3.8 mm LR305 stock was provided by Prof. Michael Debijs and was first milled down to 1.6 mm by the Department of Materials Science Mechanical Workshop. The laser cutter was then used at 20 mm/s speed and 100% power to cut through the 1.6 mm PMMA+LR305 stock.

9.2.3.5. *UV/Vis spectrometer*

The Perkin Elmer Lambda 750 UV/Vis spectrometer was used for static absorbance measurements. Measurements were carried out using a solid-state sample holder with a path length of approx. 2 cm and measured against air as reference. A broadband wavelength spectrum of 250 to 800 nm was used to obtain data across the entire active spectrum of LR305. A slit width of 2 mm was used. This allowed for enough averaging across the width of the sample to correct for any variations in LR305 concentration. The absorbance was measured at various locations of parts where possible to ensure the values were equivalent. The resolution of the wavelength scan was 1 cm⁻¹.

9.2.3.6. *Solar simulator*

An Abet Technologies Class ABB solar simulator was used as the light source for optical efficiency measurements. It was fitted with an AM1.5G filter to mimic the spectrum of actual sunlight. The height of the solar simulator above the sample was first calibrated using a reference solar cell of known efficiency coupled to a Keithley 2401 Sourcemeter such that the intensity of light on the sample is 1000±10 W/m². The measured spectrum of incident light from the solar simulator is shown in Section 4.2.2,

Figure 19 and is compared against a reference AM1.5G spectrum provided by NREL and against a spectrum of a blackbody at 5800 K.

9.2.3.7. Laser scattering setup

Figure 59(a) shows the near-IR laser with the mount designed to position the laser directly above the LSC, pointing downwards. The position of the laser is calibrated using a 3D printed mask, which can rotate about a central axis, as shown in Figure 59(b). This thus allows precise and consistent positioning of the laser on the LSC. As in the previous experimental setup, the edge of the LSC is placed on the side of the integrating sphere. This setup allows the user to measure scattering as a function of laser distance from the edge, providing greater detail about the scattering characteristics of the LSC.

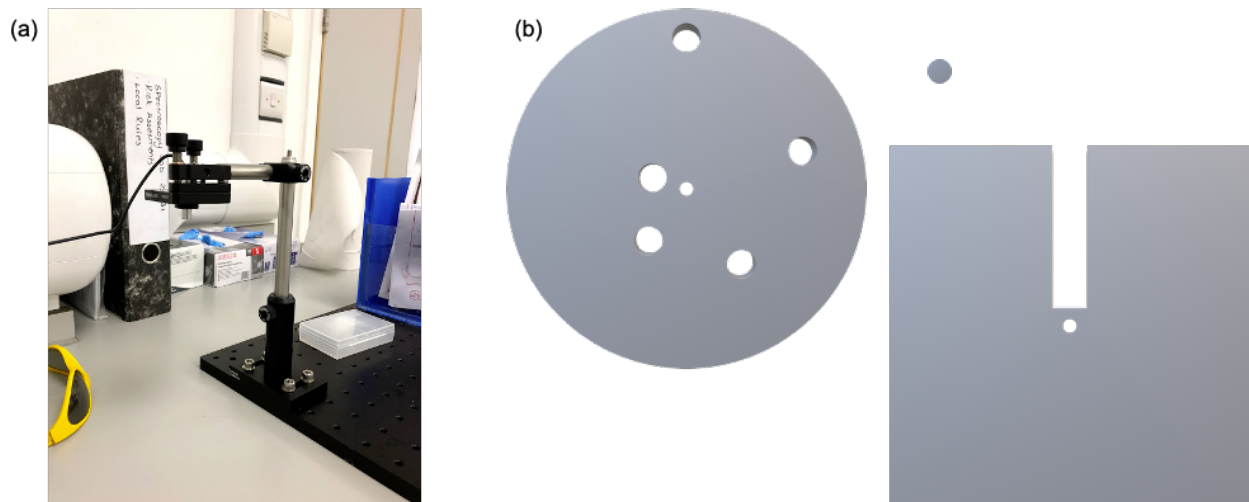


Figure 59: Scattering characterization setup for 3D printed LSCs. (a) Picture of near-IR laser to be positioned above the LSC. The clamps allow adjustment of the stands and movement in the x - and z - directions. (b) Shows a CAD model of the optical mask to be placed on top of the LSC to properly position the laser. The top has holes placed in specific distances from the center. The pin allows this top to rotate while remaining attached to the bottom. The bottom is rectangular to cover any other incident light on the LSC but has a slit to let any light passing through the hole in the top to reach the LSC.

The Thorlabs CPS780S (780 nm, 2.5 mW) collimated laser was used as the laser light source. The near-IR wavelength was chosen to prevent interactions with LR305. The laser forms an elliptical beam of size 3.8 mm \times 1.6 mm. A custom mount was designed based on parts from Thorlabs.

To accurately position the laser above the LSC sample and ensure consistent laser shape, a mask was created to place on top of the LSC, as seen in Figure 59(b). This mask had 3 parts: a rotating top with holes in specific positions, a pin, and a bottom with a slit to allow light passing through the hole in the top mask to reach the LSC.

9.2.3.8. Integrating sphere

An International Light Technologies integrating sphere was used to collect light emitted from the LSC. This was used either for edge emission measurement or light scattering measurement. The solar simulator was coupled to a SpectraLight ILT950 spectroradiometer using an optical cable for final spectral readouts, which could be analyzed within the software itself or exported for post-processing.

A custom sample holder was 3D printed to keep the LSC flat and block out any environmental light. A picture of the sample holder attached to the integrating sphere as well as a CAD model of the sample holder are shown in Section 4.5.2, Figure 27(a,b).

9.3. Additional Data

9.3.1. LSC edge emission

The full data for LSC edge emission measured using the integrating sphere and spectrometer setup is available in Figure 60.

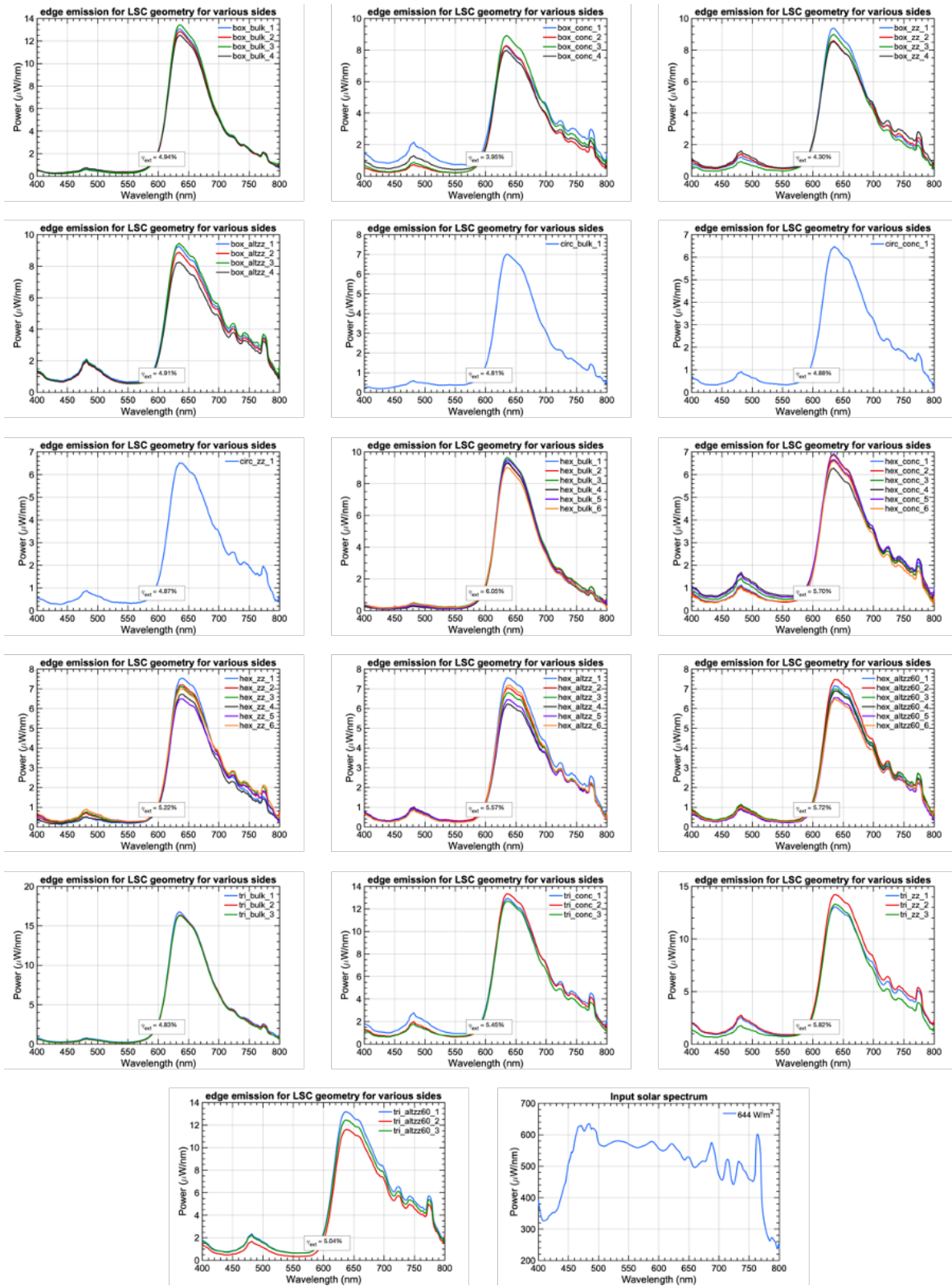


Figure 60: All edge emission data for bulk and 3D printed LSCs. The geometry of each LSC is listed in the top right corner of each plot. Edge emission from each side was measured and was averaged to calculate the overall efficiency of the part.

9.3.2. Optical Efficiency Data

Table 11: Experimentally measured efficiency for various LSC geometries fabricated either by conventional manufacturing techniques (bulk) or with 3D printing (concentric, zigzag, alternating zigzag). Efficiency measurements are presented for various wavelength ranges to vary the effects of scattering on efficiency.

LSC type	LSC shape	600-700 nm	400-800 nm	350-1000 nm
Bulk	Box	13.52%	4.94%	4.05%
	Circle	12.30%	4.81%	3.91%
	Hexagon	16.97%	6.05%	4.82%
	Triangle	13.57%	4.83%	3.81%
Concentric	Box	9.31%	3.95%	3.27%
	Circle	11.69%	4.88%	3.97%
	Hexagon	12.78%	5.70%	4.67%
	Triangle	12.47%	5.45%	4.54%
Zigzag	Box	10.26%	4.30%	3.48%
	Circle	11.56%	4.87%	3.96%
	Hexagon	12.99%	5.22%	4.20%
	Triangle	12.99%	5.82%	4.94%
Alternating Zigzag (90)	Box	10.53%	4.91%	4.16%
	Hexagon	13.04%	5.57%	4.60%
Alternating Zigzag (60)	Hexagon	13.18%	5.72%	4.79%
	Triangle	11.09%	5.04%	4.34%

9.3.3. Scattering Data

From the solar simulator data, it was possible to extract estimates for how much scattering contributes to edge emission of an LSC. This was done by integrating edge emission for all regions where LR305 does not emit (i.e. below 550 nm and above 700 nm) and dividing by the total edge emission. This was done for each edge emission spectrum and averaged over all sides to obtain a final mean value, reported in Table 12 and plotted in Figure 61.

Table 12: Scattering ratio, defined as fraction of scattered light (light of wavelengths below 550 nm and above 700 nm) over all emitted light, for various printing types and LSC shapes.

LSC type	LSC shape	Scattering Ratio
Bulk	Box	0.31
	Circle	0.34
	Hexagon	0.27
	Triangle	0.26
Concentric	Box	0.39
	Circle	0.37
	Hexagon	0.41
	Triangle	0.41
Zigzag	Box	0.37
	Circle	0.38
	Hexagon	0.35
	Triangle	0.43
Alternating Zigzag (90)	Box	0.45
	Hexagon	0.40
Alternating Zigzag (60)	Hexagon	0.42
	Triangle	0.45

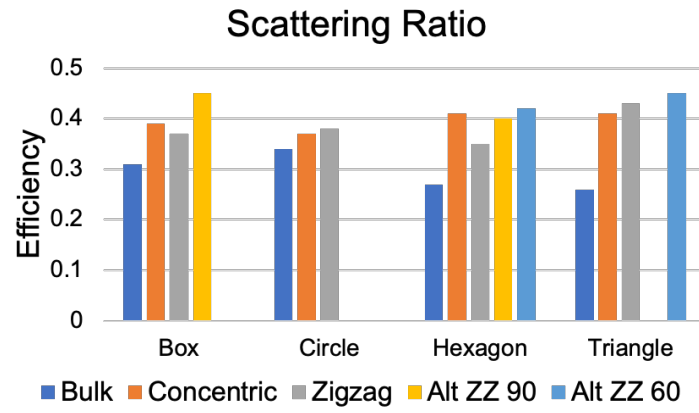


Figure 61: Scattering ratio for various LSC shapes and printing patterns. Graphed version of data in Table 12.